OBSERVING THE BARYON CYCLE IN HYDRODYNAMIC COSMOLOGICAL SIMULATIONS

BY

JACOB RICHARD VANDER VLIET, B.S., M.S.

A dissertation submitted to the Graduate School

in partial fulfillment of the requirements

for the degree

Doctor of Philosophy

Major Subject: Astronomy

New Mexico State University

Las Cruces New Mexico

May 2017

"Observing the Baryon Cycle in Hydrodynamic Cosmological Simulations " a dissertation prepared by Jacob R. Vander Vliet in partial fulfillment of the requirements for the degree, Doctor of Philosophy, has been approved and accepted by the following:

Louis Reyes
Dean of the Graduate School

Christopher W. Churchill
Chair of the Examining Committee

Date

Committee in charge:

Dr. Christopher W. Churchill, Chair

Dr. Anatoly Klypin

Dr. Rene Walterbos

Dr. Michael Engelhardt

DEDICATION

I dedicate this thesis to my wife, Ann Vander Vliet, for her unending patience and support.

ACKNOWLEDGMENTS

Thank you to the National Aeronautics and Space Administration (NASA) for funding this research through grants *HST*-AR 12646 and *HST*-GO-13398, as well as the NASA New Mexico Space Grant Consortium Graduate Research Fellowship.

Chris Churchill. Thank you for teaching me what it means to be an astronomer and for your support as I found a passion for coding. Your flexibility in redefining projects to support this passion will always be appreciated. Thank you for our long talks about the nature of graduate school and academia.

Glenn Kacprzak. Thank you for all your help in scaling up my work. Your advice for both career and research was always appreciated. Thank you for introducing me to the wonders of Australia, especially Australian Rules Football.

Anatoly Klypin. Thank you for helping me understand the realm of cosmological simulations. You always pushed me to find better ways of accomplishing a goal and to never settle for "what works".

Cameron Hummels. Thank you for our discussions on developing code structures. You opened up the world of astronomy beyond NMSU.

To the upper years. I am deeply appreciative to the upper year graduate students who taught me what graduate school is about and how to survive it when I first started. Jillian, Liz, Nikki, Cat, Nick, and Chas. The path would have been much more difficult without your help.

To my contemporaries. Our collaborations made the coursework survivable and fun. Thank you Nigel, Jean, Sean, and Diane.

Nikki. Thank you for your guidance in both the field of galaxy evolution and the field of graduate research. Your advice on dealing with the university, faculty, collaborators, and tea will never be forgotten. Thank you for letting me enter the 212 office, the greatest office in the Astronomy building.

Kenz. Thank you for your constant encouragement. I would have struggled to finish without your groundings.

Liz. Thank you for your help with research. This work would have taken years longer without your coding expertise.

Jodi. Thank you for keeping me social during my final year and preventing me from retreating into an upper-year shell.

Sean. Thank you for all the conversations throughout the years. Your friendship kept me sane over the years.

To my gaming group. Thank you Sean, Kenz, Diane, Kyle, Lauren, Jodi, Emma, Sam, Candace, Nigel, Gavin, and Kami for indulging my crazy plots and half-baked plans every week. The sessions kept me sane over the years.

To my family. Mom, Dad, Sherrie, Nicole, Jerad, and Joey, thank you for your support and encouragement throughout the long journey.

My greatest thanks to Ann, for her unending encouragement and support. Thank you for all the work you've done over the years to keep our lives going. Thank you for your understanding during the long nights of work. Thank you for forcing me to take vacations when I needed them. Thank you for everything. None of this would be possible without you.

VITA

EDUCATION

2011-2014 M.S., Astronomy
New Mexico State University
Las Cruces, New Mexico, USA

2004-2008 B.S., Physics
Colorado State University, *Cum Laude*
Fort Collins, Colorado, USA

AWARDS AND GRANTS

2016 NMSU Astronomy Zia Award

2015 NMSU Astronomy Pegasus Award

2012, 2013 New Mexico Space Grant Graduate Research Fellow

PROFESSIONAL ORGANIZATIONS

American Astronomical Society

PUBLICATIONS

Churchill, C.W., Vander Vliet, J.R., Trujillo-Gomez, S., Kacprzak, G.G., Klypin, A, 2015, The Astrophysical Journal, 802, 10, *Direct Insights Into Observational Absorption Line Analysis Methods of the Circumgalactic Medium Using Cosmological Simulations*

Churchill, C.W., Klimek, E., Medina, A., Vander Vliet, J.R., 2014, arXiv:1409,0916, *Ionization Modeling Astrophysical Gaseous Structures. I. The Optically Thin Regime*

PUBLISHED CONFERENCE ABSTRACTS

Vander Vliet, J.R., Churchill, C.W., Trujillo-Gomez, S., Klimek, E.S., Klypin, A.A., 2014, The 223rd Meeting of the American Astronomical Society, Abstract 458.12, *A Comparison of the Circumgalactic Medium of Present-Day Dwarf and Milky Way Galaxies using Absorption Line Analysis thorugh Hydrodynamic Cosmological Simulations*

Vander Vliet, J.R., Churchill, C.W., Klimek, E.S., Trujillo-Gomez, Ceverino, D., S.Klypin, A.A., 2013, The 221st Meeting of the American Astronomical Society, Abstract 227.07, *The Distribution of Metals in the High Redshift Circumcalctic Medium Around Milky Way Progenitors*

FIELD OF STUDY

Major Field: Astronomy – Galaxy Evolution

ABSTRACT

OBSERVING THE BARYON CYCLE IN HYDRODYNAMIC COSMOLOGICAL SIMULATIONS

BY

JACOB RICHARD VANDER VLIET, B.S., M.S.

Doctor of Philosophy
New Mexico State University
Las Cruces, New Mexico, 2017
Dr. Christopher W. Churchill, Chair

An understanding of galaxy evolution requires an understanding of the flow of baryons in and out of a galaxy. The accretion of baryons is required for galaxies to form stars, while stars eject baryons out of the galaxy through stellar feedback mechanisms such as supernovae, stellar winds, and radiation pressure. The interplay between outflowing and infalling material form the circumgalactic medium (CGM). Hydrodynamic simulations provide understanding of the connection between stellar feedback and the distribution and kinematics of baryons in the CGM. To compare simulations and observations properly the simulated CGM must be observed in the same manner as the real CGM. I have developed the Mockspec code to generate synthetic quasar absorption line observations of the CGM in

cosmological hydrodynamic simulations. Mockspec generates synthetic spectra based on the phase, metallicity, and kinematics of CGM gas and mimics instrumental effects. Mockspec includes automated analysis of the spectra and identifies the gas responsible for the absorption. Mockspec was applied to simulations of dwarf galaxies at low redshift to examine the observable effect different feedback models have on the CGM. While the different feedback models had strong effects on the galaxy, they all produced a similar CGM that failed match observations. Mockspec was applied to the VELA simulation suite of high redshift, high mass galaxies to examine the variance of the CGM across different galaxies in different environments. The observed CGM showed little variation between the different galaxies and almost no evolution from z=4 to z=1. The VELAs were not able to generate a CGM to match the observations. The properties of cells responsible for the absorption were compared to the derived properties from Voigt Profile decomposition. VP modeling was found to accurately describe the HI and MgII absorbing gas but failed for high ionization species such as CIV and OVI, which do not arise in the coherent structures assumed by modelling. The technique of mock QAL is useful for testing the accuracy of the simulated CGM and for verifying observational techniques, but not for differentiating between feedback prescriptions in dwarf galaxies.

Contents

LIST OF TABLES

LIST OF FIGURES

LIST OF ABBREVIATIONS

AGB	Asymptotic Giant Branch
AGN	Active Galactic Nucleus
AMR	Adaptive Mesh Refinement
ART	Adaptive Refinement Tree
AOD	Apparent Optical Depth
CDM	Cold Dark Matter
COG	Curve of Growth
COS	Cosmic Origins Spectrograph
COSFUV	Cosmic Origins Spectrograph Far-Ultraviolet
CGM	Circumgalactic Medium
DM	Dark Matter
EW	Equivlient Width
GMC	Giant Molecular Cloud
HIRES	HIgh Resolution Echelle Spectrometer
ISM	Interstellar Medium
IR	Infrared
IRAS	Infrared Astronomical Satellite
ISF	Instrumental Spread Function
ISM	Interstellar Medium
LLS	Lyman Limit System
LOS	Line of Sight
QAL	Quasar Absorption Line
SFR	Star Formation Rate
SN	Supernova
SNR	Signal to Noise Ratio
SPH	Smoothed Particle Hydrodynamics
sSFR	Specific Star Formation Rate
UV	Ultraviolet
UVB	Ultraviolet Background
UVES	Ultraviolet and Visual Eschelle Spectrograph
VP	Voigt Profile
WMAP	Wilkinson Microwave Anisotropy Probe

1. INTRODUCTION

1.1. Galaxy Evolution

Galaxies are the among the largest and most prominent structures in the universe. Collections of dust, gas, stars, black holes, and dark matter (DM), galaxies act as stellar factories to turn the hydrogen and helium gas created by the Big Bang into heavier elements. The study of how galaxies form and evolve has been a major field in astronomy since galaxies were first identified to be separate bodies outside of the Milky Way. Early models by Eggen et al. (1962) described a monolithic collapse scenario where galaxies collapse out of a gas and dust cloud in the intergalactic medium (IGM). The field has advanced a great deal since then, such as when Searle & Zinn (1978) described galaxy growth through mergers.

The modern understanding of galaxy formation follows from models describing the three main contributors to the energy balance of the universe. The dominant source of energy density is dark energy, a negative pressure described by the cosmological constant Λ, which accounts for 69.2% of the total energy density of the universe (Planck Collaboration et al. 2016). The second largest contribution to the total energy density is dark matter (DM), which is predicted to be cold and to contribute 26.8% of the total energy density. The dark matter is predicted to have speeds small compared to the speed of light and thus is referred to as cold dark matter (CDM). The rest of the total energy density of the universe comes from baryonic matter such as gas, dust, stars, and planets. Together the model is referred to ΛCDM (see Frenk & White (2012) for a review). The large scale structure of the universe is formed by the competing effects of gravitational collapse of the dark matter (DM) and the acceleration of spatial expansion by dark

energy (Λ) on random density fluctuations created by the Big Bang. As the universe expands DM collapses into filamentary structures, creating the cosmic web. Gravity pulls DM along the filaments to form dense halos at their intersections which form the basis of galaxies. Surveys of galaxies such as the Sloan Digital Sky Survey (Abazajian et al. 2003) have been able to detect the cosmic web by the 3D location of galaxies (Sarkar et al. 2012).

The primary method to understand galaxy evolution from a theoretical standpoint is using computational simulations. Simulations attempting to create the large scale structure of the universe only include dark energy and dark matter. While these simulations are very successful in reproducing observations of the universe on the largest scales (Heitmann et al. 2005; Springel 2005; Springel et al. 2006; Klypin et al. 2011), baryons must be included to fully bring simulations into agreement with observations.

Including baryons makes the simulations significantly more difficult. Dark matter interacts only through gravity through general relativity which is relatively easy to include in simulations. Baryons, however, also interact through the electromagnetic force in addition to gravity. To properly account for baryonic physics, simulations need to accurately describe radiative cooling, hydrodynamic instabilities, and shocks, which requires high spatial and mass resolution.

The effect of baryons on the universe is limited to the interior of DM halos where they can become dense enough to dominate over DM. Through interacting with the electromagnetic force, which DM cannot do, baryons can radiatively cool, allowing them to collapse into denser structures than DM can. The baryons cool and form the basis of a galaxy by collapsing into structures that are able to form

stars.

Star form when the gas within a galaxy, called the interstellar medium (ISM), gravitationally collapses into structures hot enough to fuse hydrogen and helium into heavier elements (metals). Eventually a star burns through its supply of fusible gas causing it to die in either a supernovae (SNe) for high-mass stars or a red giant to white dwarf for low-mass stars, both of which return their metal-enriched gas to the interstellar medium (ISM) of the galaxy. The returned gas can then form new stars. As long as the galaxy has adequate gas supply it will continue to form new stars and grow. Since stars do not return all of their mass back to the ISM, over time the galaxy will deplete its gas supply. Timescales for gas depletion are much shorter than the Hubble timescale ($\sim$ 14 Gyr) and are often on the order of 3 Gyr (Kennicutt et al. 1994; Rahman et al. 2012; Pflamm-Altenburg & Kroupa 2009). However many galaxies are observed to have sustained star formation for time periods longer than the depletion timescales, necessitating the acquisition of new material. Without accreting new gas a galaxy would deplete its reserve and cease star formation. A galaxy's star formation rate is a key difference between the two main classes of galaxies, blue galaxies which have active star formation and red galaxies that are quiescent with little star formation (Strateva et al. 2001; Baldry et al. 2004, 2006; Faber et al. 2007; Martin et al. 2007; Schawinski et al. 2014).

Galaxies acquire their gas through several methods. Mergers between galaxies combine their gas supply, fueling bursts in star formation. Gas can also be accreted from the intergalactic medium (IGM), the gas between galaxies.

The accretion of IGM along DM filaments occurs in either "cold-mode" or

"hot-mode" accretion. Described in Birnboim & Dekel (2003) and Dekel & Birnboim (2006), their model states that small to medium galaxies ($M_{vir} < 10^{12}$ $M_{\odot}$) are fed by cold streams of gas pulled from the IGM along DM filaments. In the early stages of galaxy evolution the cold streams efficiently deliver gas to the galaxy itself which readily for stars.

As the galaxy grows it builds up a gaseous halo. Eventually the halo becomes large enough it can support shocks and the inflowing streams become shock-heated to the virial temperature (T_{vir}) and cannot efficiently cool ($T > 10^6$ K, $M_{vir} > 10^{12}$ $M_{\odot}$). The hot gas must cool before it can condense onto the galaxy. The long cooling timescales of the hot gas leads to the creation of a hot gaseous halo that cannot reach the galaxy. Without gas accreting onto the galaxy the gas reserves are rapidly depleted, stagnating star formation through a process called "strangulation" (Kereš et al. 2005; Rasmussen et al. 2008; van de Voort et al. 2017). The shutdown of available cold gas for a galaxy to accrete is the most common way for galaxies to transition from blue, star forming galaxies to red, quiescent galaxies (Peng et al. 2015).

The mass delimitation between hot- and cold-mode accretion occurs in the recent universe ($z < 2$). At high redshift ($z > 2$) the filaments are still dense enough that they can potentially penetrate the hot halo of a massive galaxy without being shock heating. The lack of shock heating in the core of the filament allows for efficient accretion of gas to massive galaxies and is the source of massive star-forming galaxies seen in the high redshift universe. A summary of these accretion modes are shown in Figure 1.1. The predictions of the two accretion mode have been supported in hydrodynamic cosmological simulations (van de Voort & Schaye 2012, e.g.).

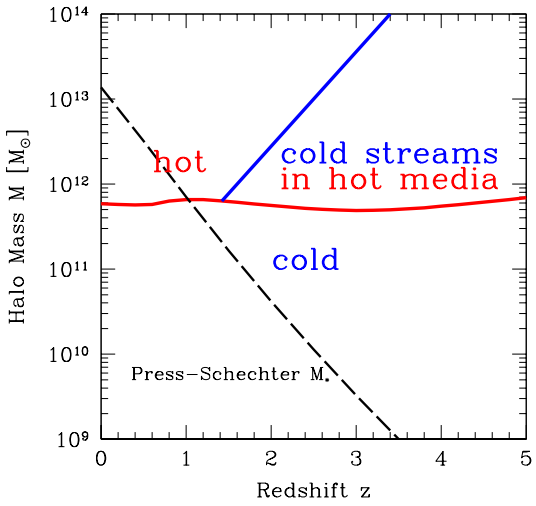

Fig. 1.1.— The conditions for hot-mode and cold-mode accretion. Adapted from Dekel et al. (2009).

1.2. The Baryon Cycle

Of primary interest in simulations is the creation of galaxies that match common observations, such as the stellar mass-halo mass relation, the Tully-Fisher Relation, the Main Sequence Relation, and the Kennicutt-Schmidt Law. To meet these goals simulations must create stars properly.

Stars have a greater impact on galaxy evolution than merely consuming gas. The formation of stars is not an efficient process (McKee & Ostriker 2007), with typically only 2–20% of the mass in giant molecular clouds (GMC) being converted into stars (Zuckerman & Evans 1974; Evans et al. 2009; Murray et al. 2011).

The process of converting gas to stars is disrupted by the recently formed stars themselves. Through stellar feedback processes such as supernovae (SNe), stellar winds, and radiation pressure, the stars push back on the gas and dissipate the GMC. Star formation becomes a self-regulated process in which only a small fraction of the gas can turn into stars before being pushed dissipated (e.g. Hopkins et al. 2011; Ceverino et al. 2014). The effect of SNe, radiation pressure, and stellar winds disrupt the surroundings enough to prohibit gravitational collapse. These processes import significant amount of energy to the gas enabling some of it to escape the galaxy itself in the form of outflows and enter the circumgalactic medium (CGM) (Oppenheimer et al. 2010; Davé et al. 2011). Once in the CGM the ejected material has three possible fates (Ford et al. 2013):

- If the gas is cool enough or contains enough metals, it can cool quickly and fall back into the galaxy with timescales of <1 Gyr in a process known as galactic fountains (Bregman 1980; Sharma et al. 2014; Marasco et al. 2015).
- If the gas is not able to cool, it is unable to fall into the galaxy and instead becomes part of the ambient CGM.
- If the outflows are moving fast enough they can escape the potential well of the galaxy entirely and enter the IGM.

The flow of gas from accretion to star formation to outflows to re-accretion is known as the "baryon cycle" and is one of the most influential processes that govern galaxy evolution. Galaxy-scale outflows are required to explain several observations, such as the mass-metallicity relation (e.g. Erb et al. 2006) and IGM metal content (e.g. Aguirre et al. 2001; Pettini et al. 2003; Oppenheimer & Davé

2006).

Hydrodynamic simulations of galaxy evolution have supported the abilities of outflows to govern galaxy and IGM evolution. The addition of momentum-driven winds in SPH simulations in Oppenheimer & Davé (2006) match IGM-based C IV absorption features at $z \sim 2$–5. Using the same recipes, Oppenheimer et al. (2010) found galactic winds are the dominant factor in shaping the galaxy stellar mass function at $z = 0$.

Bertone et al. (2007) predicted the existence of recycled accretion from semi-analytic models of galaxy evolution, later confirmed in the hydrodynamic simulations of Oppenheimer & Davé (2008) The dominant fate of wind material is reaccretion, with most wind material being ejected upwards of four times between $z = 6$ and $z = 0$. For $z < 1$, L^* galaxies are mostly unable to eject wind particles from their halo, creating extensive galactic fountains where gas is continuous ejected from the galaxy by stars then reaccreted later, with typical timescales of reaccretion of ~ 1 Gyr.

By controlling the supply of gas to a galaxy, the baryon cycle is one of the major drivers of galaxy evolution. The CGM is a massive repository of gas formed from the mixture of outflows from the galaxy and inflows from the IGM. To understand the wide variety of galaxies that exist, from the An active baryon cycle is required for an active galaxy to exist. It can contain as much mass as the ISM of the galaxy (e.g. Tumlinson et al. 2011; Thom et al. 2012; Stinson et al. 2012; Werk et al. 2014) and is a possible solution to the missing baryons problem (Persic & Salucci 1992; Bell et al. 2003; McGaugh 2008; McGaugh et al. 2010), with determined 25% of cosmic baryons exit in the CGM of galaxies (Davé et al.

2010).

1.3. Observing the Baryon Cycle in the CGM

Studying the baryon cycle in the CGM is difficult. Typical densities of gas in CGM are low ($n_H < 10^{-2}$ cm^{-3}) making any emission weak and difficult to observe. The hydrogen CGM has been directly imaged around very large, active galaxies, but these are rare cases (Martin et al. 2014, e.g.).

Without emission observations the primary method for observing the CGM utilizes absorption spectra of background objects. Light from a bright background source such as a quasar passes through the CGM and is partially absorbed by the gas, leaving atomic fingerprints of the CGM's constituents in the spectrum. A benefit of this method is the gas can be observed from any distance as long as a significantly bright background object exists, enabling the study of high-z CGM and the evolution of the CGM.

Quasar absorption line (QAL) studies are a powerful method for exploring the circumgalactic medium. Careful modeling of absorption features can determine the temperature, column density, composition, ionization state, and kinematics of the medium. There are limitations to the QAL method, however. The derived kinematics are restricted to motion along the line of sight. The strength of absorption depends on the column density of material and not the number density, meaning it is impossible to determine the exact spatial structure of the material without assumptions. The feature modeling itself depends on assumptions of the spatial structure and equilibrium status of the medium.

Due to the pencil-beam nature of the absorption, the observation only yields

information about the CGM in one very small section of the halo, restricted to a single impact parameter D (the projected distance between the LOS and the host galaxy). To build up information about the spatial structure of the CGM multiple galaxies must be observed. On rare occasions a galaxy might have multiple background QSO which allow for measuring the same galaxy multiple times (Chen et al. 2014).

Another concern is the difficulties in detecting where the absorption is relative to the hot galaxy. The line-of-sight velocity v_{LOS} of the absorbing material can be determined from modeling of the feature. However, a redshifted feature relative to the galaxy might be infalling material on the near side of the galaxy or outflowing material on the far side.

The discussion so far has assumed that the host galaxy has been identified which is not always the case. To identify the galaxy responsible for an absorption feature in a QSO spectrum requires follow-up observations to determine the redshift of all galaxies along the LOS. Since CGM features have been detected with $D > 1$ Mpc (e.g. Rudie et al. 2012), all galaxies within this large impact parameter range must be identified with redshifts accurate enough to identify the galaxy responsible for the absorption feature. The identification process by itself is difficult and often impossible. Observations without identified associated galaxies are still useful in providing statistical restrictions on models (van de Voort & Schaye 2012; Prochaska et al. 2010; Bird et al. 2013). An example is the bimodality of the metallicity of $z < 1$ Lyman-limit systems (LLS, $N_{\rm H\,I} > 10^{17.2}$ cm^{-2}) as observed by Lehner et al. (2013). The interpretation of the low-metallicity LLS arising from pristine accretion and the high-metallicity LLS arising from recycled accretion gives an observational method for identifying the physical nature

of absorbing gas.

The central challenge in QAL observations is the difficulty in converting the derived properties (column density, v_{LOS}, etc.) to actual physical properties due to projection effects and observational constraints. Simulations of the baryon cycle can be used. Hydrodynamic simulations can be used to better understand the connection between the structure and kinematics of gas in the CGM and the resulting QAL observation.

When analyzing the simulated CGM there are two methods commonly used. The first is to pull the gas properties, such as temperature, density, and metallicity, directly from the simulation output. Studying the simulation outputs in this manner enables a direct measure of the structure and evolution of the CGM.

A common part of the direct measure method is to post-process the simulation to determine the distribution of an ion of interest based on the location, density, temperature, and metallicity of the gas, then creating a 2D projection map to determine the column density profile of the ion. (e.g. van de Voort & Schaye 2012; Shen et al. 2012, 2013; Hummels et al. 2013; Rahmati et al. 2016; Gutcke et al. 2017). The comparison of the column density profile from a projection to one determined from observation should be done with caution though as observations determine the column density by modeling the absorption, which involved several assumptions that may not hold in all situations. The direct analysis approach has been used extensively in the past.

The limitation of the projection is its inability to verify the accuracy of the simulation CGM through comparison with observations. Observations do not measure the temperature, density, and metallicity of the gas in a galaxy's CGM.

The gas properties are the results of modeling absorption profiles.

The second approach is to construct mock observations of the simulated CGM. By mimicking the method by which observers use to study the CGM around real galaxies the veracity of the simulated CGM can be determined. Additionally the process can be turned around and the accuracy of observational modeling can be determined by comparing the modeled physical gas properties to the actual gas properties taken from the simulation.

The mock observation method has been implemented by fewer studies due to its additional complexities. Ford et al. (2013) used synthetic observations of the simulations of Oppenheimer & Davé (2008) to determine the effect of different wind models have on the CGM as traced by various commonly observed transitions. In Ford et al. (2014) they determined which ions should be observed to study various parts of the baryon cycle. For example, Mg II absorption traces recycled accretion of recently ejected winds while O VI absorption traces old outflows that are now a part of the stagnant CGM.

1.4. Purpose of this dissertation

The primary method of observing the CGM, QAL studies, is fraught with assumptions and simplifications. The theoretical approach to galaxy evolution, using cosmological simulations, is likewise restricted by simplifications. By combining these two approaches, the strengths of one can be used to overcome the weaknesses of the other. This leads to a better understanding of the limits of each toolset and to a better interpretation of evidence for galaxy evolution.

The structure of this dissertation is as follows. The first half of Chapter 2

describes details of hydrodynamic simulations that pertain to studying the baryon cycle. The primary product of this dissertation is the `MOCKSPEC` code which studies the simulated CGM by generating mock QAL observations. The second half of Chapter 2 describes how `MOCKSPEC` works. Chapter 3 describes the application of `MOCKSPEC` to hydrodynamic simulations of dwarf galaxies to examine how different models of stellar feedback alter the observable properties of the CGM. The connection between the properties of the CGM as derived from observational techniques and the true properties is also discuss in Chapter 3. Chapter 4 describes the application of `MOCKSPEC` to high redshift simulations of massive galaxies to examine how the observable CGM evolves across time and environment. Chapter 5 describes how cosmological inflows evolve in response to major mergers and starbursts. Chapter 6 contains a summary of the conclusions from this dissertation.

2. THE MOCKSPEC CODE

2.1. Overview

The circumgalactic medium (CGM) is a critical driver of galaxy evolution through its participation in the baryon cycle. Understanding how the reservoir of gas in a galaxy's halo interacts with the galaxy through accretion and galaxy outflows is challenging to do in observations. The CGM is diffuse and only reliably observable through absorption features in the spectra of background objects. Interpreting absorption spectra is difficult and full of assumptions about the physical and kinematic structures of the material creating the absorption.

Hydrodynamic cosmological simulations can be used to compliment observations of the CGM. The physical and kinematic structures of the gas can be directly taken from the simulation output. However comparing the simulated gas properties to the observed absorption profiles directly is difficult. A commonly used technique (Hummels et al. 2013; Smith et al. 2011; Liang et al. 2016) is to generate column density maps from projections of the gas distribution in the simulations after it has been post-processed with `CLOUDY` (Ferland et al. 2013) to combine gas density, temperature, metallicity, and ionization conditions to obtain densities of ions of interest such as Mg II or O VI. From the column density maps an equivalent width map can be determined using the curve-of-growth (COG) analysis outlined in Draine (2011). The COG method is simple to implement but is also very limited as it assumes all gas along the LOS contributes to the final equivalent width while ignoring any velocity structure in the gas or instrumental effects such as ISF and noise.

The proper method for comparing the simulated CGM with the observed

CGM is to create mock observations of the simulations and analyze the resulting spectra with the same tools used by observers to analyze real observations.

There are a few tools to generate the mock observations. To analyze SPH simulations there have been `SPECWIZARD` (Theuns et al. 1998) for `GADGET` simulations and `SPECEXBIN` (Oppenheimer & Davé 2006) used by Ford et al. (2013, 2014, 2016) to analyze the outputs of `GADGET-2` simulations. There have been no synthetic spectra generation codes for AMR simulations. The general simulation analysis toolset `yt` (Turk et al. 2011), has a recent addition named `TRIDENT` (Hummels et al. 2016) which creates mock quasar absorption spectra for the most commonly used cosmological simulation codes.

A shortcoming of all previous codes is their lack of consistent analysis. The codes generate spectra but it is left to the user to apply their favorite analysis tools to determine column density and equivalent distributions.

In this chapter the code `MOCKSPEC` is presented. `MOCKSPEC` is a pipeline to analysis the CGM of galaxies simulated with `ART` through the generation and analysis of mock quasar absorption spectra with the full treatment of instrumental effects.

2.2. Simulations

To generate a galaxy in simulations that resembles observed galaxies, the code must address the two dominant constituents of the galaxy: the dark matter (DM) and the baryons (gas and stars). The DM particles only interact through gravity (for a review on gravity solvers, see Dehnen & Read (2011)). The baryons are subject to the Euler equations of hydrodynamics. The details of how simulations

handle hydrodynamics is key to studies of the baryon cycle as many approaches exist and each have unique strengths and weaknesses.

Hydrodynamic simulation codes are broadly separated into two groups: (1) Adaptive Mesh Refinement (AMR) (e.g. Berger & Colella 1989), and (ii) Smooth-Particle Hydrodynamics (SPH) (e.g. Gingold & Monaghan 1977; Owen et al. 1998). In recent years, there have been attempts to create codes that feature traits of both code families with moving-mesh codes such as `AREPO` (Springel 2010). A brief discussion on the differences between AMR and SPH codes is included here (see Agertz et al. 2007, for a detailed analysis).

The primary different between AMR and SPH codes is how they handle the hydrodynamic equations. AMR codes utilize a Eulerian approach, where the coordinate system remains fixed. The volume is divided into cells, quantizing space, and the advection of gas properties across the cells are computed. The solutions to the hydrodynamic equations are more accurate (e.g., able to resolve shocks) with smaller grid sizes but this leads to an increase in computational load. A compromise between the competing effects of accuracy and computational load is to adaptively refine the size of cells based on conditions of the gas, typically the density. The result is high spatial resolution in areas of high density where the increased accuracy is needed and low spatial resolution in areas of low density to reduce the computational load. However, since gas is treated as a field it is impossible to track the trajectory of a gas structure such as winds in an AMR simulation.

The SPH method utilizes a Lagrangian approach to the equations of hydrodynamics where the coordinate system moves with the gas. Gas is divided into

particles, quantizing mass, and the gas properties of each particle are tracked. A strength of the SPH method is the ability to track the trajectory of a gas particle which AMR simulations cannot do. Shortcomings of the SPH method include difficulties in resolving shocks and instabilities such as the Kelvin-Helmholtz instability and handling gas mixing effectively.

2.2.1. Adaptive Refinement Tree

The `MOCKSPEC` code works with the code *hydroART*, an AMR code using the Adaptive Refinement Tree method to refine space along with an Eulerian approach to solve the hydrodynamics. The refinement tree is able to achieve high resolution (sub-kpc) in regions of high density to properly resolve the relevant physics while maintaining low spatial resolution in other areas.

The *hydroART* code was written by Andrey Kravtsov (Kravtsov et al. 1997; Kravtsov 1999). It has been improved by Daniel Ceverino (Ceverino & Klypin 2009; Ceverino et al. 2010), Sebastian Trujillo-Gomez (Trujillo-Gomez et al. 2015) and Kenza Arraki (Arraki 2016).

The galaxies simulated with *hydroART* are cosmological zoom-in simulations. The zoom-in method enables the study of galaxy evolution in a cosmological setting. Initially, a large volume, typically on the order of 10 Mpc h^{-1} along a side, is simulated with DM only. DM only interacts through gravity, so the equations of hydrodynamics are not relevant, greatly simplifying the computations. When the simulation has reached the target age, usually $z = 0$, the resulting DM systems are examined. The box is searched for halos that are of the mass desired with the correct history (e.g. quiet vs active merging). When the desired halo is found,

the DM particles that make up the halo are traced back to the beginning of the simulation. The initial conditions of the relevant particles are used as the initial conditions for a second simulation. The second run includes baryons and the required hydrodynamics. To make the run more efficient, only the area around the identified DM particles are simulated in high resolution. The end result is a large cosmological box simulated in very poor resolution with only the area around the galaxy of interest simulated in high resolution.

One of the chief advantages of *hydroART* over other simulation codes is its ability to reach high spatial resolution, achieved through the Adaptive Refinement Tree method which describes how the code divides up space to solve the Eulerian equations for hydrodynamics. In its initial state the code quantizes space into a uniform grid. When the refinement criteria in a cell is reached, the cell is divided into eight equal sized subcells. This process continues until a maximum depth is reached, typically around 11–13.

Galaxies are composed of more than dark matter and gas, however. Prescriptions for star formation and feedback are needed. The current star formation prescription was implemented in Trujillo-Gomez et al. (2015) and changed star formation from a stochastic sampling to a deterministic process. Star formation methods are activated anytime the gas in a cell would reach a certain density threshold. In previous versions of *hydroART* there would be a random chance that the gas would be consumed to form a star. On a "success" all the gas in the cell would be turned into a stellar particle. Observations have determined that star formation is an inefficient process, with only $\sim$2% of gas in a giant molecular cloud being converted to stars (Krumholz & Tan 2007). To match the observations the probability of a dense gas cell being converted into a stellar particle was low.

The result is that on average the fraction of gas able to form stars that actually do matches the observations, but each individual dense cell either does form stars or does not. The result is few, massive stellar particles.

In the new version of *hydroART* every cell that reaches the critical density to form stars does, a description that matches the actual events in a galaxy. Instead of having all the mass in the cell being converted into a stellar particle, only a fraction of the cell's mass is converted. The results is more, smaller stellar particles in the simulation.

Once a stellar particle has formed it begins to influence its surroundings. Since *hydroART* is unable to simulated individual stars the details of stellar feedback are included in sub-grid models. The details of sub-grid models is one of the largest open questions in simulations of galaxy evolution.

The sub-grid model used in *hydroART* contains descriptions of stellar winds, supernovae, and radiation pressure (Ceverino & Klypin 2009; Ceverino et al. 2014; Trujillo-Gomez et al. 2015, see). Stellar winds are treated as a thermal energy source. SNe feedback is separated into SNIa and SNII feedback due to the different timescales they affect. SNII act on a shorter timescale than SNIa. Radiation pressure from massive stars is the newest addition to *hydroART* to reflect findings that it is a primary cause of molecular cloud disruption, acting before SNe occur Murray et al. (2011); Hopkins et al. (2011).

2.2.2. Simulations of Dwarf Galaxies

The dwarfs used in the study described in Chapter 2.7 were generated with the N-body plus hydrodynamics AMR code *hydroART* (Kravtsov et al. 1997;

Kravtsov 1999). They are the result of a cosmological "zoom-in" simulation detailed in Trujillo-Gomez et al. (2015).

The thermal balance of the gas is determined using heating and cooling functions obtained form the radiative transfer code Cloudy (Ferland et al. 1998, 2013). The heating and cooling functions include metal and molecular line cooling, and a uniform ionizing background Haardt & Madau (2001) with self-shielding of high column density gas. The star formation model implemented in *hydroART* is based on observations of star forming regions in molecular clouds. Stars are formed deterministically with the observed low efficiency in cold, dense gas of $\sim$ 2–3%. The stellar feedback model includes the major contributions from photoionization heating, direct radiation pressure, energy from type Ia and type II supernovae, and stellar winds. The star formation and feedback model was shown to reproduce many properties of low-mass galaxies at $z \sim 0$ without fine tuning, such as the stellar to halo mass ratio, cold gas fraction, baryon content, star formation history, rotation curves, and morphologies.

The CGM of the simulations of low-mass galaxies designated dwSN, dwALL_1, and dwALL_8 presented in Trujillo-Gomez et al. (2015) were analyzed. The host dark matter halo hosts an isolated dwarf galaxy with $M_{vir} = 2.8 \times 10^{10}$ $M_{\odot}$, $R_{vir} = 80$ kpc. The simulations reached a minimum cell size of 40 h^{-1} pc and a DM mass resolution of 9.4×10^4 $M_{\odot}$. The simulation was run multiple times with different feedback recipes to explore the effect feedback has on the galaxy and its surroundings. The feedback prescription for each run are summarized in Table 2.1. SNII+SN indicates supernovae and stellar winds, RP stands for radiation pressure, and PH stands for photoheating. Run dwSN includes only supernovae and stellar wind feedback while dwALL_1 and dwALL_8 include radiation pressure

and photoheating. The radiation pressure is modeled as an additional momentum source whose strength depends on the optical depth of the gas τ_{tot}. The photoheating is modeled as an additional pressure. The subscript in the run name denotes the strength of the photoheating pressure in units of $10^6\, k_B$ K cm^{-3}.

The stellar properties of the simulations depends heavily on the feedback prescription. Radiation feedback stops star formation earlier than supernovae, resulting in fewer stars being formed. Consequently the runs with stronger radiation feedback result in a galaxy with a lower stellar mass. The properties of the runs are shown in Table 2.2. Despite the similar virial mass, the stellar mass varied by two orders of magnitude in dwSN and dwALL_8, revealing the magnitude of the effect additional stellar feedback physics had on the evolution of galaxies.

2.2.3. Simulations of Massive Galaxies

Investigating the evolution of Milky Way-massed galaxies is of central interest to the field of galaxy evolution. Galaxies in this mass range rest at the peak of star formation efficiencies (Behroozi et al. 2013a) and are thus expected to be actively producing stars. The active star formation suggests an active baryon cycle, providing a valuable test bed for studying star formation, stellar feedback, and the role of the baryon cycle.

Table 2.1. Parameters for feedback in the simulations.

Mode	Feedback	τ_{tot}	P_{PH}/k_B (10^6 K cm^{-3})
dwSN	SNII+SW	-	0
dwALL_1	SNII+SW+RP+PH	1	1
dwALL_8	SNII+SW+RP+PH	1	8

The CGM of massive galaxies were analyzed using the VELA simulation suite as described in Ceverino et al. (2014); Zolotov et al. (2015). The VELA simulation suite was run to compliment the HST CANDELS survey (Barro et al. 2013, 2014). An overview of the suite is included here.

Each VELA galaxy was simulated in a box 20 h^{-1} Mpc along a side using the 5 year WMAP results (Komatsu et al. 2009) utilizing the zoom-in technique outlined in §2.2.1. The halos selected for the hydrodynamic run were selected based on their mass and merging history at $z = 1$. To be selected galaxies need to have $M_{vir} \sim 10^{11} - 2 \times 10^{12}$ $M_\odot$and to not be experiencing a major merger. The final simulations achieved a maximum spatial resolution of 17 pc, a DM particle mass of 8×10^4 $M_\odot$, and a minimum star particle mass of 10^3 $M_\odot$.

The hydrodynamic code used included prescriptions for gas cooling and heating, star formation, and stellar feedback in the form of stellar winds, SNe, radiation pressure and photoheating. Details on the gas cooling, heating and star formation can be found in Ceverino & Klypin (2009); Ceverino et al. (2014). The stellar feedback details are of interest to the baryon cycle and are briefly described here.

Stellar winds and SNe feedback were implemented as thermal energy sources. Stellar winds and SNII were combined into a single parameter that deposits thermal energy into the surrounding medium at a constant rate for the first 40 Myr

Table 2.2. Final mass of each dwarf galaxy

Model	M_{vir}	M_*
dwSN	3.0×10^{10}	8.1×10^8
dwALL_1	3.2×10^{10}	1.3×10^8
dwALL_8	2.8×10^{10}	2.1×10^7

after a stellar particle forms. The energy from SNIa are included after the time period ends.

Radiation pressure was added as a momentum driven wind. A non-thermal pressure was added to gas cells around a massive stellar particle younger than 5 Myr. For exact details on the implementation, refer to Ceverino et al. (2014); Agertz et al. (2013).

Photoheating was included as a separate pressure. In regions where the gas density is high enough ($\rho > 300$ cm^{-3}) the IR radiation from stars can become trapped and increase the pressure in the gas by a factor proportional to the IR optical depth in the gas, τ_{IR}.

The full `VELA` suite contained initial conditions for 35 galaxies, however only nine were used in this work, specifically halos #21–29. To accurately study the baryon cycle in the CGM of a galaxy the simulation must be run long enough to be able to build a healthy CGM. At very high redshift the galaxy has not experienced enough generations of stars to have a complete baryon cycle. The halos selected for the study were halos that had been run to the lowest redshift, reaching z=1, allowing for a study of the long-term evolution of the CGM.

Each halo in the `VELA` suite was simulated with three different feedback models. The first feedback model, formally named v1, contained models for stellar winds and SNe. The second model, formally named v2, included all the physics of the first model included as well as radiation pressure. The third model, formally named v2.1, included all the same physics as v2 but also included photoionization, photoheating, and radiation pressure IR trapping. The v2 and v2.1 simulation runs were renamed to `VELA2`a and `VELA2`b respectively for clarity in this work.

An analysis of the v1 simulations in Ceverino et al. (2014) found the simple feedback models were unable to create realistic galaxies as the simulations require radiation feedback to reduce the SFR to observed values. An analysis of the 2a and 2b simulations by Arraki (2016) found slight differences between the simulations. To reduce redundancies, the work presented in this chapter only used the 2b simulations.

The evolution of the properties of the galaxies are shown in Figure 2.1 with the final properties tabulated in Table 2.3. The galaxies all grow steadily throughout their evolution both in M_{vir} and M_*. A few of the galaxies experience major mergers which can be seen in the rapid increases in M_{vir} of `VELA2b-29` at $z \approx 2.75$, `VELA2b-27` at $z \approx 2.25$, and `VELA2b-23` at $z \approx 1.25$. The mergers created corresponding peaks in the SFR. None of the galaxies are quiescent, with the sSFR$> 10^{-11}$ yr^{-1} for all snapshots. While the galaxies grow throughout the times studied here most of their mass had already been established before z=4, the earliest snapshot used. On average the galaxies have 90% of their z=1 stellar mass already formed at z=4 and 94% of their virial mass.

Table 2.3. Final Properties of `VELA` Runs

Number	Final z	M_{vir} [$M_\odot$]	M_* [$M_\odot$]	SFR [$M_\odot$ yr^{-1}]	sSFR [yr^{-1}]
21	1.0	12.0	10.9	8.3	-10.0
22	1.0	11.8	10.7	1.5	-10.6
23	1.0	11.7	10.4	7.5	-9.5
24	1.2	11.6	10.3	1.3	-10.2
25	1.0	11.5	10.2	0.6	-10.4
26	1.0	11.6	10.4	1.0	-10.4
27	0.9	11.6	10.3	0.7	-10.4
28	1.0	11.3	9.9	0.2	-10.6
29	1.0	12.0	10.6	5.3	-9.9

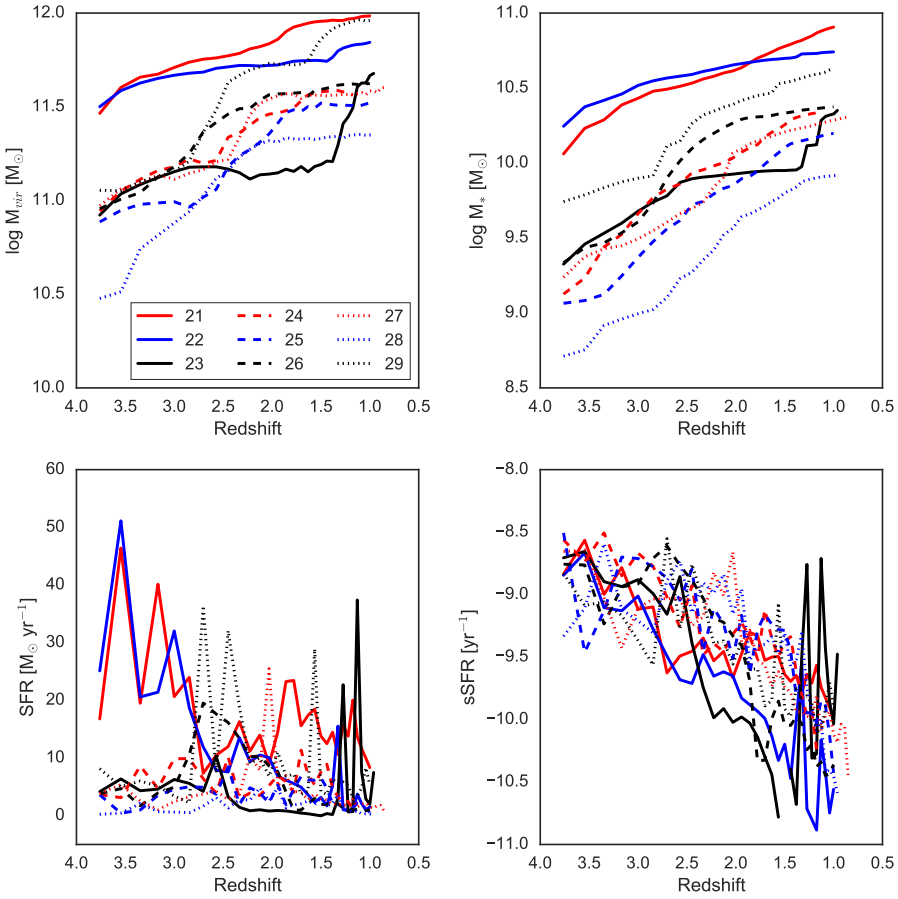

Fig. 2.1.— The mass and star formation histories of the VELA simulations. Shown here are the virial mass M_{vir} (*upper left*), stellar mass M_* (*upper right*), star formation rate SFR (*lower left*), and specific star formation rate sSFR (*lower right*).

2.3. ANA

The remainder of this chapter details the methods used to analyze the simulated galaxies.

The first step in processing the simulation outputs was to convert between the raw outputs to a data format that is easier to process. The simulation outputs were stored in unformatted binary for faster reading and writing, as well as smaller

file sizes. The cost of these benefits is making the files difficult to work with, as well as impossible for humans to read. In order to work with the data each code must read in the unformatted Fortran. To reduce redundancies and the possibilities of error a code named `ANA` was written to interpret the simulation outputs and write them out plain ASCII. `ANA` is a Fortran code and was initially written by Daniel Ceverino as a part of his doctoral work, with significant additions by Kenza Arraki.

`ANA` has multiple purposes. As stated, the primary purpose is to convert the unformatted binary format to plain ASCII, enabling the output to be read in by any coding language. It also selects out a small sample of the cosmological simulation that is of interest. In the zoom-in simulations used, a galaxy was simulated with high spatial resolution only around the selected halo, resulting in only a small portion of the initial large cosmological volume that was simulated with high enough resolution to be useful. In order to facilitate ease of working with the data, ANA selects out a smaller volume around the center of the DM halo as determined by the halo finding code `Rocktar` (Behroozi et al. 2013b).

The size of the smaller box is measured in units the galaxy's virial radius, R_{vir}. By default it is selects a box of length 6 R_{vir} along a side with the galaxy at the center. The coordinates of all DM particles, stellar particles, and gas cells are converted to a new reference frame where the center of the galaxy is at the origin.

`ANA` also performs necessary unit conversions. For each gas cell, the `ART` code keeps track of a several parameters to define the state of the gas such as the spatial location, metal content, and internal energy. The location and velocities

are calculated in code units during the simulation's run; ANA converts these values to physical units, namely parsecs distances and km/s for velocities. The energy content of the cell is convert to temperature in units of Kelvin, and the density is converted from code units to number of hydrogen atoms per cubic centimeter.

For the purposes of this work, the last useful parameter calculated by ANA is the rotation matrix which defines the orientation of the galaxy relative to the orientation of the small box. The orientation of the galaxy is defined by a new coordinate system with the z-axis aligned with the galaxy's rotation axis as defined by the cold gas. The rotation matrix is vital for controlling the orientation of the galaxy when running lines of sight through the box and is discussed more fully in §2.5.2.

The output of ANA is a small box containing all information about the gas cells in the high resolution part of the simulation. The columns of the file and their units are shown in Table 2.4.

2.4. MOCKSPEC

The MOCKSPEC code was designed to examine the simulated CGM through the application of mock quasar absorption line studies. The first step to analyzing the output of ANA is to solve for the ionizatoin correction. The simulations do not track the distribution of specific elements nor their ionization state. The distribution of metals is tied into the metal mass fraction due to SNII and SNIa. The mass fractions need to be combined with the cell density to calculate the number density of each element to be examined. Then the ionization correction of the element needs to be calculated to determine the number density of the ion

of interest. The ionization correction is handled by the HARTRATE code written by Chris Chruchill and is detailed in Churchill et al. (2014).

After HARTRATE converts the gas boxes into ion boxes the data is ready for the mock quasar absorption analysis. The rest of the process is performed by a code named MOCKSPEC. The code follows the following structure:

1. Generate lines of sight (LOS)
2. Run the lines of sight through the ion boxes and identify the gas cells that lie along the LOS.
3. Determine the path length of the line of sight through each cell to calculate its column density contribution
4. Generate the synthetic spectrum based on the column density of the ion, kinematics and the instrument selection
5. Analyze the spectrum to calculate the equivalent width and AOD column density
6. Determine which cells are actually responsible for the observed absorption

Each step is controlled by a separate code. MOCKSPEC is the driver that unifies everything into a single structure.

MOCKSPEC and all of its required sub-codes are publicly available in a GitHub repository at https://github.com/jrvliet/mockspec.

MOCKSPEC is a python code, written with python 2.7. In its current state it is not compatible with python3. The code is controlled by a single control file, which

contains the information on what simulations are going to be analyzed and flags to turn on or off various parts of the pipeline. The file is named mockspec.config and a sample version is contained in the controls directory in the mockspec repository. The control file contains the following fields that need to be updated for every run:

- **GalID:** The root of the ion box file name. The GalID uniquely identifies which simulation the galaxy came from and which halo it is. Examples are D9o2, which is the ninth halo in the dwarf simulation run using feedback prescription o2.

- **Expansion parameter:** The expansion parameter, a, of the simulation output that is being used, which is related to the redshift by $a = \frac{1}{z+1}$ and is written to three decimal points. `MOCKSPEC` uses expansion parameter and not redshift since the simulation snapshots are output in equal steps of expansion parameter.

- **Number of LOS:** The number of lines of sight to generate and run through the simulation. The default is 1000. The maximum value is 9999 due to filename conventions in some parts of the pipeline.

- **Maximum impact parameter:** The largest impact parameter to use when generating LOS, in units of R_{vir}. The default is 1.5, since the CGM is mostly confined to be within 1 R_{vir} which effectively includes all observable material. Care must be taken if this value is increased. The maximum impact parameter is limited by the size of the gas box output by `ANA`. By default, `ANA` creates a box where the largest distance any gas cell can be

from the galaxy is $\sqrt{3} \sim 1.73$ R_{vir}. At the farthest corners, the LOS would run into edge effects. In order to equally compare absorption along an LOS at the far edges of the CGM to absorption closer to the galaxy, both LOS must have comparable path lengths through the box. Absorption strength depends on the column density of material along the path of the LOS, which is given by $N_{ion} = n_{ion}L$ where n_{ion} is the number density of particles along the LOS and L is the path length of the LOS. If weaker absorption is detected at large impact parameters compared to small impact parameters and the LOS do not have comparable path length, then it would be impossible to disentangle what is actually causing the lack of absorption at large impact parameters. Thus the maximum impact parameter should be kept at 1.5 R_{vir} or lower unless `ANA` is changed to output a bigger gas box.

- **Galaxy inclination:** The inclination of the galaxy to use. The inclination is used when generating the LOS and is discussed more in §2.5.1. An inclination of $i = 0$ corresponds to a face-on view of the galaxy and $i = 90$ corresponds to an edge-on view.

- **Equivalent width (EW) cut:** A possible cut to not include absorption with an equivalent width less than this value, given in angstroms. The default is to zero, which still implements an effective equivalent width cut due to the noise added to the spectrum. The noise could obscure weaker absorption and result in a non-detection.

- **Signal-to-Noise:** The signal-to-noise ratio (SNR) the generated spectrum should have. The default is set to 30. The presence of noise imposes an effective EW cut on the detections as the noise will overwhelm very weak

absorption features. For SNR = 30, the effective EW cut is ∼0.05 Å.

- **Number of processors to use:** The most computationally intensive part of the code is `CELLFINDER`, discussed in §2.5.2. It has been parallelized to help speed up the calculations. This field sets how many processors should be used by cellfinder. No other part of `MOCKSPEC` is parallelized.

- **Root location:** No longer used

- **Percent EW change:** The last part of `MOCKSPEC`, `SIGCELLS`, determines which cells along the line of sight are actually the source of the observed absorption. The process is described fully in §2.5.6. The default is 5 per cent.

- **Flags:** The next section of mockspec.config is list of all the parts of the pipeline along with flags. If the flag is set to 1, the corresponding code is run. Otherwise, the code is skipped. This setting is useful if the user wants to rerun the pipeline for a reason that only affects a late code, such as testing the effect of changing the SNR. The ion boxes do not need to be generated again and the code should use the same LOS, so everything before `LOS7` could be turned off.

- **Ions:** The last section of mockspec.config is a list of all the ions to be included in the analysis. There is no limit to the number of ions that can be included. For each ion, there are three parameters to be filled in. The first column is the name of ion in typical absorption style, such as HI, MgII, or CIV. The next column is how much the abundance of the element should be artificially increased during the `HARTRATE` code. This value should be zero

for all except magnesium, which defaults to 0.5. The last column is which instrument to use. In SPECSYNTH, the spectrum in convolved with the instrument's ISF to accurately replicate observations. Available instruments are found in Mockspec.instruments, found in the control directory. The instruments included by default are shown in Table 2.5. If additional instruments are desired, this file can be updated with the relevant information.

To run MOCKSPEC, the user needs to copy only the control file to the working directory and run the master code file, mockspec.py, from there. The code handles the directories that get made and copying all required files to the correct location.

2.5. Ionization Correction

After ANA the metal content of the gas cells are contained in the SNII and SNIa columns which contain the mass fraction of metals contributed by Type II supernovae (Z_{SNII}) and Type Ia supernovae (Z_{SNIa}), respectively. For the purpose of generating mock absorption features the code needed to determine the number density of various ions in their correct ionization state, such as O VI or Mg II. The conversation has two steps: (1) Convert Z_{SNII} and Z_{SNIa} to number density of the atom of interest (i.e. n_O or n_{Mg}), then (2) apply an ionization correction to get the number density of the actual ion. The code to perform these steps for each cell in the simulation is HARTRATE, developed by Chris Churchill, and is detailed in Churchill et al. (2014). A brief overview of the code follows.

The first step requires knowing the abundance ratios of each element in the SNII and SNIa. For SNII mass fractions, HARTRATE use the production factors from the models of Chieffi & Limongi (2013). For SNIa mass fractions, HARTRATE

Table 2.4. Contents of the GZ file Output by `ANA`

Field	Description	Units
cell_size	The length of one side of the cell	parsecs
x	x-coordinate of the center of the cell	kiloparsecs
y	y-coordinate of the center of the cell	kiloparsecs
z	z-coordinate of the center of the cell	kiloparsecs
vx	x-component of the cell's velocity	kilometers per second
vy	y-component of the cell's velocity	kilometers per second
vz	z-component of the cell's velocity	kilometers per second
density	Number denstiy of hydrogen in the cell	atoms per cubic centimeter
temperature	Temperature of the cell	Kelvin
SNII	Fraction of the cell's mass contained in metals from Type II supernovea	None
SNIa	Fraction of the cell's mass contained in metals from Type Ia supernovea	None

Table 2.5. Instruments Available for `MOCKSPEC`

Name	Short Name	Telescope	Resolution	Wavelength Range [nm]
Cosmic Origins Spectrograph Near-UV	COSNUV	Hubble	18000	115 – 178
Cosmic Origins Spectrograph Far-UV	COSFUV	Hubble	22000	115 – 320
DEep Imaging Multi-Object Spectrograph	DEIMOS	Keck	5000	410 – 1100
High Resolution Eschelle Spectometer	HIRES	Keck	45000	300 – 1000
Ultaviolet and Visual Echelle Spectrograph	UVES	VLT	45000	300 – 1100
Low Resolution Imaging Spectrometer	LRIS	Keck	4000	320 – 1000

uses the yields from the C series DD2 models of Iwamoto et al. (1999).

The mass fractions of each atomic species k are denoted as $(x_k)_{II}$ and $(x_k)_{Ia}$ for SNII and SNIa respectively. For hydrogen ($k = 1$) and helium ($k = 2$), x is zero. The metal mass fractions are rescaled by a constant to recover the original mass fraction in the cell:

$$Z_{II} = C_{II} \sum_{k=3} (x_k)_{II} \tag{2.1}$$

$$Z_{Ia} = C_{Ia} \sum_{k=3} (x_k)_{Ia} \tag{2.2}$$

The hydrogen and helium mass fractions need to be rescaled as well to ensure $\sum_k = 1 x_k = 1$. Since these elements are only included in type II ejecta, the parameter $r = (x_2)_{II}/(x_1)_{II}$ is used:

$$x_1 = \frac{1 - (Z_{II} + Z_{Ia})}{1 + r} \tag{2.3}$$

$$x_2 = r x_1 \tag{2.4}$$

$$x_k = C_{II}(x_k)_{II} + C_{Ia}(x_k)_{Ia} \tag{2.5}$$

Once the number densities of each element of interest is known the number density of each ionization state can be determined. `HARTRATE` assumes the gas is in ionization equilibrium, an assumption that generally holds. In Oppenheimer & Schaye (2013b) they investigated the effect of dropping this assumption. Non-equilibrium effects tend to boost the degree of ionization and reduce cooling efficiencies. The effect is more important if the background ionization field is neglected. While `HARTRATE` does not account for non-equilibrium effects, it does include the ultraviolet background (UVB) from Haardt & Madau (2011).

The current form of HARTRATE assumes all gas is optically thin which means there is no attenuation of the ionizing radiation field anywhere in the simulation. All gas cells see the same ionizing field. For the vast majority of the CGM this is a safe assumption. The assumption breaks down near the galaxy or near satellites where the gas density gets high enough. A proper treatment of the radiation field would require a full radiative transfer treatment which is computationally intense. A common simplified solution is to assume all gas cells with a hydrogen density above a certain cut are fully shielded. Typical values are $n_H > 0.01$ cm^{-3}. Cells that meet this criteria have all their hydrogen in the H I state and all magnesium in the Mg II state (e.g. Ford et al. 2013). The consequence of not including any optical depth considerations is that HARTRATE may underpredict ions that typically reside in optically thick clouds such as Mg II.

The output of HARTRATE is a copy the simulation gas box for each ion. In addition to the data in Table 2.4 the box also has the fields specific to each ion shown in Table 2.6.

Table 2.6. Contents of the GZ file Output by HARTRATE

Field	Description	Units
nAtom	Number density of the atomic species (e.g. carbon)	cm^{-3}
fIon	Fraction of the atomic species in the desired ionization state (e.g. CIV)	None
nIon	Number density of the ion (e.g. CIV)	cm^{-3}
alpha_sol	Solar abundance of the atomic species)	None
alpha_Zmet	Metallicity of the cell	solar units
t_ph	Photoionization timescale	log years
t_rec	Recombination timescale	log years
t_coll	Collisional ionization timescale	log years
t_cool	Cooling timescale	log years

2.5.1. Generating Lines of Sight

Once the ion boxes are made then lines of sight are generated using a code called `GENLOS`. The lines of sight are generated based on the maximum impact parameter, the galaxy's virial radius, the galaxy's inclination, and the galaxy's rotation matrix. The rotation matrix describes how the galaxy is rotated relative to the simulation box output and is generated by `ANA`.

There are three coordinate systems used in `GENLOS` code: box, galaxy, sky. All coordinates systems are centered on the galaxy and the only difference is how they are rotated. The box coordinate system is the one used by the simulation. After `ANA` this coordinate system is centered on the galaxy. The galaxy coordinate system depends on the rotation of the galaxy. The z-axis is along the angular momentum vector as defined by the cold gas. The disk of the galaxy lies in the xy-plane. The sky coordinate system is how the user would observe the system. The xy-plane is in the plane of the sky and the z-axis is pointed towards the observer.

To translate from one coordinate system to another requires using a rotation matrix. An example of a rotation matrix to move from one coordinate system to a new one that is rotated about the x-axis by an angle θ is:

$$a = \begin{bmatrix} 1 & 0 & 0 \\ 0 & \cos(\theta) & -\sin(\theta) \\ 0 & \sin(\theta) & \cos(\theta) \end{bmatrix}$$

To translate from the sky plane to the galaxy frame, the coordinates are rotated around the x-axis by the inclination angle i. The rotation matrix for the

translation, defined as a_{stg}, is given by:

$$a_{stg} = \begin{bmatrix} 1 & 0 & 0 \\ 0 & \cos(i) & -\sin(i) \\ 0 & \sin(i) & \cos(i) \end{bmatrix}$$

To reverse the direction of the translation (go from the galaxy to sky frame), the new rotation matrix is the inverse of the original:

$$a_{gts} = a_{stg}^{-1}$$

The rotation matrix given by `ANA` describes how to rotate from the box frame to the galaxy frame:

$$a_{btg} = \begin{bmatrix} a11 & a12 & a13 \\ a21 & a22 & a23 \\ a31 & a32 & a33 \end{bmatrix}$$

The lines of sight are defined by three parameters:

1. Impact parameter b: The perpendicular distance between the line of sight and the center of the galaxy.

2. Impact angle ϕ: The angle between the sky's z-axis and the vector connecting the center of the galaxy to the line of sight.

3. Inclination i: Angle between the z-axis of the galaxy frame and the z-axis in the sky frame.

Since the z-axis of the sky frame is aligned to point towards the observer, all LOS have the same directional vector in the sky frame, $\overrightarrow{d_s}$:

$$\overrightarrow{d_s} = \begin{bmatrix} 0 \\ 0 \\ -1 \end{bmatrix}$$

To define a line a point in space is needed along with the directional vector. This point, denoted by the position vector $\overrightarrow{p_s}$, is set by selecting the impact parameter and the impact angle of the LOS. The impact parameter is randomly selected from a uniform distribution of values between zero and the maximum impact parameter. The impact angle is randomly selected from a uniform distribution between zero and 360 degrees. Using this point, the position vector is given by:

$$\overrightarrow{p_s} = \begin{bmatrix} b\cos(\phi) \\ b\sin(\phi) \\ 0 \end{bmatrix}$$

The end goal is to define the line of sight in terms of the box coordinate system, so the sky frame needs to be translated to the galaxy frame:

$$\overrightarrow{d_g} = a_{stg} \times \overrightarrow{d_s}$$

$$\overrightarrow{p_g} = a_{stg} \times \overrightarrow{p_s}$$

Then to rotate into the box frame:

$$\overrightarrow{d_b} = a_{gtb} \times \overrightarrow{d_g}$$

$$\overrightarrow{p_b} = a_{gtb} \times \overrightarrow{p_g}$$

The last step is to change the description of each LOS from being defined by a point and a directional vector to being defined by two points. The two points are where the line of sight intersects with the edges of the gas box.

The process is repeated for each LOS desired, then sorted by increasing impact parameter. For the rest of `MOCKSPEC` the LOS number is proportional to the impact parameter of the LOS.

The output of this step is two files named lines.dat and lines.info. The lines.dat file is used by `CELLFINDER` in the next step of the pipeline. It contains the entrance and exit points of each line of sight. The lines.info file is not used by any code and is for the user's information only. It contains the impact parameter and the impact angle for each line of sight.

2.5.2. Identifying Intercepted Cells

With the lines of sight defined the next step is to use `CELLFINDER` to run the lines through the simulation to identify which cells lie along the LOS and thus can contribute to absorption. `CELLFINDER` is the most computationally intensive part of `MOCKSPEC` and thus is the only code that is parallelized.

The process under which cellfinder works is fairly straightforward. For each LOS, `CELLFINDER` moves through each gas cell in the simulation. It then calculates the minimum distance between the center of the cell and the line of sight. If that

distance is less than the size of the cell, it is counted as contributing to absorption along the line of sight.

The method used by `CELLFINDER` is a brute force method. For each LOS, it scans through the entire box. Small simulation boxes, such as a high-z dwarf galaxy, have $\sim 10^{5-6}$ cells. Large boxes can have upwards of 10^7 cells. Cycling through every cell for every LOS is inefficient. A better alternative would be a linked list system. This structure would contain the information about which cell is bordering the current cell, drastically cutting down on the number of cells that need to checked if they are intercepted by the LOS. However, a linked list with this information is not simple to make and is very time consuming to construct. Running the LOS through the box once is comparable in time usage as constructing a linked list. The benefit would only come with running LOS through the box multiple times, something that is not often done.

Additionally, relying on linked lists would limit possible future uses for `MOCKSPEC`. In its current state, `MOCKSPEC` only works on ART simulations. There is little reason it could not be adapted to other simulation codes in future developments. The current method could be applied to other AMR and even SPH outputs with relatively minor modifications. Linked lists would be beneficial for other AMR codes, but would be useless for any SPH codes. Linked lists were not implemented because the benefit is small for the development cost and it limits possible other uses.

The output of `CELLFINDER` is a list of cell identification numbers. A Python code called `IDCELLS` reads through the ion boxes output by `HARTRATE` and generates a file for each LOS containing a list of cellIDs along the line of sight. A

second code is run after GENLOS that cycles through the cellIDs and selects out the details of the cell for each ion being studied. It outputs a file named containing all information about the cell from the ion box, removing any need for any following codes to read in the massive ion box.

2.5.3. Path Length

The rest of the pipeline is ion specific. MOCKSPEC creates a directory in the working directory for each ion that contains the output from the rest of the pipeline.

The output of CELLFINDER contains all cells the LOS intercepts. The column density contribution of each cell is needed to generate the spectrum, which requires knowing the path length of the LOS through the cell. The code that calculates the column density contribution of each cell is LOS7 and is detailed below.

For each LOS, LOS7 examines each cell identified as laying along the LOS by CELLFINDER and calculates its line-of-sight properties, namely the distance the cell lies along the LOS S_{LOS}, its velocity parallel to the LOS v_{LOS}, and the redshift and velocity of the absorption caused by the cell z_{LOS} and v_{abs}:

$$S_{LOS} = l(x\_x_{gal}) + m(y - y_{gal}) + n(z + z_{gal})$$

$$v_{LOS} = lv_x + mv_y + nv_z$$

$$z_{LOS} = z_{box} + (1 + z_{box})\frac{v_{LOS}}{c}$$

$$v_{abs} = c\frac{z_{LOS} - z_{gal}}{1 + z_{gal}}$$

Here l, m, and n are the directional cosines of the LOS. The path length D of the LOS through the cell is then calculated and used to determine the parameters of the cell that are used to generate the spectrum:

$$N = n_{ion}D$$

$$b = 10^{-5}\sqrt{\frac{2k_BT_{cell}}{m_{ion}}}$$

where N is the column density contribution of the cell, n_{ion} is the number density of the ion in question in the cell, b is the Doppler b parameter, k_B is Boltzmann's constant, and m is the mass of the ion in question. These parameters are calculated for every cell in returned by `CELLFINDER` and output into files for the next code to use.

2.5.4. Generating Spectra

The synthetic spectra are generated with the `SPECSYNTH` code. The full details of the methods used are detailed in Churchill et al. (2015). A brief overview is given here.

The optical depth contribution of each cell, i, to the absorption is first determined for each ion. For each observed wavelength, the optical depth $\tau_i(\lambda)$ of contribution of each cell is given by

$$\tau_i(\lambda) \;=\; N_i \frac{\sqrt{\pi} e}{m_e c^2} \frac{f \lambda_0^2}{\Delta \lambda_i} U(a,b)$$

were λ_0 is the rest-frame wavelength of the transition, f is the oscillator strength of the transition, N_i is the column density of the ion in cell i, $U(a,b)$ is the Voigt function and $\Delta\lambda$ is the Doppler width given by

$$\Delta \lambda_i \;=\; \frac{\lambda_0}{c} \sqrt{\frac{2kT_i}{m}}$$

where m is the mass of the ion. The Voigt function is computed using the methods described in Humlek (1979). Once the optical depth of each cell is computed the normalized flux incident on the "detector" can be computed from

$$\mathcal{I}'(\lambda) \;=\; \prod_{i=1}^{n_c} \exp(-\tau_i(\lambda)).$$

The final step is to simulate the effect of the instrument. The primary effects are a convolution with the instrumental spread function (ISF), pixelization, and added noise terms. Convolving the incident flux ($\mathcal{I}'(\lambda)$) with the ISF ($\Phi(\lambda' - \lambda)$) results in the normalized instrument convolved spectrum ($\mathcal{I}(\lambda)$)

$$\mathcal{I} \;=\; \Phi(\lambda' - \lambda) * \mathcal{I}'(\lambda')$$

The next instrumental effect is pixelization. The current flux is a smooth function of λ but instruments only measure flux as set bins of λ described by the pixelization $\Delta\lambda_{pix}$ which differs for each instrument. To mimic this effect the incident flux $\mathcal{I}$ is sampled with $\Delta\lambda_{pix}$ taking the mean value of the flux within each pixel.

The last step to create the final spectrum is to add noise to the spectrum. The code simulates the read noise (RN) of the instrument and a Gaussian noise based on the input signal to noise ratio (SNR). To add noise to the synthetic spectrum an uncertainty spectrum $\sigma_{\mathcal{I}}(\lambda)$ is created using

$$\sigma_{\mathcal{I}}(\lambda) = \frac{\sqrt{\mathcal{I}_c \mathcal{I}(\lambda) + \mathrm{RN}^2}}{\mathcal{I}}_c,$$

$$\mathcal{I}_c = \frac{1}{2}\left(\mathrm{SNR}^2\right)\left[1 + \sqrt{1 + 4\frac{\mathrm{RN}^2}{\mathrm{SNR}^2}}\right].$$

The term $\mathcal{I}_c$ approximates the continuum for the SNR. For additional details, see Churchill (1997). When processing observations an additional source of uncertainty arises when removing the continuum from the spectrum. The `MOCKSPEC` pipeline does not include the spectrum of the background source so this uncertainty needs to be modeled in. The code applies the approximation detailed in Sembach & Savage (1992) that the continuum placement uncertainty is proportional to the Poissonian uncertainty in the continuum yielding

$$\sigma_{contin}(\lambda) = h\sigma_{\mathcal{I}}^2(\lambda).$$

The constant of proportionality h was determined experimentally to be $h = 0.4$. Combining the sources of noise in quadrature yields the full uncertainty spectrum

$$\sigma(\lambda) = \frac{1}{\mathcal{I}_c}\sqrt{\mathcal{I}_c \mathcal{I}(\lambda) + \mathrm{RN}^2 + h^2\left[\mathcal{I}_c + \mathrm{RN}^2\right]}$$

With the full uncertainty spectrum the final spectrum can be calculated using

$$I(\lambda) = \mathcal{I}(\lambda) + G_{pix}\sigma(\lambda),$$

where G_{pix} is a random value selected from a unit Gaussian distribution on a per pixel basis.

2.5.5. Sysanal

A strength of the `MOCKSPEC` code is its ability to automatically analyze the absorption profiles it generates. The function `SYSANAL` automatically identifies significant absorption features in the outputs of `SPECSYNTH` and calculates its EW and apparent optical depth (AOD) column density of the intervening material.

The method of identifying which spectra have significant absorption features are described fully in Churchill & Charlton (1999); Churchill et al. (2000) where itself was derived from methods described in Schneider et al. (1993). A brief overview is included in this section.

The first step in detecting absorption features is to convert the spectrum to an equivalent width spectrum, $w(\lambda)$ and its associated uncertainty spectrum $\sigma_w(\lambda)$. The equivalent width spectrum is determined by convolving a normalized, pixelized form of the ISF with the each pixel of the spectrum. The result is a spectrum where each resolution element is the observed equivalent width as a function of wavelength.

The two equivalent width spectra are used to define where absorption features are found by identifying the wavelength range over which $w(\lambda) \leq -N\sigma_w(\lambda)$. The value for N can be changed to mimic methods used by various observational surveys and has a default value of 5 for singlet lines. If the transition is doublet

only the blue transition uses $N = 5$ while the red transition uses $N = 3$. Both transitions must have detected absorption for the feature to be identified as a region of significant absorption. If there are no regions of significant absorption detected ($w(\lambda) > -N\sigma_w(\lambda)$ for all wavelengths) then the 3σ upper limits are recorded.

Once the areas of significant absorption features are identified the wavelength edges to the features need to found. Starting from the center of the absorption feature as identified by $w(\lambda) \leq -N\sigma_w(\lambda)$ and moving redward, the upper limit of the feature is marked where $w(\lambda) \geq -1\sigma(\lambda)$. The lower limit is likewise found by traveling blueward of the significant absorption range.

Using the wavelength limits of the absorption features the total equivalent width is computed. If the transition is a doublet then the doublet ratio is also computed. Additionally the code computes the flux decrement weighted velocity centers, velocity widths, and velocity asymmetries along with all related uncertainties.

There are several methods to determine the column density of the absorbing medium, but many, such as VP decomposition, are difficult to automate. The `SYSANAL` code computes the AOD column density as it can be reliably automated. The AOD column density spectrum for each ion ($N_a(\Delta v)$ is calculated using the methods described in Savage & Sembach (1991). The total AOD column density is found by integrating the AOD column density spectrum over the velocity window found previously.

A limitation of the AOD method is in the event of saturation. The AOD method effectively adds up the apparent optical depth in each pixel of the spec-

trum. If any pixel of the spectrum is saturated (i.e. $I(\lambda) = 0$) the AOD method will only be able to apply a lower limit the column density.

2.5.6. Identifying Significant Cells

One of the main goals of `MOCKSPEC` is to determine the physical properties of gas that creates absorption features. Modeling observations can give insights into what kind of gas likely creates the gas, but techniques are limited. Voigt profile fitting determines the column density and Doppler b parameter ($b = \sqrt{2kT/m}$) of the absorption. The process of fitting Voigt profiles to the absorption features is complicated and difficult to automate. Voigt profiles also have built-in assumptions that may not be valid, such as absorption clouds arising from isothermal, coherent structures.

One of the main difficulties in determining the nature of the absorbing gas is due to the fact the strength of the absorption is dependent on the column density, which in turn depends on the number density n and the path length L through the absorbing gas. The dual dependence introduces a degeneracy: the same absorption feature can be created from a small dense cloud as from a large diffuse cloud.

There are ways to break the degeneracy, but they have their own difficulties. A common method is to model the ionization parameters of the gas. Gas can be ionized through three primary methods: collisional ionization, photoionization, and cosmic ray ionization.

The rates of collisional ionization depends on the density and temperature of the gas. Higher densities and higher temperatures both increase the rate at which

atoms collide with each other, increasing the ionization rate. The temperature of the gas can be determined from the b parameter from Voigt profile fitting with the assumption that the broadening of the line is dominated by thermal motion and not turbulence. If collisional ionization is the dominant form of ionization for the gas the knowledge of the its temperature puts a limit on the density of the gas, which puts a limit on the path length of the gas when combined with the column density.

If photoionization is the primary method for ionizing the gas it is harder to put limits on the size of the absorbing structure. If the cloud becomes too dense, it will start to become optically thick, limiting the ability of a background ionization field to ionize the gas. If the gas is primarily photoionized, there is an upper limit on how dense the cloud can be, which puts a lower limit on the size of the cloud when combined with the column density. If the gas arises in an optically thick cloud the limit instead becomes an upper limit on the density and consequently an upper limit on the size of the cloud.

A notable benefit of studying mock absorption features from simulations is knowing the true properties of the absorbing structures. Knowing the nature of the gas that is actually causing the absorption enables a test of observational techniques to measure how accurately the methods can determine the absorbing gas' properties. However to do this `MOCKSPEC` needs to be able to determine which gas cells are actually causing the absorption features.

In the process of generating spectra `MOCKSPEC` uses several criteria to determine which gas cells to utilize. The initial cut occurs during `CELLFINDER` where only cells that are intersected by the line of sight are selected. The selection

is tightened during LOS7 when the column density contribution of each cell are calculated. Only cells with an ion column density contribution greater than 10^9 cm^2 are included in the lines files. Cells with an ion column density less than this limit are too diffuse in the ion to contribute significantly to the absorption feature. Observations struggle to detect absorption features from systems with column densities less than 10^{16}. It would take over one million cells with individual column densities of 10^9 in a coherent structure to be observed which does not occur in the simulations.

The final cut is performed in the function SIGCELLS. The goal of this code is to identify which cells were actually responsible for the detected absorption. Typically a few hundred gas cells lie along a given LOS. However not all of the cells contribute equally to the absorption features. Briefly, the SIGCELLS determines which cells account for 95% of the absorber's strength as quantified by the equivalent width. The process relies on the lines files output by LOS7. The cells are sorted into decreasing column density then systematically removed until the spectrum created by the remaining cells has an equivalent width that is 95% of the equivalent width of the original spectrum. The spectrum are created with zero noise to remove any randomness to the process. Typically the number of cells identified as significant was around 10-30, compared with the $\sim$100 initally along the LOS.

The cells are removed using a bisect method. For a line of sight that involves n cells the procedure removes the $n/2$ smallest cells from the lines file and generates a new spectrum with zero noise. The equivalent width of the spectrum EW_{cut} is then compared to the equivalent width of a noise-less spectrum from the full n cells, EW_{full}. If the difference $\Delta EW = EW_{full} - EW_{cut}$ is less than $0.05 * EW_{full}$,

then the cut was too small and more cells need to be removed. The new cut point is then set to $n/4$ and the process is repeated. If $\Delta EW > 0.05 EW_{full}$, then the cut was too deep and less cells need to be removed. The new cut is set at the $3n/4$ biggest cells and then repeated. On all subsequent cycles, the difference between the old cut and the new cut will be n/i^2 where i is the iteration count. When the difference between the new cut and the old cut is less than one cell, the method has found the solution and returns the final list.

2.6. Outputs

The final outputs of `MOCKSPEC` are two files for each ion. The first is a culmination of the output of `SYSANAL`. This file contains all the observed properties of the absorption and is detailed in Table 2.7.

The second file contains the properties of the significant cells as determined by `SIGCELLS` and its contents are detailed in Table 2.8.

The final output files are stored using the HDF5 file format (The HDF Group 1997-2017) which creates files that take up roughly half of the disk space as plain ASCII while still remaining easy to access with any programming language.

2.7. Limitations and Future Development

Currently `MOCKSPEC` is in a stable form. It can be run on any simulation generated by `ART` after it has been processed by `ANA`. It generates synthetic spectra for multiple lines of sight through the simulation, controlling for impact parameter and inclination. It is able to generate generate synthetic spectra for any ionization state for any element from hydrogen to zinc. It replicates the effect of

Table 2.7. Results contained in absorption data files from `SYSANAL`

Variable	Description	Units
los	LOS number	–
D	Impact parameter	kpc
phi	Azimuthal angle	deg
zabs	Redshift of the absorption	–
v-	Lower velocity edge of absorption feature	km s^{-1}
v+	Upper velocity edge of absorption feature	km s^{-1}
EW_r	Rest frame equivilent width	Angstroms
dEW_r	Uncertainty in EW_r	Angstroms
DR	Doublet Ratio	–
dDR	Uncertainty in DR	–
SL	Signifigance level of detection	–
Vbar	Central velocity of detection	km s^{-1}
dVbar	Uncertainty in Vbar	km s^{-1}
Vsprd	Velocity spread of absorption	km s^{-1}
dVsprd	Uncertainty of Vsprd	km s^{-1}
Vasym	Velocity asymmetry of absorption	km s^{-1}
dVasym	Uncertainty in Vasym	km s^{-1}
lgt	Log optical depth of absorption	–
dtau-	Lower uncertainty in lgt	–
dtau+	Upper uncertainty in lgt	–
logN	Log AOD column density	log cm^2
dNcol-	Lower uncertainty on logN	log cm^2
dNcol+	Upper uncertainty on logN	log cm^2

Table 2.8. Results contained in absorbing cells files from `SIGCELLS`

Variable	Description	Units
LOS	LOS number	–
D	Impact parameter	kpc
cellID	Cell's ID number	–
redshift	Redshift of the cell	–
logN	Column density of the cell	–
dobbler_b	Doppler b parameter of the cell	–
x	x-coordinate of the cell (box frame)	kpc
y	y-coordinate of the cell (box frame)	kpc
z	z-coordinate of the cell (box frame)	kpc
vx	x-component of cell's velocity (box frame)	km s^{-1}
vy	y-component of cell's velocity (box frame)	km s^{-1}
vz	z-component of cell's velocity (box frame)	km s^{-1}
r	Galactocentric distance of the cell	kpc
nH	Number density of hydrogen	cm^{-3}
temperature	Temperature of cell	K
cell_size	Length of cell's side	kpc
SNII	Mass fraction of metals from Type II SNe	–
SNIa	Mass fraction of metals from Type Ia SNe	–
alpha_Zmet	Metallicity of cell	solar
ion_density	Number density of the ion	cm^{-3}

several instruments, including HIRES, COS, and UVES, and adding additional instruments is simple. The outputs of MOCKSPEC include the equivalent width and AOD column density of all detected absorption, as well as the physical properties of the cells that are responsible for the absorption.

MOCKSPEC is not without shortcomings however. The primary limitation is the restriction to ART simulations. While ART is a powerful and useful simulation code, there are several other codes available. It would be of great interest to compare the results of MOCKSPEC of ART simulations to the results of other codes, such as ENZO (Bryan et al. 2014), GADGET (Springel 2005), or GIZMO (Hopkins 2014).

The difficulty in updating MOCKSPEC to handle other codes lies in altering how the other codes output the location of their metals. In ART the output is a grid throughout all space, and each cell contains some amount of metals. Adapting MOCKSPEC to work for other grid-based code, such as ENZO would be simple.

SPH code such as GADGET would be more difficult. SPH codes take a Lagrangian approach to hydrodynamics, meaning the metal distribution is contained in the metallicity of gas particles that move through the simulation. The particle based gas structures would have to be "deposited" onto a grid that MOCKSPEC could read in for processing. The deposit method is the current method used by the yt code when analyzing SPH simulations.

Another notable shortcoming of MOCKSPEC lies in HARTRATE. This code calculates the ionization balance for the gas in the simulation. It accounts for a great deal of relevant physics as detailed in §2.5, but there are a few notable exclusions. The most pressing issues are in the photoionization calculations. In dense regions ($n_H > 0.01$ cm^{-3} Rahmati et al. (2013)) the absorption of incoming radiation by

the gas becomes significant to reduce the strength of photoionization. Currently this effect is not included in HARTRATE. Most observations of the CGM detect gas more diffuse than this limit so the lack of shielding is not greatly important for higher ionization ions such as O VI and Ne VIII. However low ionization ions, such as Mg II, are often found in gas dense enough to be affected by self-shielding. For this reason, discrepancies between real Mg II observations and mock Mg II observations are expected.

In the photoionization calculation, HARTRATE includes the background ionizing radiation field from Haardt & Madau (2012). However local massive stars and AGN can also generate substantial ionizing radiation. Including the local radiation sources would require HARTRATE to calculate the spectrum of every star particle based on its age and metallicity, and calculate its distance to every gas cell to determine its contribution to the photoionization rate. If shielding is included, then this calculation becomes more difficult as attenuation of the radiation by intervening material would have to be included, requiring a detailed radiative transfer solution to be included. Shen et al. (2013) included the effect of local ionization to the photoionization balance for an L^* galaxy with a SFR = 20 $M_\odot$/yr and found it to be only relevant for gas within 45 kpc of the galaxy. Beyond this distance the extra-galactic UV radiation field dominates. Rahmati et al. (2013) found the contribution to the ionizing radiation from local stars was only important at z=0 for damped Lyman alpha systems with $N_{HI} > 10^{21}$ cm^{-2}. Werk et al. (2014) found the local ultraviolet radiation was not required to created the observed ionization parameters in the CGM of the COS-Halos sample.

When HARTRATE calculates the ionization state it assumes equilibrium, a common assumption as it greatly simplifies the calculations. Oppenheimer & Schaye

(2013b) examined how dropping this assumption alters the resulting ionization balance. They found non-equilibrium effects are important in cool ($T < 10^6$ K) gas and tend to boost the degree of ionization and reduce the cooling efficiencies. However the strength of the effect is small compared to the effect the extra-galactic background has on the ionization balance. Since `HARTRATE` accounts for the extra-galactic background dropping the assumption of equilibrium would have a small effect.

The last shortcoming of `MOCKSPEC` is a result of its history. Several of the functions used in `MOCKSPEC` were developed separately and for other purposes. For example, `SYSANAL` was originally developed to be used interactively and on observations. Each function in `MOCKSPEC` described in this chapter can be run separately. To relay the results from one function to another the outputs of one function are written to file and the next function reads it in. While this structure enables easy testing of each function, it drastically slows down the code. File I/O is one of the slowest functions a code can perform.

The next generation of `MOCKSPEC` will combine everything into one body of code that passes the output of each function to the next one directly which would require a substantial rewrite of several functions. The functions should be unified into a single language as well, ideally Python. The restructure will also be able to handle each LOS in parallel. The conversion to Python would likely slow down the code, but the parallelization would compensate for this loss and lead to a general speed up of the code.

In summary, `MOCKSPEC` is an efficient tool for analyzing the CGM around galaxies created in `ART` simulations. With a runtime of only a few hours `MOCKSPEC`

generates thousands of mock QAL observations while replicating instrumental effects and automatically measures the equivalent width and AOD column density of each detection. It also is the only mock QAL code that identifies the cells responsible for the absorption. This allows for comparisons between the derived physical properties of the absorbing gas from observational techniques and the true nature of the absorbing materials, revealing any potential bias in observational analysis.

3. THE CIRCUMGALACTIC MEDIUM OF DWARF GALAXIES

3.1. Introduction

Dwarf galaxies are the most abundant of galaxies but are also the least understood mass range of galaxies. The low luminosity of dwarf galaxies makes them difficult to observe at any significant distance. Despite their small size ΛCGM predicts dwarfs are a vital part of galaxy evolution as a whole.

One of the consequences of ΛCGM is small galaxies form first with massive galaxies arising from the mergers of small galaxies. Despite the early formation, observations have determined most dwarf galaxies build up their stellar mass after large galaxies in a process called "downsizing" (Neistein et al. 2006). The delayed star formation in dwarf galaxies can be partially attributed to their inability to retain gas during periods of star formation.

The weak gravitational potential allows for easier gas removal from the ISM due to stellar feedback than in more massive galaxies. The winds generated by star formation in dwarf galaxies are also more able to escape the halo entirely and enter the intergalactic medium (IGM). The IGM is mostly formed form primordial gas which should be free of metals, but several observations of the Lyα forest between $z = 2 - 4$ find metal contamination. Schaye et al. (2003) determined the median metallicity of the IGM between $z = 2-4$ to be $[\mathrm{C/H}] \approx = 3.5 + 0.1(z - 3)$. About half of the IGM by mass is contaminated with metals (Simcoe et al. 2004; Pieri & Haehnelt 2004). Simulations have been moderately successful at replicating the IGM contamination with wind ejecta from galaxy (Wiersma et al. 2011). The baryon cycle of dwarf galaxies is thus a vital component of the evolution of universe.

Observing the baryon cycle of dwarf galaxies is difficult. The low luminosity and size of dwarf galaxies restricts the distance from which they can be observed. Surveys of absorber statistics over a large redshift range undoubtedly catch dwarf galaxies in their sample but it is impossible to identify the galaxy responsible for each absorption feature for most surveys. The only survey to target the CGM of dwarf galaxies is the COS-Dwarfs survey which observed the CGM of 44 dwarf galaxies ($L < 0.1\,L^*$) at very low redshift.

Studying the baryon cycle of dwarf galaxies is likewise rare. Most simulations of galaxy evolution to test feedback prescriptions focus on more massive galaxies ($L \sim L*$) as the observational data set available for comparison is much larger and available at high-z so the simulations do not have to run as long. To verify a simulation of a dwarf galaxy the simulation must be run to present day to have any observational data sets to compare to. Shen et al. (2013) simulated a group of seven dwarfs and examined their evolution and CGM. The CGM was analyzed by examining column density spatial distributions derived from 2D projections of the gas distribution. They did not create mock observations and thus their results are difficult to compare to observations.

This chapter describes the analysis of the CGM of three isolated dwarf galaxies using `MOCKSPEC`. The three galaxies were generated by using three different stellar feedback prescriptions to test the impact of radiation feedback on the galaxy and its CGM. The results of the `MOCKSPEC` analysis were compared to the COS-Dwarfs datasets. Additionally the accuracy of commonly used observational techniques such as Voigt Profile fitting were tested.

3.2. Methods

3.2.1. Model Selection

The simulations used to explore the CGM of a dwarf galaxy are detailed in 2.2.2. The full simulation suite produced eight runs using the same DM halo with varying feedback prescription. To simplify the analysis of the galaxy's CGM only a selection of the galaxies were used, specifically model dwSN, dwALL_1, and dwALL_8. The dwSN model was included as the canonical sample. The RP runs (dwRP_1_long, dwRP_10_long, dwRP_50_long) were not found to be significantly different from the dwSN model (see Trujillo-Gomez et al. (2015) for details) and were not included in the CGM analysis. The dwALL_40 model was not included as the value used for the strength of photoheating is far outside limits from observations. The dwALL_8_long model was not included as it was not significantly different from dwALL_8. An example of the output is shown if Figure 3.1.

The goal of the study was to determine which model produces the most realistic CGM as compared to observations. The low luminosity of dwarf galaxies ($L < 0.1L^*$) makes them difficult to observe and restrict observations to low redshift samples. Only snapshots with $z < 0.1$ were used in this study to match observations. The final properties of the three runs used are shown in Table 3.1.

This analysis of the simulations focused on four of the most commonly ob-

Table 3.1. Properties of each dwarf at $z = 0$

Model	M_{vir}	M_*	SFR [$M_\odot$ yr^{-1}]	sSFR [yr^{-1}]
dwSN	3.0×10^{10}	8.1×10^{8}	5.3×10^{-2}	6.5×10^{-11}
dwALL_1	3.2×10^{10}	1.3×10^{8}	2.6×10^{-2}	2.0×10^{-10}
dwALL_8	2.8×10^{10}	2.1×10^{7}	1.7×10^{-3}	7.9×10^{-11}

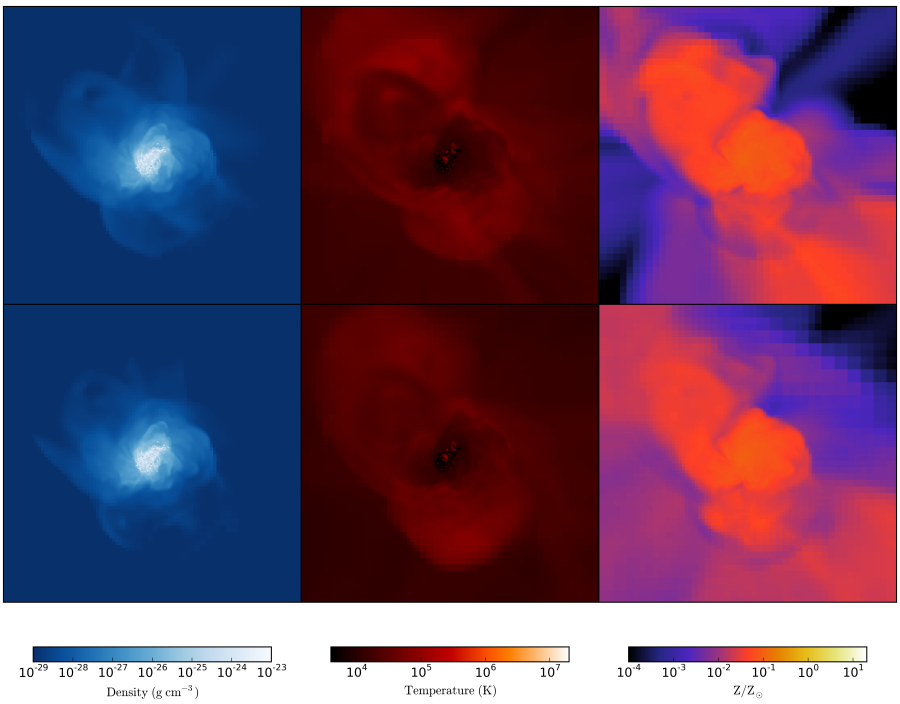

Fig. 3.1.— Images of the dwALL_1 model at $z = 0$. The images are centered on the galaxy and are 4 R_{vir} across. From left to right are the density, temperature, and metallicity of the gas cells. *Top:* A narrow slice through the center of the box. *Bottom:* A projection of all gas cells in the simulation. Even for the this small galaxy the CGM has clear structure and is enriched in metals.

served ions, namely H I Lyβ, Mg II $\lambda\lambda$2796, 2803, C IV $\lambda\lambda$1548, 1550, and O VI $\lambda\lambda$1031, 1037. These ions probe a wide range of ionization conditions. H I and Mg II typically trace the "cool" and dense gas ($T \sim 10^4$ K, $n_H \sim 0.1$ cm^{-3}) while C IV and O VI typically trace the "warm" to "hot", low density gas ($T \sim 10^{5-6}$ K, $n_H \sim 10^{-2} - 10^{-4}$ cm^{-3}). The CGM was examined with 1000 LOS with randomly chosen impact parameters (out to $D = 1.5$ R_{vir}) and randomly chosen position angles. The spectra are generated using the COSFUV ISF for H I, C IV, and O VI and the COSNUV ISF for Mg II with $S/N = 30$.

The `MOCKSPEC` code was used to analyze the simulations using 1000 lines of sight (LOS) with impact parameters ranging from 0 – 1.5 R_{vir} ($R_{vir} \sim 90$ kpc).

The star formation rate of the dwarfs are extremely bursty, especially for dwALL_1 and dwALL_8. The goal was to examine the average properties of the CGM, not the effect of star formation bursts on the CGM. To reduce the effect of the bursts in star formation, we averaged together all snapshots of each run with $z < 0.1$. This results in six snapshots per run, for a total of 6000 LOS per feedback prescription. In this time frame, dwSN experiences no star formation bursts, dwALL_1 experiences one burst, and dwALL_8 experiences two bursts. By averaging over these bursts, our results are indicative of the average global properties of the dwarf's CGM and less influenced on if the galaxy recently experienced a burst in star formation.

3.2.2. Observations

Observations of dwarf galaxies are difficult due to their low luminosity and small mass. Data sets of the CGM of dwarf galaxies are limited to the COS-Dwarfs survey (Bordoloi et al. 2014). This survey was a continuation of the COS-Halos survey (Tumlinson et al. 2013) which mapped out the metal content in the CGM of massive galaxies ($L \sim L^*$). The COS-Dwarfs survey focused on mapping the metal content of dwarf galaxies by observing the C IV $\lambda\lambda 1548, 1550$ in absorption around $L \sim 0.006 - 0.18\,L^*$ galaxies using the *Cosmic Origin Spectrograph* (Green et al. 2012) on *HST*. The wavelength range of the COS FUV gratings limit observations of the C IV doublet to $z < 0.1$.

The study resulted in 43 galaxies with stellar masses ranging from 10^8 – $10^{10.5}$ $M_\odot$ sampled out to impact parameters of 150 kpc. The galaxies were separated into two categories based on their specific star-formation rate, with galaxies with

sSFR $> 10^{-10.5}$ yr^{-1}classified as star-forming galaxies. Of the initial 43 galaxies observed, 34 are classified as star-forming. The sSFR of the simulated galaxies place them in the star-forming category. The simulated galaxies had lower stellar masses than the COS-Dwarfs sample which only contains galaxies with $M_* > 1.58 \times 10^8$ $M_\odot$. The largest simulated dwarf was dwSN with $M_* = 8.2 \times 10^8$ are smaller than the majority of COS-Dwarfs sample as shown in Figure 3.2. The mass of a galaxy has a strong effect on the nature of the CGM so the simulations cannot be fully compared equally to the COS-Dwarfs sample.

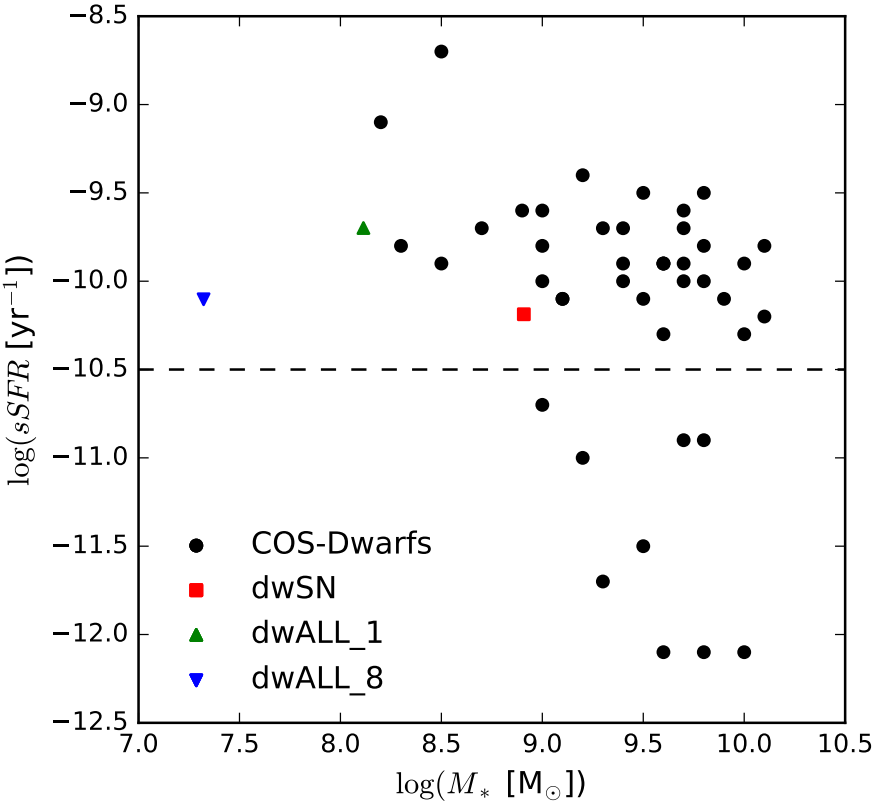

Fig. 3.2.— The stellar mass sSFR relation for the COS-Dwarfs sample and the simulated dwarf galaxies. The horizontal line marks the cutoff between star-forming and quiescent galaxies. The simulated dwarfs were high above the star formation cutoff but were lower in stellar mass than the majority of the COS-Dwarfs sample.

3.2.3. Mockspec Parameters

To match COS-Dwarfs the instrumental ISF used in `MOCKSPEC` was COS FUV with a S/N = 30. The orientation of the galaxies was set to 0° (face-on). However, the galaxies are small and have a bursty star formation history, making establishing a morphology difficult.

This study included HI, MgII, CIV, and OVI. While COS-Dwarfs only published results for CIV, this only selects a single phase of gas. Collisionally ionized carbon resides in the CIV state for gas with T $\sim 10^5$ K (Oppenheimer & Schaye 2013b). The inclusion of OVI is to probe hotter gas, while MgII probes cooler gas. Utilizing a selection of ions with a range of ionization conditions enables detection of a broader sample of the CGM's phase-space.

3.3. Results

3.3.1. Equivalent Width vs. Impact Parameter

To characterize the distribution of metals around the galaxy observers explore the relation between the strength of the absorption feature, characterized by the equivalent width (EW) and impact parameter (D). The detected EW trends with impact parameter are shown in Figure 3.3. For each ion a line is fit to the behavior of $\log(EW)$ vs D such that $\log EW = mD + W_0$. The fit parameter of these lines are shown in Table 3.2. The "coefficient of determination" r^2 was adopted to describe how much of the variance in $\log EW$ was predictable from D, and ranges from 0 (a poor fit) to 1 (a perfect fit).

The HI absorption strength declined in a mostly linear fashion, as evidenced

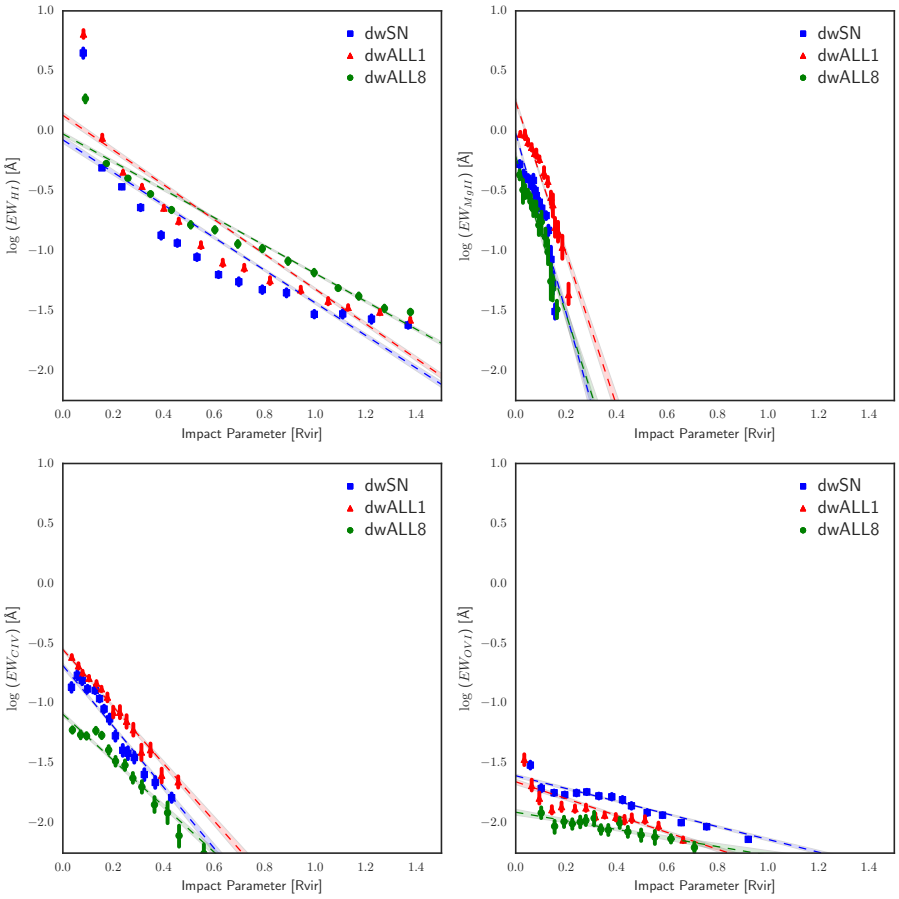

Fig. 3.3.— The binned equivalent width trends with impact parameter for each ion in the three runs. For each ion a line is fitted to the data such that $\log EW = mD + W_0$. *Top Left*: The HI absorption behavior. It can be found at all impact parameters. The decline of EW with increasing impact parameter was mostly linear outside of the smallest impact parameters. *Top Right*: The MgII absorption was constrained to the inner portions of the simulation and dropped off quickly. The decline was more linear than for HI. *Bottom Left*: The CIV behavior. This ion was still linear but declined less quickly than MgII. *Bottom Right*: The OVI absorption was mostly flat with impact parameter.

by the high r^2 values ($r^2 > 0.66$). The largest deviation occurred in the inner regions where $D < 0.1$ R_{vir}. In this region most of the LOS passed through the galaxy itself, which is a large reservoir of hydrogen gas and generates very strong absorption features. The variation between runs was slight. As the strength of radiation feedback increased the mean strength of HI features increased by at

most 0.5 dex.

The Mg II absorption profile dropped off much faster with increasing impact parameter than H I ($\bar{m}$ = -6.81 versus -1.3) and was not found beyond 0.3 R_{vir}. The trend with feedback prescription was different from H I as well. The strongest Mg II absorption was found in dwALL_1 with dwALL_8 and dwSN having very similar profiles.

The C IV absorption profile was shallower ($\bar{m}$ -2.27 versus -6.81) and extended farther out, reaching 0.6 R_{vir}. As with Mg II, the dwALL_1 simulation generated the strongest absorption at all impact parameters and dwALL_8 generated the weakest absorption features, evidence that the C IV CGM was sensitive to the strength of photoheating. Stronger photoheating (dwALL_8) generated weaker C IV absorption than weak photoheating (dwALL_1) or no radiative feedback (dwSN).

The O VI absorption profile was the shallowest with lowest slope ($\bar{m} = -1.72$) and extended for the largest range of the metals, reaching out to 1 R_{vir}, but with the weakest absorption features. The strongest O VI features had an equivalent width of $10^{-1.5} \sim 0.03$ Å. Since typical observations have an equivalent width sensitivity of ∼0.05 Å, most observations would not detect the O VI absorption. Between the three simulations, dwSN produced the strongest O VI absorption and dwALL_8 produced the weakest. Adding radiative feedback weakened the O VI absorption but the effect was slight.

Taken all together, dwALL_8 which utilizes the strongest photoheating feedback, produced the most metal-poor CGM. The dwALL_1 simulation produced the strongest Mg II and C IV, but dwSN produced stronger O VI. However the strength

of these trends was slight as the observed EW for Mg II and C IV depended more on the impact parameter rather than the feedback prescription. The trend between $EW_{O\,VI}$ and impact parameter was weak and thus would be the best ion to observe to differentiate between the feedback prescriptions. This difference was more apparent in the EW distribution, shown in Figure 3.4.

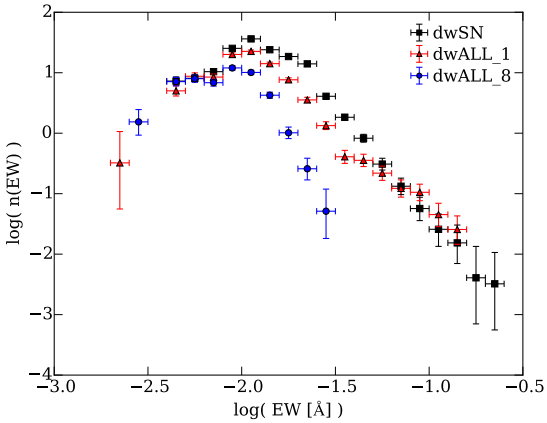

Fig. 3.4.— The equivalent width distribution for O VI around the dwarf galaxies, showing the log frequency each equivalent width is observed around for each run. The dwALL_8 run consistently produced weaker O VI features than the other runs. The dwALL_1 and dwSN runs had comparable O VI distributions. The drop off seen at small EW (EW$< 10^{-2}$ Å) was due to detection sensitivities and not indicative of the true nature of the distribution.

To determine which simulation created the most realistic CGM the EW trend with D was compared to the results of COS-Dwarfs, described in §3.2. The result is shown in Figure 3.5.

The COS-Dwarfs survey only released results for C IV, limiting the ability to compare. The simulation results are shown as contours to eliminate the effect of binning. In general, the simulations under predicted the strength of C IV. The dwALL_1 simulation, shown in red, came closest by matching the weakest

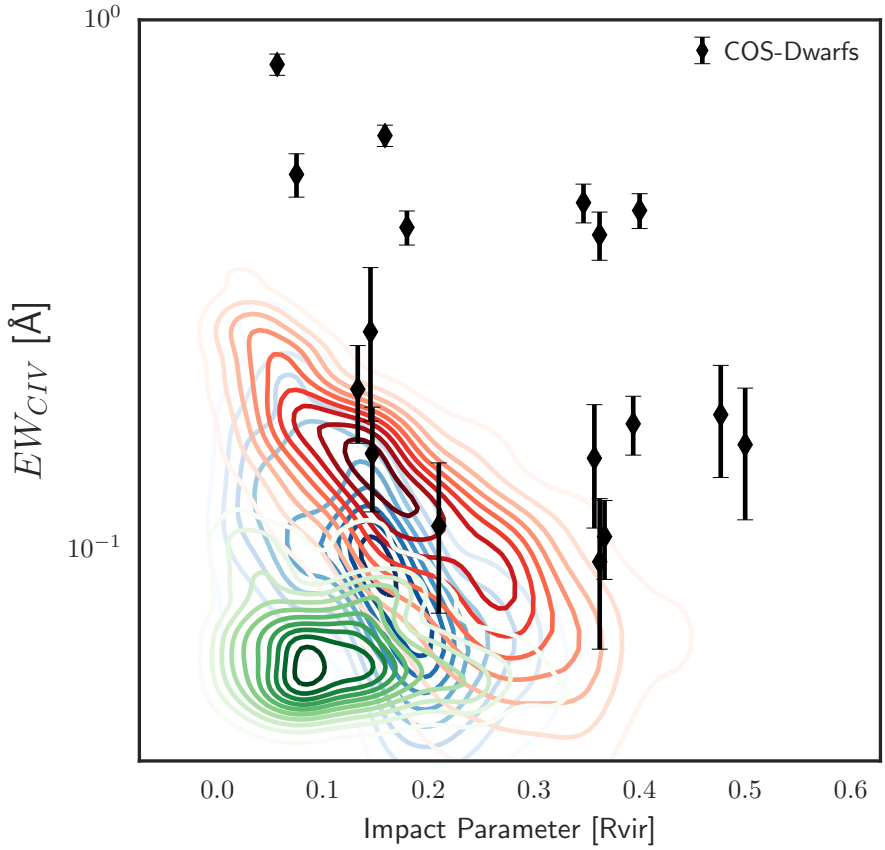

Fig. 3.5.— The comparison of the $\mathrm{EW_{C\,IV}}$ vs D for the three simulations to observations from COS-Dwarfs. The simulation results are shown in contours due to the large number of data points with the colors matching as in Figure 3.3 (dwSN = blue, dwALL_1 = red, dwALL_8 = green). A 0.05 Å cut was applied to the simulation results to match COS-Dwarfs. In general the simulations under predict the strength of C IV absorption. The dwALL_1 is the most realistic CGM as it matches a few observations. The EW distributions for the other ions show no significant difference between the three models and thus are not shown.

observations. None of the simulations could match the strongest C IV observations. The dwALL_8 simulation produced the least realistic CGM as traced by C IV absorption.

3.3.2. Covering Fraction

To quantify the extent of metals in the CGM of the dwarfs, the covering fraction of each ion was calculated. The covering fraction is the ratio of sightlines with detected absorption above a given minimum EW to the total number of sightlines through the halos within a given bin of impact parameter. Figure 3.6 presents the covering fraction for HI, MgII, CIV, and OVI absorption as a function of D and EW detection thresholds. Each column is a different feedback prescription and each row is a different ion. The behavior along the x-axis shows the effect of impact parameter, while the behavior along the y-axis shows the effect of the EW cut. The color shows the covering fraction at a given impact parameter and EW cut.

The results from Fig 3.6 are as follows. HI could found with a $C_f > 50\%$ at all impact parameters with a low enough EW cut (> 0.01 Å). Within 0.3 R_{vir} of the galaxy, HI was found with an EW > 1 Å in 100% of LOS. Once outside of 0.3 R_{vir}, the occurrence of HI drops precipitately, with no LOS having an EW > 1 Å. The details of the feedback prescription did not play a dominant role in the HI covering fraction in the inner halo ($D < 1.0$ R_{vir}). Beyond the virial radius the covering fraction increased for low EW cuts ($EW_{cut} < 0.1$ Å) as the strength of photoheating was increased.

Similarly, the MgII covering fraction did not change significantly with feedback prescriptions. MgII was found with high probabilities ($> 50\%$) close to the galaxy, but was not found at all outside of ~ 0.3 R_{vir}. The resulting covering fraction was very sensitive to the EW cut. At very low impact parameters, the covering fraction could vary drop from 100% to 10% by increasing the EW cut

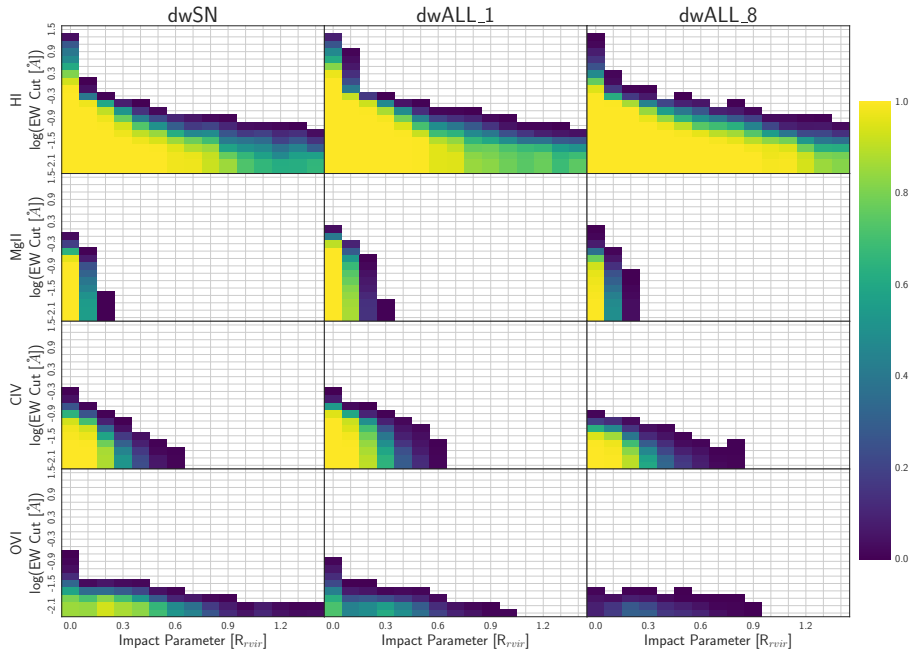

Fig. 3.6.— Covering fraction for each ion and feedback prescription as a function of impact parameter and equivalent width cut. Each column is a different run and each row is a different ion. The color of at each point is the resulting covering fraction at that distance given by the x-axis and using the equivalent width cut given by the y-axis. This explicitly shows how the sensitivity of an observational survey to weak absorption features can mask the true distribution of gas, particularly with HI and OVI. The distribution of MgII was less sensitive to the cut used.

from 0.5Å to 1Å.

The CIV covering fraction was similarly insensitive to the feedback prescriptions. As the strength of photoheating was increased the maximum EW$_{cut}$ allowed that still resulted in detectable CIV absorption decreased. The added feedback resulted in overall weaker CIV absorption. The radial extent of CIV absorbing gas did not change between dwSN and dwALL_1, reaching out to 0.6 R$_{vir}$, but dwALL_8 generated very weak CIV out to 0.9 R$_{vir}$. The outer regions had sparse CIV detections. If the distribution was limited to areas where it was likely to detect CIV (C_f(CIV) $>$ 0.5), the variation between feedback prescriptions disap-

peared. Measurements of C IV absorption could be used to differentiate between the feedback prescriptions but only with a large enough sample to accurately probe the low covering fraction space.

The O VI covering fraction was strongly affected by the details of the feedback. This ion's covering fraction within 0.5 R_{vir} of the galaxy varied from ∼80% in dwSN to to ∼50% in dwALL_1 to ∼30% in dwALL_8. The effect of the EW cut was not greatly altered by the feedback prescription as O VI was undetectable outside of 0.1 R_{vir} with an EW cut >0.03 Å. The drop in covering fraction with radiation feedback strength was also seen in the equivalent width distribution (Figure 3.4) and the EW spatial profile (Figure 3.3). This explicitly shows how in the dwALL_8, the simulations failed to produce strong O VI absorption. The dwSN and dwALL_1 runs were able to produce O VI profiles with an order of magnitude higher equivalent widths than dwALL_8.

The C IV covering fraction was compared the observed results from COS-Dwarfs in Figure 3.7. Here a 0.1 Å EW cut was applied to the `MOCKSPEC` results and the COS-Dwarfs impact parameter binning was used. In general, the simulations did a poor job matching observations. The only success occurred in the inner bin in the dwALL_1 run. The dwSN and dwALL_8 runs failed to match the C IV observations at all impact parameters. Beyond the inner bin, dwALL_1 also failed to match observations. In the outer bin, with $D > 0.5$ R_{vir}, all models agreed with observations by not detecting any C IV.

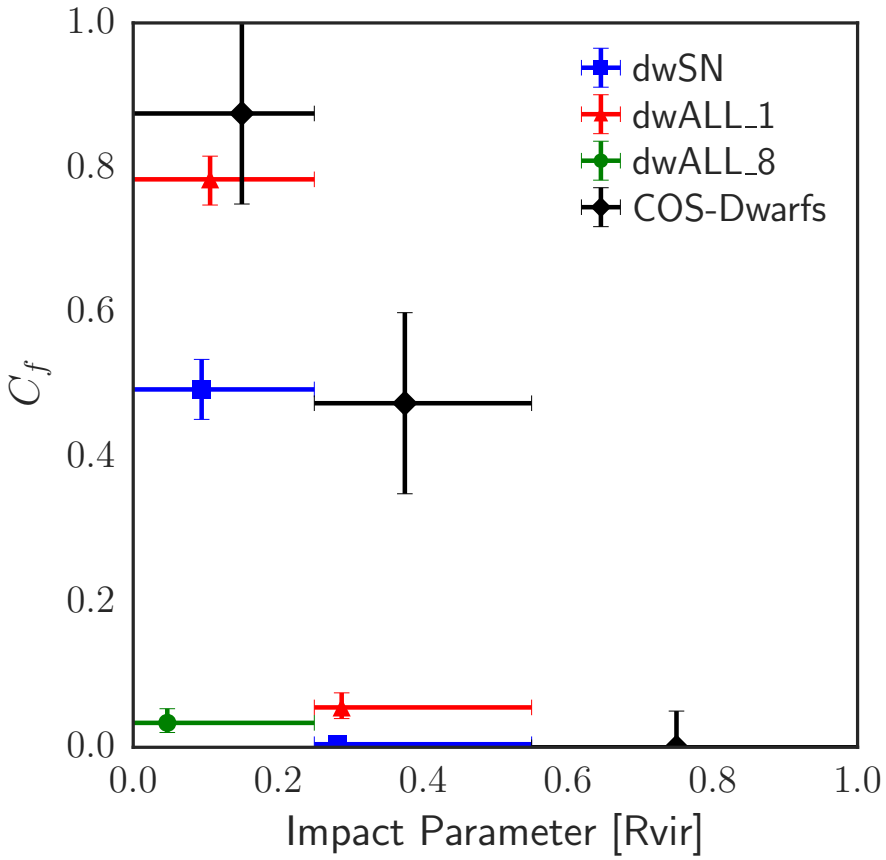

Fig. 3.7.— The covering fraction of CIV compared to the CIV covering fraction observed around star-forming galaxies. An EW cut of 0.1 Å had been applied to the simulation results to match the COS-Dwarfs methods. The dwSN model agreed with the observed results in the inner regions of the CGM, but failed beyond 0.3 R_{vir}. The dwALL_1 and dwALL_8 models failed to match the observations at all impact parameters. This failure was due to the EW cut, as dwALL_1 and dwALL_8 generated significant CIV absorption with EW < 0.1 Å as shown in Figure 3.3 and Figure 3.6.

3.3.3. Phase

To describe the physical state of the gas that give rise to absorption the phase of the gas is shown in Figure 3.8. All cells that gave rise to significant absorption were placed in the density-temperature plane with the color denoting the total mass of the ion at the given density and temperature.

While the phase diagram encompasses all LOS at all impact parameters, it could be divided into two regimes. The cells at high density and low temperatures ($\log(n_H) > -1$ and $\log(T) < 4$) were primarily within 0.1 R_{vir} of the galaxy. This region was classified as the ISM tail. The rest of the phase diagram was dominated by the CGM.

Gas cells that generated HI absorption could be found at all phases, however detectable HI preferred to reside in the ISM tail and in a thin region at T $\sim 10^4$ K. There was little density dependence for the absorbers, with cells found from $n_H = 10^{-8} - 10^1$ cm^{-3}. Very little gas with T $> 10^5$ K generated HI absorption as hydrogen above this temperature would likely be ionized into HII.

There was little change in these trends across the various feedback prescriptions used. This implied the nature of HI around galaxies was relatively immune to the star-formation and outflow activity of the galaxy. Star formation was mostly concerned with the consumption of HI, not the production of it so it is not surprising that the details of star formation do not have a strong affect on the HI absorption. Outflows are predicted to be hot with T $> 10^5$ K which was not a phase that produces strong HI, so it was also not surprising that the details of stellar feedback did not strongly influence the HI CGM. The outflows could move the cool HI but the results presented here suggested any interaction did not strongly affect the phase of HI absorbing cells.

Contrary to HI there was a strong phase selection when MgII absorbing cells are examined, shown in the second row of Figure 3.8. In general MgII only arose in dense, cool gas. Very little gas with T $> 10^4$ K and with $n_H < 10^{-4}$ cm^{-3}contributed to MgII absorption. The majority of the mass of MgII around

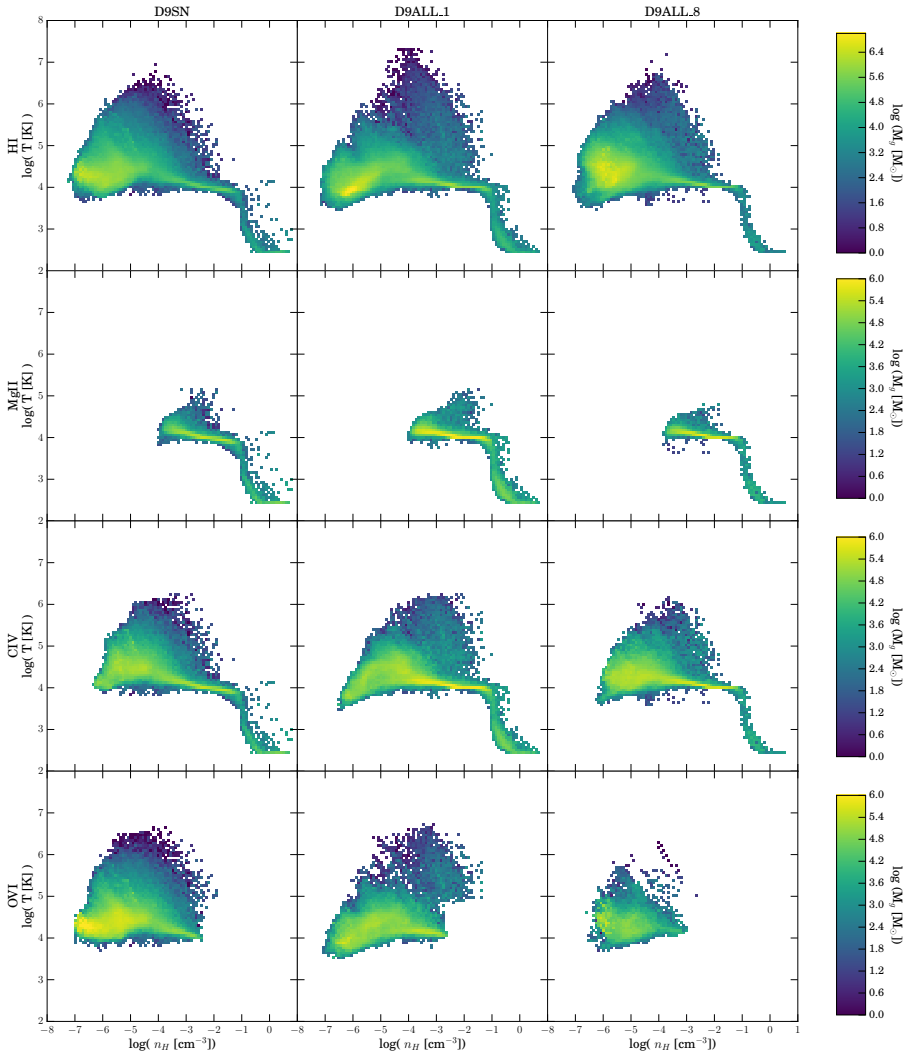

Fig. 3.8.— The phase off all cells that contribute significantly to absorption as determined by `SIGCELLS`. The color corresponds to the total mass in each phase bin. Each row is a different ion and each column is a different run. The HI gas could be found at most phases, with the most mass located in the cool, diffuse regions ($T \approx 10^4$K, $n_H \approx 10^{-6}$). The metals were restricted to a smaller phase space then HI. The MgII gas was primarily found in the cool, dense gas, particularly the ISM tail. The CIV gas was found at lower densities and higher temperatures than MgII, and OVI peaked at still more diffuse and hotter gas. There was no significant difference between the feedback prescriptions for the all ions except OVI. Increasing the strength of radiative feedback decreased the total amount of OVI found, especially in very hot gas (T$> 10^{5.5}$K).

the galaxies resided at T $\sim 10^4$ K and $n_H \sim 10^{-3}$ – 10^{-1} cm^{-3}. The ISM tail was also a strong contributer of MgII gas.

As a product of star formation it was expected that MgII would be affected by the changing physics of the different runs. A small variation between the three runs was found. As the strength of photoheating was increased the amount of MgII found in the ISM tail relative to the total amount of MgII decreased. In dwALL_8 cell contributing to MgII absorption were almost exclusively outside of the ISM tail. A possible explanation for this is the stronger outflows in the dwALL_8 run pushed ISM MgII gas into the CGM.

For HI and MgII, the derived absorbing cell phase was in agreement with the phase distributions of HI and MgII absorbing gas found for $D = 100$ kpc from Ford et al. (2013), albeit for larger galaxies ($M_{vir} \approx 10^{11-12}$ $M_\odot$). The similarity was a consequence of the low impact parameters. The inner regions of DM halos were similar regardless of the total size of the halo. This self-similarity of halos has been observed for low ions (Churchill et al. 2013).

Gas giving rise to CIV was expected to be hotter than MgII gas due to the higher ionization potential than MgII (64.5 eV versus 15.0 eV) and so was expected to reside at higher temperatures where it could be more easily collisionally ionized. In collisional ionization equilibrium (CIE) carbon will prefer the CIV state for temperatures of T $\sim 10^5$ K (Oppenheimer & Schaye 2013b). At this temperature there was a peak of gas in the phase diagrams across a wide range of densities corresponding to the collisionally ionized CIV. However it was a small component of the absorbing CIV gas. Most of the gas lied at T $\sim 10^4$ K with peaks at $n_H \approx 10^{-4}$ – 10^{-3} cm^{-3}suggesting the gas was dominated by photoionization. A small

fraction of the overall distribution resided in the ISM tail.

Like Mg II, the phase of absorbing C IV varied across the different runs. Most notably the collisionally ionized C IV decreased as the strength of photoheating increased. The photoionized cloud of C IV remained mostly unaffected by the changing feedback models.

The phase distribution of C IV was compared to the distribution found by Ford et al. (2013) and found to be similar. The differences, however, were larger than for the Mg II phase distributions. The phases derived by `MOCKSPEC` peaked at a lower density than that found by Ford et al. (2013) by a full dex for similar impact parameters. This suggests the self-similarity of the CGM does not hold for high-ionization ions.

With the highest ionization potential of the ions we evaluated, O VI gas in CIE should reside at the highest temperatures of T $\approx 10^{5.5}$ K. In the bottom row of Figure 3.8 some of the O VI absorbing gas occupied a small, well-defined region of phase space consistent with that of collisionally ionized gas (T $\approx 10^{5.5}$ K, n_H $\approx 10^{-5}$ – 10^{-3} cm^{-3}). However, like with C IV, the collisionally ionized gas was a small fraction of the total absorbing gas. Most of the O VI gas resided at lower temperatures and lower densities, suggesting it was primarily photoionized. A notable exception for O VI compared to the other ions is the lack of an ISM tail. Gas dense and cool enough to reside in the ISM tail was unable to produce high ionization species.

3.3.4. Common Absorbers

Table 3.3 contains the global likelihood of a cell contributing to the detection of two different ions derived from all snapshots of all feedback prescriptions. The phase diagrams discussed above did not have strong variations between the runs, which matches expectations. Changing the stellar feedback prescriptions altered how the stars impact their local environment, which had consequences for the distribution of gas in the CGM. However once the gas was in the CGM changing the feedback prescriptions should not affect the ionization state of gas in the CGM, especially since stellar radiation fields are not considered. Thus a gas cell in dwSN that contributed significantly to CIV and OVI absorption should have similar properties to a CIV and OVI cell in dwALL_1 and dwALL_8.

In Table 3.3 are the percent chances of finding a certain ion in a cell given that it contributes to a different ion's absorption. For example, given that a cell contributed to a CIV absorption feature there was a 23.0% chance that the cell also contributed to a MgII feature. The diagonal of the table give the fraction of all cell probed by a LOS that generated absorption features, meaning all cells probed only 5.6% of them generated MgII absorption.

The first conclusion from Table 3.3 was selecting by HI was not a useful criterion. If a LOS has metal absorption there will be associated HI absorption in the same gas.

The relation between MgII and CIV was interesting. Approximately one quarter of CIV cells gave rise to MgII but roughly all MgII cells also give rise to CIV. The MgII cells were a subset of the CIV cells, which was supported in Figure 3.8. The part of the phase diagram covered by MgII was also covered by CIV, but

Table 3.2. Fit Parameters for EW vs D

Ion	Run	Slope	W_0	r^2
HI	dwSN	-1.36	-0.08	0.66
	dwALL_1	-1.45	0.13	0.73
	dwALL_8	-1.16	-0.03	0.78
MgII	dwSN	-7.51	-0.02	0.72
	dwALL_1	-6.34	0.24	0.72
	dwALL_8	-6.59	-0.22	0.61
CIV	dwSN	-2.54	-0.69	0.70
	dwALL_1	-2.39	-0.55	0.68
	dwALL_8	-1.92	-1.09	0.68
OVI	dwSN	-0.53	-1.60	0.47
	dwALL_1	-0.70	-1.65	0.37
	dwALL_8	-0.36	-1.91	0.19

Table 3.3. Probabilities of a cell being a common absorber.

Given	Finding			
	HI	MgII	CIV	OVI
HI	83.4	6.7	29.2	26.2
MgII	99.3	5.6	99.8	17.0
CIV	99.7	23.0	24.4	44.9
OVI	99.3	4.3	49.7	22.0

CIV also arose in hotter and more diffuse gas.

As expected from the phase diagram there was very little overlap between the MgII and OVI. The overlap was four times larger if the sample was selected for MgII, but it still remained under 20%. The disparity between the common fraction depending on the ion selection used fell from the area each ion took up on the phase diagram. MgII was restricted to a very narrow region, so gas cells that lied in this part of the diagram are very likely to generate MgII absorption due to the high density of MgII absorbing cells here. In contrast, OVI took up a very large area of the phase diagram and there was a small area where they overlap. The overlap area was a larger fraction of the MgII area than the OVI area so selecting for MgII absorption would naturally lead to a larger incidence rate of common absorption than selecting for OVI.

The last pair, CIV and OVI, showed similar behavior as suggested by their large overlap on the phase diagram. When selecting by either ion, there was a roughly 50% chance of detecting the other one. This was in rough agreement with studies of the cosmic density of metal absorption that find the incidence rates of CIV and OVI are roughly equal (Rahmati et al. 2016).

The fraction of cells with common absorbers had implications for observational plans. Suppose the goal of an observational survey were to observe OVI around dwarf galaxies. It would be a poor choice to selects galaxies with MgII absorption as only 17% of the systems would also have significant OVI absorption. The best plan would be to select systems that have CIV absorption detected, but this would still only yield OVI absorption $\sim$50% of the time.

3.4. Discussion

The goals of this study were to (1) examine the effects of varying stellar feedback models had on the absorption properties of the CGM, (2) compare statistics of mock absorption lines to observations, and (3) to examine the how gas properties differed from the observational analysis methods to the properties of the gas that actually gave rise to the absorption.

Three different feedback methods were implemented in separate simulations of the same DM halo. The first, dwSN, included only SNe and stellar winds as possible stellar feedback methods. The second, dwALL_1, added radiative pressure and weak photoheating to the feedback methods of dwSN. The last, dwALL_8, used the same models as dwALL_1 but with stronger photoheating. Using `MOCKSPEC` the CGM of each simulation was observed with synthetic QAL and compared to the COS-Dwarfs sample.

3.4.1. Effect of Feedback

A primary goal of this study was to determine to effect varying stellar feedback prescriptions have on the absorption line properties and the gas phase distribution of the CGM of dwarf galaxies. The results shown in §3.3 argue that the effect is slight. The EW distribution, trends with impact parameter, covering fraction, and absorber phase for HI, MgII, and CIV did not vary significantly with changing feedback prescription. The lack in variation in the absorption and phase properties was a sharp contrast to the strong effect the various feedback prescriptions had on the galaxy itself such as the factor of 40 difference between the stellar masses.

The exception was OVI absorbing gas. Increasing the strength of radiation feedback in the form of radiation pressure and photoheating decreased the amount of OVI observed as seen in the decreased number of strong OVI absorption features detected, the lower OVI covering fraction, and the decreased amount of collisionally ionized OVI absorbing cells in dwALL_8 as compared to dwALL_1 and dwSN.

The similarity between dwALL_1 and dwSN suggested the nature of the CGM was not sensitive to the inclusion of radiation pressure feedback. The difference between dwALL_1 and dwALL_8 suggested the hot CGM was sensitive to the strength of photoheating feedback.

A possible explanation could be derived by examining the recycling time of galactic winds as traced by the various ions. Since ART is an AMR code, the wind recycling time is very difficult to measure from the simulations. However, Ford et al. (2014) used a modified version of Gadget-2, an SPH code, to measure this recycling time around Milky Way mass galaxies. They determined that HI traced ambient gas that was not participating in winds, MgII traces the galactic fountain, CIV traces recycled accretion at low impact parameters and traces ancient outflows at high impact parameters, and OVI traces ancient outflows. Ancient outflows are defined as winds originating more than 1 Gyr ago. While a direct comparison between the higher-mass simulations and dwarf simulations is not ideal, there are no comparable studies of recycling time using low-mass galaxies.

The OVI was strongest in the dwSN model and weakest in the dwALL_8 model. As discussed in Trujillo-Gomez et al. (2015), the increased radiation feedback in dwALL_8 impeded star formation significantly. The lowered star forma-

tion rate lead to fewer outflow events, lowering the amount of energy in the CGM. The decreased thermal energy decreases the amount of oxygen in the collisionally created O VI state, leaving only the photoionized O VI. This had the effect of decreasing the mean equivalent width of the observed O VI. The non-thermal feedback from radiation effects decreased the strength absorption due to collisionally ionized high-ionized species.

The low- and mid-ionization species, traced by Mg II and C IV were strongest in the dwALL_1 model. This suggested that radiation feedback was capable of generating outflows, albeit cooler ones than the dwSN model due to the earlier onset of radiation feedback. The dwALL_8 model's feedback was too strong and strongly reduced the number of stars created, which in turn decreases the ability of the stars to push metals into the CGM.

The uniformity of the CGM between the three runs had implications for the role both virial mass and stellar mass play in the nature of the CGM. Between the three models, the virial mass remained the same while the stellar mass varied by two orders of magnitude. This suggested the stellar mass did not have a strong effect on the nature of the CGM. The virial mass was more important to the structure of the CGM, in agreement with studies of larger galaxies (Churchill et al. 2013).

The O VI phase diagrams showed the largest difference across the three runs. Similar to C IV the size of the collisionally ionized gas in the CGM decreased as the strength of photoheating was increased. In dwALL_8 region of the phase diagram corresponding to collisionally ionized O VI was not populated.

There are several possible reasons for why the amount of collisionally ionized

gas decreased as the strength of photoheating increases. One scenario is the addition of radiation feedback models produced a cooler CGM, resulting in a reduction in the amount of gas available for ionization in the collisionally ionized portion of the phase diagram. The cooler CGM could be a consequence of the way feedback is modeled in the simulations. Radiation pressure was modeled as a non-thermal momentum added to the gas and photoheating was modeled as a pressure. Neither of these feedback sources heated the gas but did move gas away from the stars generating them. The combination would result in cooler winds and possibly a cooler CGM.

A second scenario was a lack of oxygen atoms in the CGM. As the strength of photoheating increased the radiation and photoheating effects disrupted the star formation sooner by removing gas from the area around stars. This reduced the amount of material available for the SNe to push out of the galaxy. If SNe were the dominant method for moving material into the CGM, reducing the amount of gas around the stars when the SNe occur would reduce the resulting amount of metals in the CGM. However it is unclear how this would preferentially reduce the amount of oxygen in the CGM while leaving the MgII and CIV abundances unchanged.

3.4.2. Comparison to Observations

The goal of comparing the simulated CGM to observations was made difficult due to the difficulty of observing the CGM of dwarf galaxies. The comparison was limited to the COS-Dwarfs sample. An unfortunate consequence of the zoom-in simulation technique is the output galaxies were selected by their virial mass, not

their stellar mass. Observationally, it is much easier to control for stellar mass as it can be directly observed. Inferring the virial mass from the stellar mass requires techniques such as abundance matching (Trujillo-Gomez et al. 2011). The stellar mass in simulations is a consequence of the physics included in the simulation.

The simulated galaxies used in this chapter had smaller stellar masses than the galaxies studied in the COS-Dwarfs survey. As discussed in §3.3.1, 3.3.2 the simulated CIV was weaker than observed by COS-Dwarfs. The simulated CIV CGM extended for the same distance as observed in that there was no detected CIV beyond 0.5 R_{vir}. However the detected CIV in the simulations within 0.5 R_{vir} had smaller EW than what is observed.

A result of COS-Dwarfs was a weak correlation between stellar mass and EW(CIV) where larger galaxies gave rise to stronger CIV absorption. This is intuitive as larger galaxies have generated more stars which in turn generates more metals in the CGM. Adding metals to the CGM is one method to strengthen an absorption feature. If this correlation holds for smaller galaxies than COS-Dwarfs observed then the simulated galaxies would be expected to have weaker CIV features. To truly verify the results of the simulations observations of small dwarf galaxies must be made or larger galaxies need to be simulated

3.4.3. Connection between Observations and True Properties

A common tool used by observers to determine the physical properties of the gas is to fit a Voigt profile to the absorption (Boksenberg et al. 1979; Churchill et al. 2003; Simcoe et al. 2006; Mathes et al. 2014) in a process called Voigt profile (VP) decomposition. This technique allows observers to infer the absorber's

temperature and kinematic structure.

VP decomposition has several implicit assumptions. The base assumption is the absorption arises from a single physical structure that is spatial coherent, referred to as "clouds". Each cloud is also assumed to be kinematically uniform and isothermal, required so each structure can be assigned a velocity and a temperature.

The validity of these assumptions is nearly impossible to check observationally. If the same structure could be observed in emission, the combination of the data sets could give a limit on the physical size of the structure to test the spatially coherent assumption. However structures that are both observable in emission and absorption are very rare.

A strength of the `MOCKSPEC` code is its ability to determine which gas cells are actually generating the absorption profile (see §2.5.6). To test the assumptions of VP fitting a sample LOS was selected that contained absorption for all ions tested, HI, MgII, SiII, CII, CIII, CIV, and OVI. This LOS probed dwALL_8 at $z = 0$ with an impact parameter of 11 kpc (~ 0.2 R_{vir}). The spectra for HI, MgII, CIV, and OVI are shown in the top row of Figure 3.9.

For each synthetic spectrum generated by `MOCKSPEC` for this LOS a VP decomposition was applied. This procedure determined the column densities N, Doppler b parameters (derived from the fitted temperatures of each component using $b = \sqrt{2kT/m_x}$ where m_x is the mass of ion x), and observed redshift z for each VP component using the `Autovp` code. The original version of `Autovp` developed by Davé et al. (1997) was updated to include convolution with an ISF.

Automating VP decomposition is a difficult task made worse by the highly

varying kinematic structures between the gas phases. To fit the spectra generated by `MOCKSPEC` the lines were split in to a low-ionization category, consisting of HI, MgII, SiII, and CII, and a high-ionization category, consisting of CIII, CIV and OVI. Within each category the spectra were fit together, applying the assumption that low-ionization transitions trace the same structures and high-ionization transitions trace the same structures without any assumption that the two categories trace the same structures.

The results of `Autovp` that generated the largest number of kinematically distinct structures were selected. To determine the final results the output of `Autovp` was run through the `Minfit` code (Churchill 1997; Churchill & Vogt 2001). For a complete description of `Minfit`, see Evans (2011). The final model selected contained the fewest VP components that were statistically significant at the 97% confidence level by applying an F-test on the χ^2 distribution. The results of the fitting were shown in Table 3.4.

The summary of the results for this study is shown in Figure 3.9. The top row plots the spectra for HI, MgII, CIV, and OVI.

The second row shows the column density of all gas cells identified as significant by `SIGCELLS` in black points. The colored lines is a histogram of these cells. The colored circles identify the column density of the VP components. The column densities of the fits for HI are in good agreement with the actual column density. However, the VP column densities drastically over predicted the actual column densities of the gas for all metal transitions. The over prediction for MgII was due to the intrinsic absorption profiles of the gas being unresolved by the instrument (Savage & Sembach 1991). This is a well-studied phenomenon

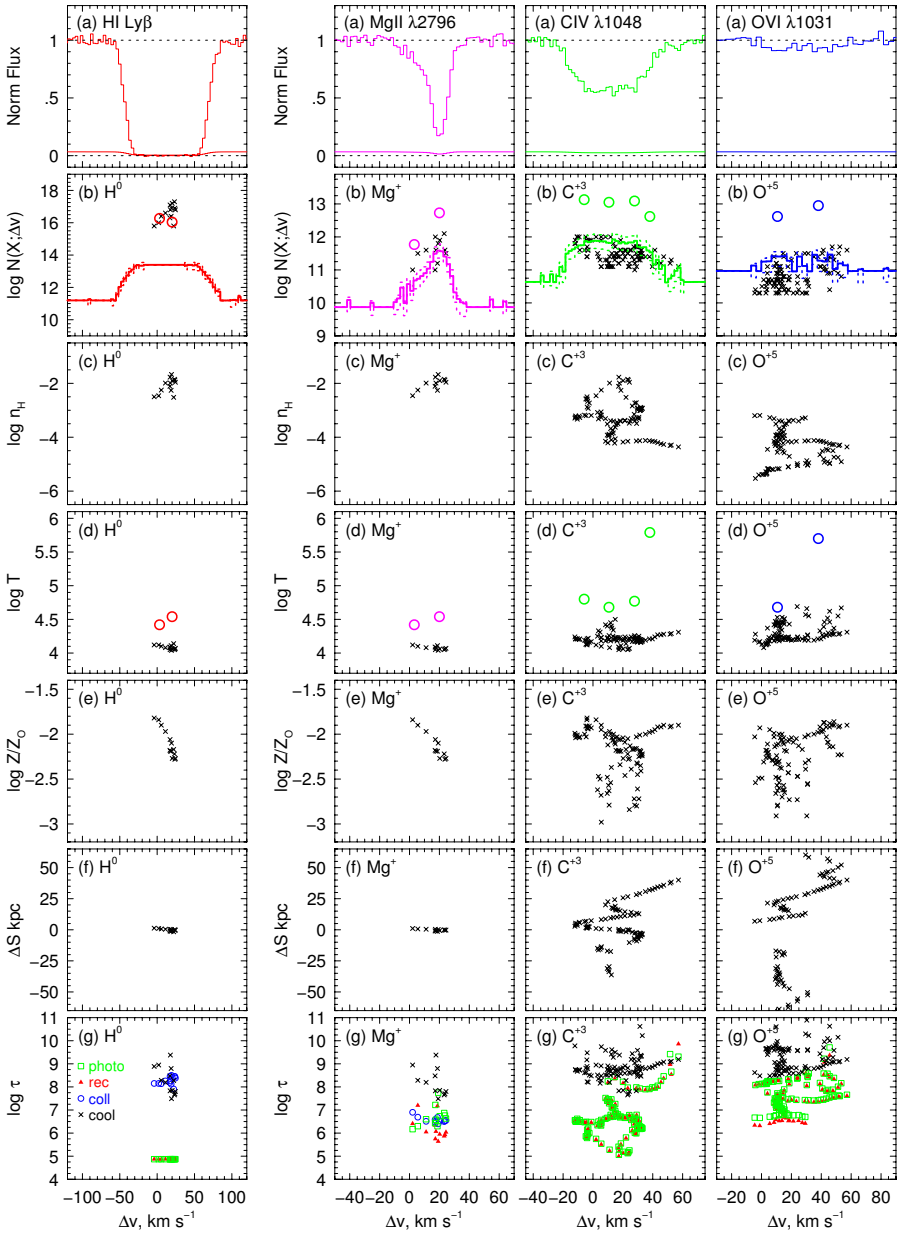

Fig. 3.9.— Comparison of the properties of the gas cells responsible for the detected absorption features and the properties derived by VP decomposition. See text for full description. Adapted from Churchill et al. (2015).

with correction measures developed Jenkins (1996). The ∼1.5 dex discrepancies for CIV and OVI were more interesting and were the first indications that VP

decomposition struggles with high-ionization ions.

The third row shows n_H as a function of Δv for the significant cells. Gas cells that contributed to HI absorption were clustered around $n_H \sim 10^{-2}$ cm^{-3} and $\Delta v \sim$ -10 – 30 km s^{-1}. The gas cells that contributed to MgII were clustered around similar densities and a slightly larger Δv range. The tight clustering around similar densities suggested a single structure, in agreement with the assumptions of VP decomposition.

The gas cells that contributed to CIV and OVI were spread over a large density range. The CIV contributing cells could be found at densities ranging from 10^{-4} to 10^{-2}, while OVI contributing cells could be found at densities ranging from 10^{-6} to 10^{-3} cm^{-3}. The Δv range was similarly large, stretching over 60 km s^{-1}. The large range of densities suggested the cells generate high-ionization absorption do not reside in a single structure, violating an assumption of VP decomposition.

The forth row shows the temperature of the significant cells as a function of Δv. The fitted temperature from the VP decomposition is shown in colored circles for each ion. The low-ionization species all arose from cool gas residing at 10^4 K. The fitted temperature for these species over predicted the actual temperatures by $\sim$0.5 dex. This was similar to the discrepancies for the MgII fitted column density.

The derived temperatures for the high-ionization species again over predicted the actual temperatures of the gas cells. Most of the absorbing gas resided in cool gas with $T \sim 10^4$ – $10^{4.5}$. However the VP decomposition predicted the gas to reside at $10^{4.5}$ – $10^{5.7}$ K. The low temperature fits would suggest the gas to be primarily collisionally ionized, however the actual temperatures would suggest

the gas to be primarily photoionized. This highlights of the possible pitfalls of applying VP decomposition to high-ionization ions.

The fifth row shows the metallicity of the significant cells relative to solar as a function of Δv. Both H I and Mg II show a significant metallicity trend as the absorbing cells moved to higher Δv. Since $\Delta v = 0$ corresponded to the velocity of the galaxy, moving to higher velocities suggested moving away from the galaxy (supported by the next row). This suggested a steep metallicity gradient as the distance from the galaxy increased.

There was no trend between metallicity and Δv with the high-ionization ions. This also supported the model that C IV and O VI did not arise in cloud-like structures.

The sixth row shows the distance along the LOS (ΔS) the significant cells are located as a function of Δv. This quantity demonstrated the spatial extent of the structures generating the absorption. In the low-ionization ions there is virtually no spread in ΔS, strongly supporting the model that gas generating H I and Mg II are cloud-like structures.

The spread in ΔS for high-ionization ions was very different. There was a large spread in the location of the cells along the LOS ($\sim$75 kpc for C IV, $\sim$150 kpc for O VI). The high-ionization absorption was derived from gas cells throughout the entire box which clearly violated the VP decomposition assumption of arising from a single structure. The large spread in O VI locations agrees with the observations of Muzahid (2014).

Examining the relation between ΔS and Δv reveals the source of the velocities of each VP component. The VP components reside at velocities were a large

number of gas cells happen to reside, regardless of the physical location. This suggest the existence of the absorption feature is due to a coincidence of velocity alignment of gas cells, not due to an actual structure. It also strengthened the concept that low-ionization ions and high-ionization ions trace difference phases of the CGM.

The bottom row shows the various timescales of the significant cells as a function of Δv. The photoionization timescales are shown in green, the recombination timescales are in red, the collisional timescales are in blue, and the cooling timescales are in black. These timescales were used to evaluate the assumption of ionization equilibrium. For gas to be ionization equilibrium the gas must be thermally stable while ionization and recombination effects work to achieve a steady-state balance, which requires $\tau_{eq} \ll \tau_{cool}$ here τ_{eq} is the timescales over which equilibrium occurs and τ_{cool} is the cooling timescale calculated by

$$\tau_{cool} = \frac{Q}{|dQ/dt|} = \frac{Q}{|\Lambda_{net}|} = \frac{\frac{3}{2}(n_e + n_N)kT}{|\Lambda_{heat} - \Lambda_{cool}|}.$$

Here, Q is the total heat energy of the gas, n_e is the electron number density, n_N is the nuclear number density, Λ_{heat} is the heating rate per volume, and Λ_{cool} is the cooling rate per volume. The cooling rates were determined using the cooling functions of Wiersma et al. (2009). The heating and cooling rates depend on the ionizing spectra, gas density, gas temperature, and abundance of metals. The ionizing rate can be different for each ion so the ionizing equilibrium assumption must be checked for all ions. The methods for calculating the photoionization, recombination, and collisional timescales can be found in Churchill et al. (2014).

The H I gas was clearly in ionization equilibrium. The photoionization timescales

were shorter than the collisional ionization timescale by three order of magnitude, indicating the HI gas was primarily photoionized. The cooling timescale was comparable to the collisional ionization timescale, which was longer than the dominant ionization timescale. Thus the HI gas was in ionization equilibrium.

The MgII gas was also in ionization equilibrium, as the cooling timescales were longer than the other timescales. Unlike the HI the MgII cells were not dominated by any particular ionization method as $\tau_{photo} \sim \tau_{coll}$.

The gas giving rise to CIV and OVI showed the same behavior. The gas was in photoionization equilibrium as $\tau_{photo} \sim \tau_{rec}$. The collisional ionization equilibrium was greater than 10^{11} years and thus were not shown on the plots. Thus the gas was strongly dominated by photoionization, as suggested by the phase diagram shown in Figure 3.8. The cooling timescales were generally longer than the photoionization timescales, validating the ionization equilibrium assumption.

The assumption of ionization equilibrium was valid for all ions. The HI, CIV, and OVI gas were dominated by photoionization, while the MgII gas was dominated by both photoionization and collisional ionization. The methods used to calculate these timescales did not require additional information other than what can be determined by the VP decomposition. However, as found above, applying VP decomposition to high-ionization ions can lead to inaccurate results and can thus give incorrect timescales estimations.

3.5. Conclusions

In this chapter the CGM of a dwarf galaxy was observed with `MOCKSPEC`. The galaxy was simulated with three different stellar feedback prescriptions

The canonical sample, designated dwSN, utilized only SNe and stellar winds. The other simulations add radiation pressure and photoheating to the stellar feedback models. The dwALL_1 simulation implemented a weaker version of photoheating than then dwALL_8 simulation. The varying feedback prescriptions resulted in significantly different galaxies by $z = 0$. The common observer quantities of covering fraction and EW behavior with impact parameter were presented and compared to observations. Using the results of `MOCKSPEC` that identified the gas cells that contributed significantly to each absorption feature detected, the connection between gas cells and detected absorption was examined. The phase distribution of gas cells was explored, leading to insights on ionization mechanisms for each ion. The nature of cells that contributed to multiple ion absorption features was explored, and the validity of VP decomposition was tested. The conclusions are summarized below.

1. All feedback models tested were able to create a strong, metal-rich CGM. Regardless of the ionization potential of the ion used, the dwarf galaxies produced enough to generate detectable absorption in the CGM.

2. While the changing feedback models resulted in significant differences in the final galaxy they had little effect on the CGM. The trends of both EW and covering fraction with impact parameter do not vary strongly with changing feedback methods. Thus CGM analysis is not a useful metric for testing the validity of the stellar feedback models tested.

3. The CGM between each model was very similar while the stellar mass of the galaxy varies by two orders of magnitude. The nature of the CGM was thus determined more by the virial mass of the halo rather than the stellar

mass of the galaxy.

4. In the study of small galaxies, selecting by stellar mass was not a viable way to study the relations between the CGM and the galaxy. A better approach is to select galaxies by their virial mass.

5. There was significant discrepancy between the behavior of CIV in the simulation and the observational results of COS-Dwarfs. The simulated EW and covering fraction were too low for agreement with observations. However this could be a result of the lower mass of the simulated galaxies compared to the COS-Dwarfs sample. Observations of smaller dwarf galaxies are required for a more conclusive result or simulations of higher stellar mass galaxies.

6. Gas cells contributing to MgII absorption were typically cool and dense, compared with the hot and diffuse nature of OVI absorbing cells. The CIV absorbing cells bridged the gap between the MgII and OVI phase distributions. The HI absorbing cells could be found at all phase locations.

7. To examine the largest range of the CGM's phase space observations should target CIV as the phase space traced by MgII was also traced by CIV. The phase space traced by OVI shares significant overlap with CIV as well.

8. VP decomposition was valid and worked well for low-ionization species such as HI and MgII. It did not work well with high-ionization species such as CIV and OVI since the absorption features of these ions did not arise from a single coherent and isothermal structure. Instead the CIV and OVI absorption features were the result of overlaps in the velocity fields of all gas

cells along the entire length of the LOS.

9. The assumption of ionization equilibrium in the CGM of dwarf galaxies was valid. Most of the CGM was dominated by photoionization, with the exception of MgII gas which was not dominated by any single ionization method.

.

From this work we concluded that dwarf galaxies host a metal-rich CGM that was insensitive to the details of star formation and stellar feedback. While there are presently no observations of galaxies as small as the ones simulated, the simulated CGM was not consistent with observations of the CGM around larger galaxies. The conclusions presented here are particular to the simulations used. To verify the ubiquity of the conclusions more and larger galaxies must be tested.

Table 3.4. VP Decomposition

Ion	Δv [km s^{-1}]	$\log N$ [cm^{-2}]	b [km s^{-1}]	$\log T$ [K]
H I	3.20	16.27 ± 0.15	20.80 ± 0.85	4.42 ± 0.04
	20.01	16.04 ± 0.06	23.92 ± 0.46	4.54 ± 0.02
Mg II	3.20	11.77 ± 0.03	4.24 ± 0.17	4.42 ± 0.03
$\lambda\lambda 2796, 2803$	20.01	12.73 ± 0.01	4.87 ± 0.09	4.54 ± 0.02
Si II	3.20	11.72 ± 0.07	3.94 ± 0.16	4.42 ± 0.04
$\lambda 1260$	20.01	12.10 ± 0.04	4.53 ± 0.09	4.54 ± 0.02
C II	3.20	13.31 ± 0.02	6.03 ± 0.25	4.42 ± 0.04
$\lambda 1335$	20.01	13.86 ± 0.02	6.93 ± 0.13	4.54 ± 0.02
C III	-5.89	13.41 ± 0.15	9.33 ± 0.76	4.80 ± 0.04
$\lambda 977$	10.69	14.66 ± 1.42	8.09 ± 4.89	4.68 ± 0.26
	27.80	13.42 ± 0.18	9.01 ± 1.05	4.77 ± 0.05
	38.05	12.19 ± 0.62	26.33 ± 8.60	5.70 ± 0.31
C IV	-5.89	13.13 ± 0.09	9.33 ± 0.76	4.80 ± 0.04
$\lambda\lambda 1548, 1550$	10.69	13.05 ± 0.23	8.09 ± 4.89	4.68 ± 0.26
	27.80	13.09 ± 0.11	9.01 ± 1.05	4.77 ± 0.05
	38.05	12.52 ± 0.61	26.33 ± 8.60	5.70 ± 0.31
O VI	-5.89	< 11.36	...	...
$\lambda\lambda 1031, 1027$	10.69	12.62 ± 0.56	7.01 ± 4.24	4.68 ± 0.26
	27.80	< 11.31	...	...
	38.05	12.95 ± 0.63	22.81 ± 6.12	5.70 ± 0.31

4. THE CIRCUMGALACTIC MEDIUM OF MASSIVE GALAXIES

4.1. Introduction

The cycle of baryons in and out of galaxies is an important factor in determining how a galaxy evolves. An active baryon cycle with high accretion rates fuels rapid star formation which generates persistent outflows, resulting in an active blue galaxy. A stalled baryon cycle cannot feed star formation, leading to a red and dead galaxy. The strength of a galaxy's baryon cycle is a direct measure of the galaxy's future health.

To observe the strength of a galaxy's baryon cycle observations of the spatial distribution and kinematics of gas in the galaxy's halo are required. The diffuse nature of the galaxy's circumgalactic medium (CGM) requires observing it in absorption. By observing the absorption profiles of different ions in the spectra of background objects such as quasars the spatial extend and kinematic structure of different phases of the CGM can be determined.

The connection between the activity of a galaxy and the nature of its CGM is most easily studied in simulations. Cosmological hydrodynamic simulations of galaxy evolution reveal how epochs of star formation generate metal rich halos through the implementation of stellar feedback models such as stellar winds from AGB stars, supernovae, radiation pressure, and photoheating. Studies have revealed the importance of stellar feedback to create the metal-rich halos observed around galaxies (e.g. Wiersma et al. 2011; Smith et al. 2011; Hummels et al. 2013; Ford et al. 2013, 2014; Liang et al. 2016).

To verify the accuracy of the simulated halos the results need to be compared to observations. There is a large body of work of CGM observations at low redshift

($z < 1$), such as the COS-Halos survey (Tumlinson et al. 2013), the COS-Dwarfs (Bordoloi et al. 2014), and the MAGIICAT sample (Nielsen et al. 2013b).

There are few studies of the CGM at at $z \sim 1 - 2$ due to the galaxy's emission lines being pushed into the IR. Between $z = 2.5 - 3$ the rest-frame UV absorption features are pushed into the optical, enabling a small redshift window where CGM absorption studies are possible. The Keck Baryonic Structure Survey (KBSS, Rudie et al. (2012)).

Despite the difficulties in observing the role the baryon cycle plays in high redshift galaxy evolution, there are several astrophysical reasons why the high redshift regime of galaxy evolution is useful. The cosmic star formation rate density peak at $z \approx 2$ (Madau & Dickinson 2014). The baryon cycle is fueled by stellar feedback that occurs during periods of active star formation. Studying the CGM at $z \approx 2$ can give insight into how the baryon cycle reacts to strong star formation.

Additionally between z=2-1 the dominant mode of accretion for massive galaxies is predicted to change from cold-mode to hot-mode (Dekel & Birnboim 2006). The change of accretion modes is due to gas properties of the halo being able to support shocks in the CGM and preventing gas from cooling efficiently. This phase shift of the CGM be observable in the absorption lines of multiple ions.

The focus of the work presented in this chapter was to explore the high redshift CGM of galaxies in cosmological hydrodynamic simulations. The focus on redshifts from 4 to 1 enabled the study of how periods of intense star formation altered the CGM of the galaxies and how the change in accretion modes would affect observations. As there are very few observational constraints in this redshift

regime the results presented here serve as a prediction of future observations.

4.2. Methods

To explore the CGM around high-mass galaxies the simulations in the VELA suite (Ceverino et al. 2014) were used. The simulations are described in depth in §2.2.3.

The VELA2b simulations used were analyzed with the MOCKSPEC code. All snapshots between $a = 0.2$ ($z = 4$) and the last snapshot available, typically $a \approx 0.5$ ($z \approx 1$), were analyzed. The snapshots were output in steps of $\Delta a = 0.01$ resulting in roughly 30 snapshots capturing the evolution of the galaxies. Each snapshot was processed with MOCKSPEC using 1000 LOS with impact parameters randomly selected out to 1.5 R_{vir} with an edge-on orientation. To select gas across the range of ionization parameters spectra were generated for HI, MgII, CIV, and OVI with the HIRES instrumental properties ($R \sim 45,000$). The SNR used was set to 30 which imposed an effective EW cut of $\sim$0.01 Å.

4.3. Results

4.3.1. EW vs. D

The simplest method for examining the spread of metal through the CGM when it has been observed in absorption is the behavior of the equivalent width (EW) with impact parameter D. The EW profile in each VELA2b simulation and each ion processed with MOCKSPEC is shown in Figures 4.1 - 4.6. Figures 4.1 - 4.3 show the EW profile when D is measured in units of R_{vir} while Figures 4.4 - 4.6 show the EW profile when D is measured in units of kpc. In each plot the points

give the mean EW (<EW>) of detections in a bin of impact parameters with

For simplicity only EW profiles for the z = 1,2,3, and 4 snapshots of the simulations are shown. At high redshift the EW profiles will not extend to as large of impact parameters as the EW profiles at low redshift when D is measured in kpc. This cutoff is a consequence of how the simulation box is removed from the larger cosmological simulation. The size of the smaller box used by `MOCKSPEC` is a multiple of R_{vir} which changes as the galaxy grows. Consequently, the high redshift CGM was not sampled to the same physical distance as the low redshift CGM.

Figures 4.1, 4.2, and 4.3 show the EW profiles with D scaled by R_{vir} for `VELA2b-21`-`VELA2b-23`, `VELA2b-24`-`VELA2b-26`, and `VELA2b-27`,29 respectively. The environment, history, and star formation rate for each halo varies at each snapshot presented; however, there are a few trends in the EW profile that are common to all halos.

For all halos, the mean EW_{HI} profile is highest (largest <EW>) at z=4 and lowest (smallest <EW>) at z=1. This fall in <EW> occurs at all D. The largest <EW> at all snapshots for HI occur in the inner regions of the halo. For all halos the drop off of <EW> with increasing D is relatively flat outside of $D \approx 0.2\ R_{vir}$. Inside this limit the <EW> is typically half a dex stronger than immediately outside the limit. The disparity between the two regions is likely due to the inner region being dominated by the galaxy's ISM which contains more compact gas which would result in a higher EW.

The MgII profiles showed notable redshift evolution for all halos. The maximum spatial extent where MgII was still detected dropped significantly from

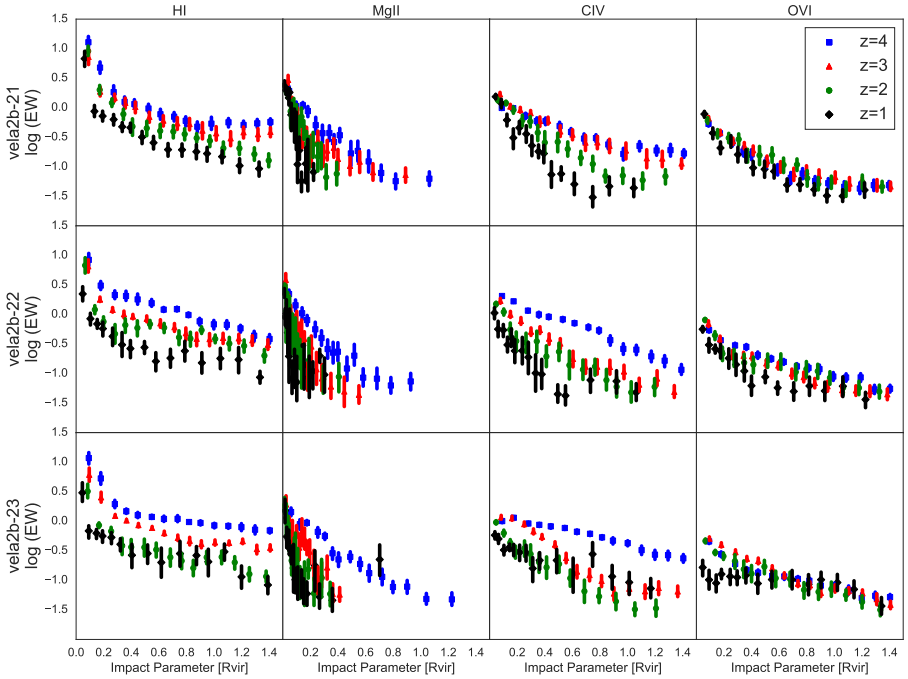

Fig. 4.1.— The behavior of the mean equivalent width with impact parameter measured in units of R_{vir} for `VELA2b-21` - `VELA2b-23`. Only the $z = 1, 2, 3, 4$ snapshots are shown for clarity. Each column is a different ion and each row is a different halo. There was notable evolution for each ion and halo over time with the general trend of moving towards weaker absorption at a given impact parameter as redshift decreases. All ions except MgII were found at all impact parameters. As the halo evolves the spatial extent of MgII decreases due to the increase of R_{vir} as the halo grows.

greater than 1 R_{vir} at z=4 to less than 0.5 R_{vir} at z=1.

The CIV profile showed similar evolution as the HI profile and was found at all impact parameters. At z=4 the typical CIV <EW> in the outer CGM ($D > 0.3$) R_{vir} was between 0.5-1 dex higher than at z=1.

Contrary to the other ions, the OVI <EW> profile showed the least amount of redshift evolution. Only `VELA2b-26` showed significant evolution in the outer CGM ($D > 0.5$ R_{vir}). `VELA2b-23` and `VELA2b-29` both showed notable evolution in the inner halo ($D < 0.2$ R_{vir}) with the <EW> increasing with time. All other

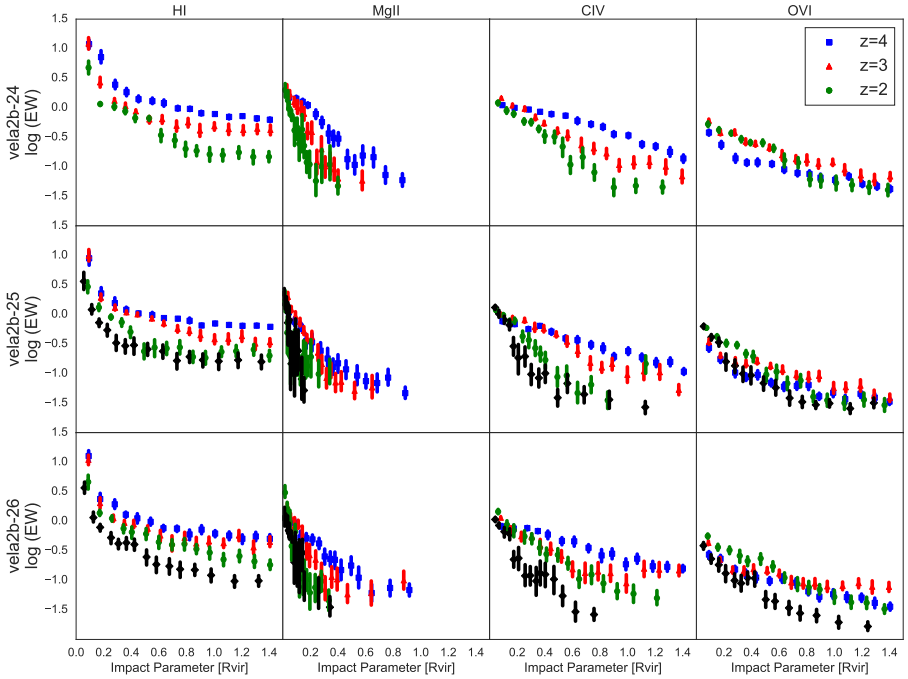

Fig. 4.2.— The same as Figure 4.1 but for `VELA2b-24`, `VELA2b-25`, and `VELA2b-26`. The `VELA2b-24` simulation did not reach $z = 1$ so only data for $z = 2$, 3, and 4 are shown.

halos did not show significant redshift evolution in the <EW> of O VI.

When studying the evolution of the CGM as traced by absorption lines it is important to examine the radial profiles with the impact parameter measured in both physical units (such as kpc) and scaled by R_{vir}. Scaling by R_{vir} details the relative importance of the observed structures to the overall halo but can lead to misleading redshift evolution as R_{vir} is not constant with time. The <EW> radial profiles showed trends with redshift when D was modulated by R_{vir}. Figures 4.4 - 4.6 show the same profiles but with D measured in proper kpc (pkpc).

Immediately it was apparent most of the redshift evolution discussed above were actually due to the evolution of R_{vir} as the trends disappear when D was measured in physical units. The <EW> profiles for H I, Mg II, and C IV showed no

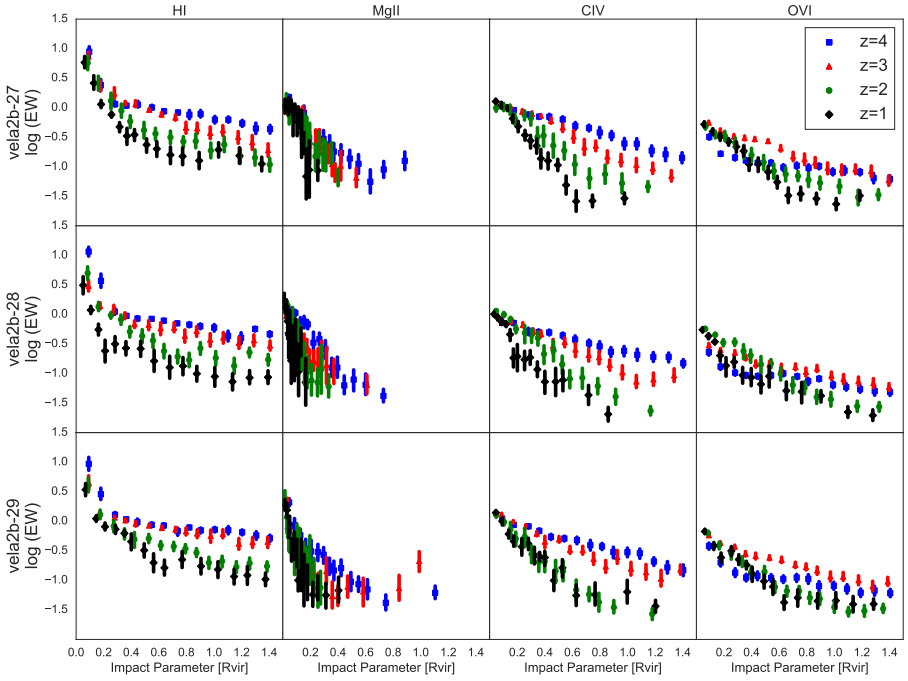

Fig. 4.3.— The same as Figure 4.1 but for `VELA2b-27`, `VELA2b-28`, and `VELA2b-29`.

significant redshift evolution at any impact parameter in any halo. The only minor exception was the <EW> of CIV in the outer CGM ($D > 100$ kpc) of `VELA2b-23` and `VELA2b-29`. Both halos showed a rise in the CIV <EW> at $z = 1$. Both halos also experienced numerous mergers with mass ratios ($M_{sat}/M_{host} > 0.3$) at this time, suggesting the rise in equivalent width of CIV was due to the presence of satellite galaxies.

To quantify the effect D scaling has on the evolution of the EW radial profiles linear fits of the form $\log(\mathrm{EW}) = mD + b$ were generated for each profile. The variance of the fitted slope for each ion is shown in Table 4.1. The second column shows the variance in the slope over time when D was scaled by R_{vir}. The third column shows the variance in the slope over time when D was measured in kpc. The contrast was clear with the variance with R_{vir} scaling typically being two order

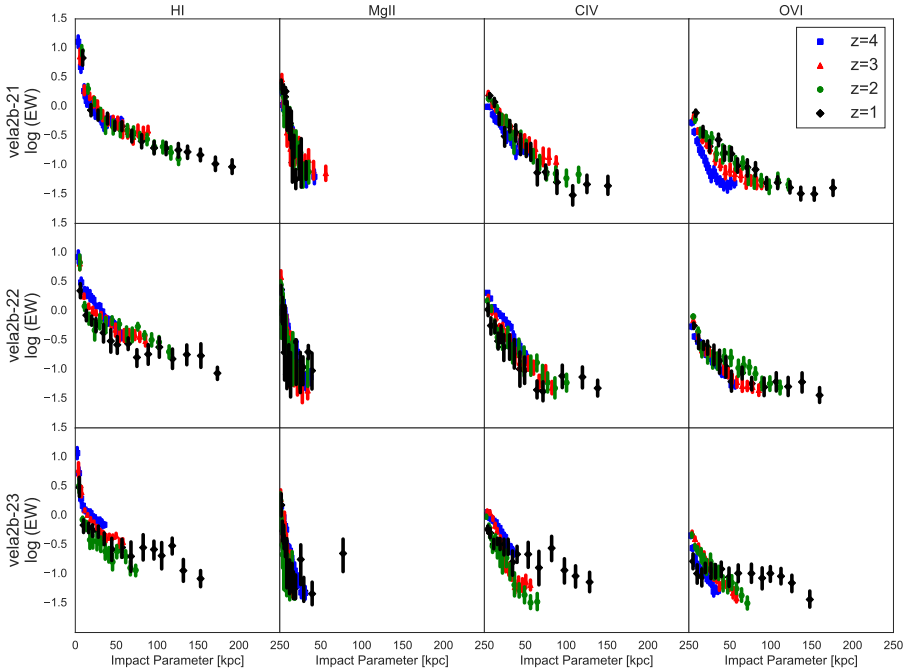

Fig. 4.4.— The same as Figure 4.1 except the impact parameter is in units of pkpc. The increased spatial extent of detections with decreasing redshift was a consequence of how the zoom-in halos were extracted from the larger cosmological simulation as the box size was determined in units of R_{vir}, which increased with time. With the impact parameter in physical units the strong trend of decreased <EW> with decreased z mostly disappeared, suggesting the actual spatial extent of the CGM does not evolve significantly. The exception is O VI which still showed notable redshift evolution. Also contrary to the other ions, O VI generally moves to stronger absorption features with time.

of magnitude larger than the variance when D was not scaled. The intercepts of the fits showed no variation depending on the scaling used for D as it only depended on the equivalent width at D=0.

As before, O VI defied the same trends as the lower ions. The <EW> of detected O VI increased at all D as the halos evolved. For all halos the weakest <EW> of O VI occurred at $z = 4$. For all halos except `VELA2b-22`, `VELA2b-23`, and `VELA2b-26` the strongest <EW> of O VI occurred at $z = 1$. `VELA2b-22`, `VELA2b-23`, and `VELA2b-26` were notable for having the three lowest <sSFR> of

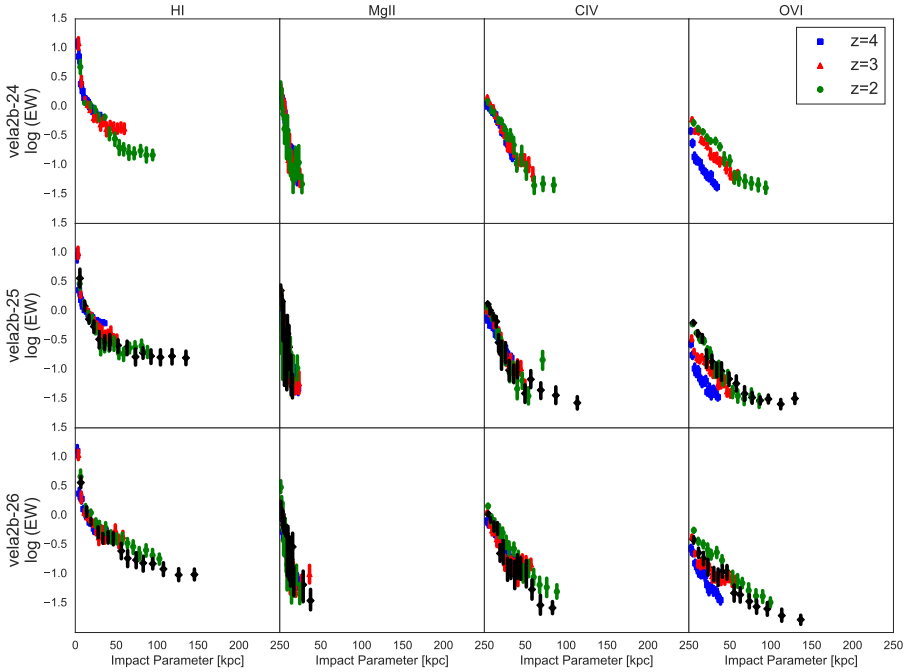

Fig. 4.5.— The same as Figure 4.4 but for `VELA2b-24`, `VELA2b-25`, and `VELA2b-26`. The `VELA2b-24` simulation did not reach $z = 1$ so only data for $z = 2$, 3, and 4 are shown.

the `VELA2b` simulations, *suggesting the strength of detected* O VI *is correlated with the star formation rate of the host galaxy*, in agreement with observations of lower redshift galaxies (e.g. Tumlinson et al. 2011).

The similarity of the <EW> with D across the various `VELA2b` halos motivated the creation of an "average" halo. Treating the halos as the same galaxy creates a typical <EW> profile that averages over the different environments and

Table 4.1. Variance in the Fitting Parameters of EW profile scaling

Ion	σ^2_{Rvir}	σ^2_{kpc}
HI	0.201	0.004
MgII	1.729	0.022
CIV	0.267	0.004
OVI	0.175	0.003

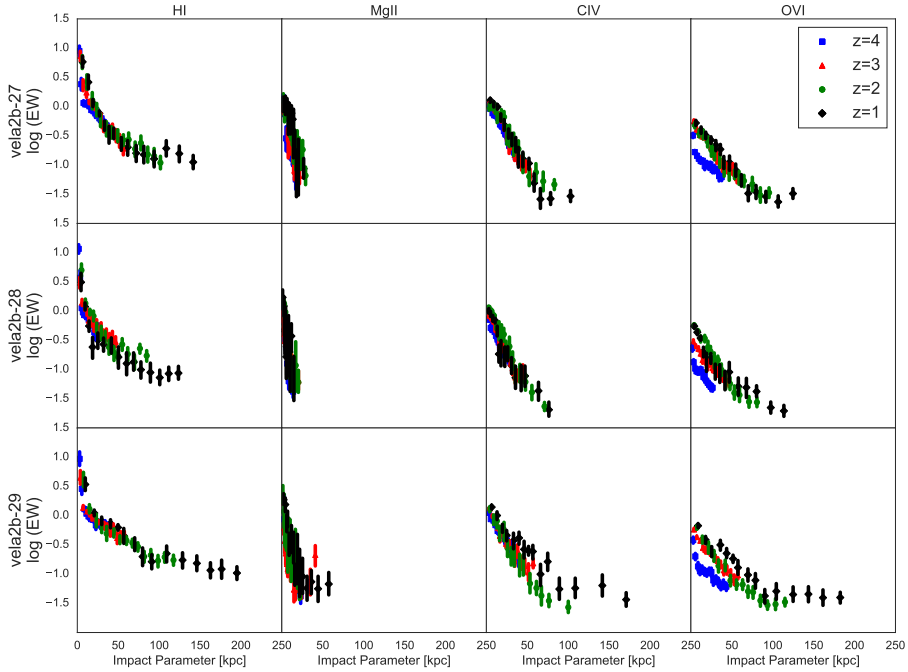

Fig. 4.6.— The same as Figure 4.4 but for `VELA2b-27`, `VELA2b-28`, and `VELA2b-29`.

histories of each halo. The results of the typical halo are shown in Figure 4.7 (D scaled by R_{vir}) and Figure 4.8 (D in kpc).

The trends in the evolution of <EW> as a function of D scaled by R_{vir} for each ion discussed above remained when the halos were treated as one. The <EW> of detected HI absorption decreases by $\sim$ 1 dex at all impact parameters as the typical halo evolves. In the most inner region of the halo ($D < 0.2\ R_{vir}$) had significantly stronger HI absorption than the outer regions, again due to ISM contamination. When D was measured in units of kpc the detected HI <EW> vs. D evolution disappeared.

The evolution of the <EW> of MgII in the composite halo were the same as the evolution of the <EW> of MgII in the separate halos. At a given D/R_{vir} the <EW> of MgII absorption decreased as the halo evolved. As in the individual

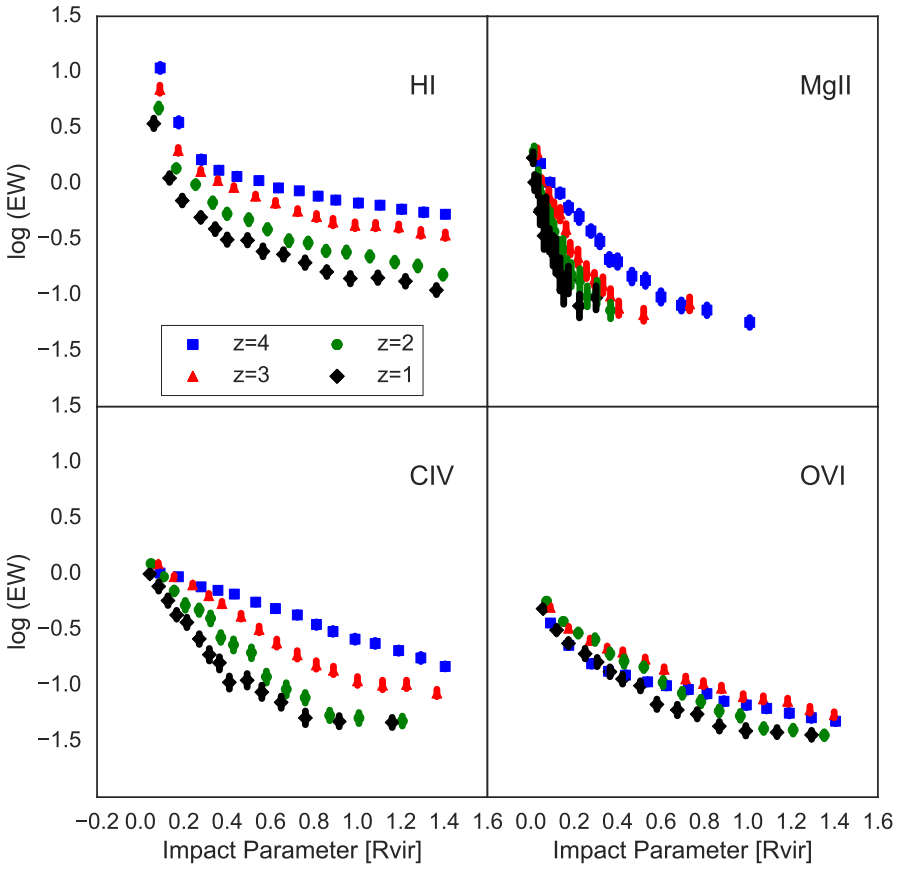

Fig. 4.7.— The evolution of absorber strength of each ion as a function of impact parameter scaled by R_{vir} for all VELA2b halos averaged together. The evolution noted in Figures 4.1 - 4.3 are prominent in the averaged halo. The detected absorption of HI, MgII, and CIV in the CGM decreased in EW as the halo evolved. The mean strength of OVI increased at $z = 3$ then reached a minimum at $z = 1$.

halos, this behavior did not trace any CGM evolution but instead R_{vir} evolution as the trend once again disappeared when D was measured by physical units. Similar trends were found in the <EW> vs D of profiles for CIV absorption.

The <EW> vs. D profile for OVI did not follow the same trends as the lower ions. When D was scaled by R_{vir}, the <EW> of detected OVI at all impact parameters was the weakest at z=1. The strongest <EW> occurred at z=3 for all impact parameters. Unlike with the lower ions, the redshift evolution for <EW>

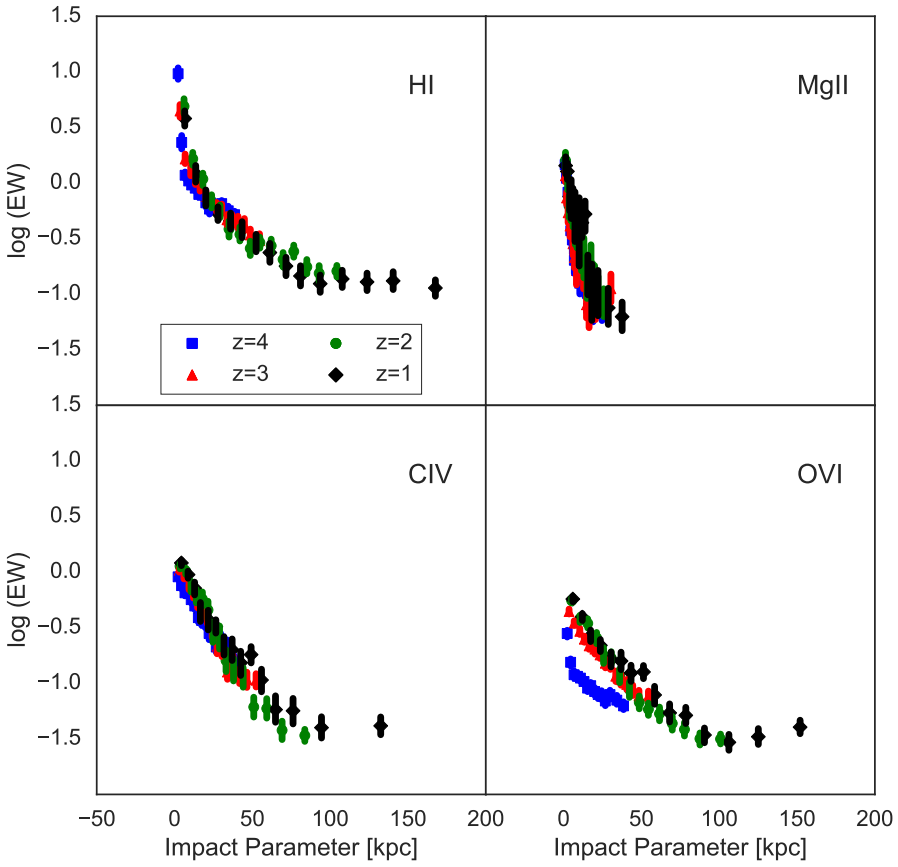

Fig. 4.8.— The same as Figure 4.7 but with the impact parameter measured in physical units. As before, when the impact parameter is measured in physical units the evolution of <EW> with D disappears for HI, MgII, and CIV. The evolution of <EW> with D for OVI becomes more prominent and tends to increase with time.

vs. D for OVI did not change when impact parameter was measured in physical units. The trend reversed with the strength of OVI being the weakest at z=4 and strongest at z=1 at all D.

4.3.2. Covering Fraction

To quantify the likelihood of detected significant absorption in a given LOS it is useful to calculate the covering fraction (C_f) of an ion as a function of impact

parameter. The covering fraction is defined as the ratio of the number of LOS in a given impact parameter bin that detected absorption with an EW above a cutoff value (EW_{cutoff}) to the total number of LOS in the same impact parameter bin. The result can be thought of as the probability of detecting absorption with EW $> \mathrm{EW}_{cutoff}$ at a given impact parameter.

In this section the C_f of each ion was calculated as a function of D measured in both R_{vir} and kpc for each halo and the composite halo introduced in the previous section. The

The evolution of the covering fraction of each ion as a function of D/R_{vir} for the composite halo s shown in Figure 4.9. Similar to the EW vs. D profile discussed in the previous section, there was very little variance between the covering fraction of the halos, so only the composite halo is shown here. There was significant evolution in the covering fraction of all ions at fixed D/R_{vir} with the covering fraction decreasing over time. At z=4, the covering fraction of HI, CIV, and OVI were near unity for all LOS. The spatial extent of MgII was as great with the covering fraction dropping to less than 20% at $D \approx$0.8 R_{vir}.

By z=1, the covering fraction of all ions had dropped significantly in the outer regions of the CGM. The covering fraction of CIV and OVI dropped below 20% at $D \approx$0.7 R_{vir} and $D \approx$ 1.3 R_{vir} respectively. The covering fraction of HI never dropped below 40%. The region of detectable MgII had decreased significantly, with the covering fraction dropping to zero beyond D=0.4 R_{vir}.

Motivated by the observation that the EW vs D evolution disappeared when the impact parameter was reported in physical units, the Figure 4.9 was repeated with the impact parameter measured in kpc in Figure 4.10. As expected the

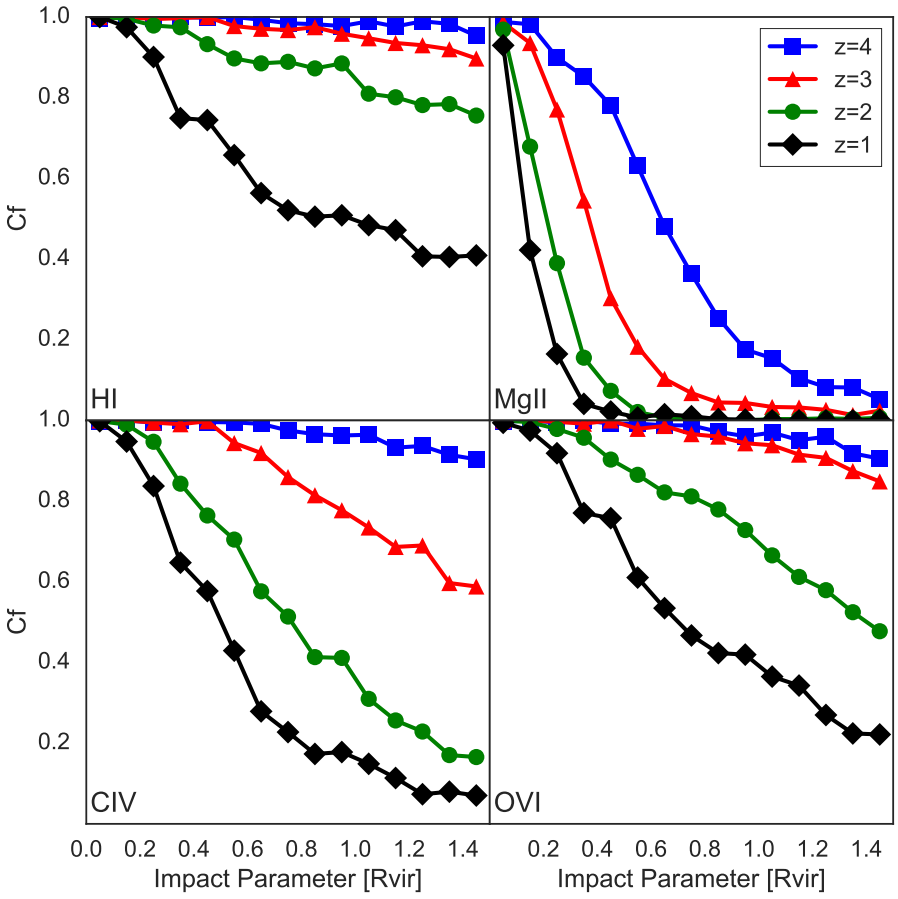

Fig. 4.9.— The covering fraction for each ion as a function of impact parameter in units of R_{vir}. All ions showed similar evolution in their covering fractions with the covering fraction dropping at fixed D/R_{vir} with time. An EW cut of 0.1 Å was applied

majority of the redshift evolution found in Figure 4.9 was due to evolution in R_{vir}. The covering fraction of MgII had no redshift evolution. Any LOS with detectable MgII was located within 60 kpc of the galaxy as the covering fraction was zero beyond $D = 60$ kpc.

The covering fraction of CIV and OVI still showed some redshift evolution with the non-modulated impact parameters. At a fixed D the covering fraction of both ions dropped from z=4 to z=1 although not as much as with the modu-

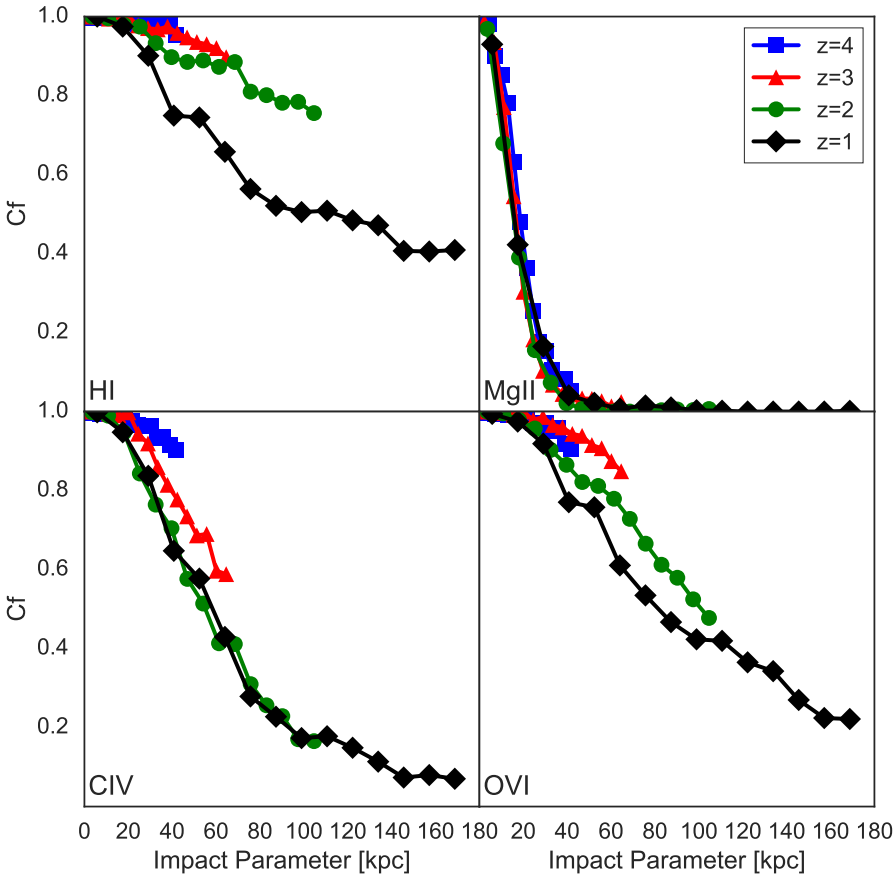

Fig. 4.10.— The covering fraction for each ion as a function of impact parameter in units of kpc. The evolutionary trends found in Figure 4.9 were still found here with the covering fraction at fixed D dropping over time. However the trend was much less pronounced. The covering fraction of Mg II showed the least evolution while O VI showed the most evolution of the metal lines. An EW cut of 0.1 Å was applied.

lated impact parameter. For example, the covering fraction of C IV at D=40 kpc dropped from ∼90% to ∼70% between z=4 and z=1.

The covering fraction of H I showed little evolution between z=4 and z=2 but dropped noticeable at all impact parameters between z=2 and z=1. Beyond D=40 kpc the H I covering fraction dropped by ∼20%.

4.3.3. Phase

One of the key strengths of the MOCKSPEC code is its ability to identify which gas cells along a LOS are responsible for the detected absorption. The gas cells intercepted by the LOS are removed from the generation of the synthetic spectrum until the resulting spectrum's EW is 5% smaller than the unaltered spectrum. The resulting cells were identified as the as the significantly absorbing gas cells. In this section the phase of the gas cells responsible for the detected absorption in each halo for each ion are presented. Examining the phase of the absorbing gas cells illustrates the type of gas each ion effectively probes and is helpful in determining the dominate physical properties in the CGM such as the dominate ionization mechanism for each ion.

The phase of the all gas cells in a typical simulation is shown in Figure 4.11. To aid with the following discussion the phase diagram was split into four regions. The coldest gas with $T < 10^{4.5}$ K was predominately located within the galaxy and was hence given the label of "ISM". The temperature region between $10^{3.5}$ K and $10^{4.5}$ K is a thermodynamically stable temperature region as cooling times are long in this temperature range. Gas in this temperature region was given the label of "Cool CGM". Hot gas ($T > 10^{4.5}$ K) was split based on the density of the gas. Hot gas with $n_H < 10^2$ cm^{-3} was classified as "Hot Diffuse CGM" and gas with $n_H > 10^{-2}$ cm^{-3} was classified as "Hot Dense CGM". By mass the dominate phase regions in the simulation was the Cool CGM and the Hot Diffuse CGM.

The phase of all gas cells that contributed significantly to detected HI absorption features around the composite halo are shown in the top row of Figure 4.12. Gas can generate detectable HI absorption at nearly all available phases. The

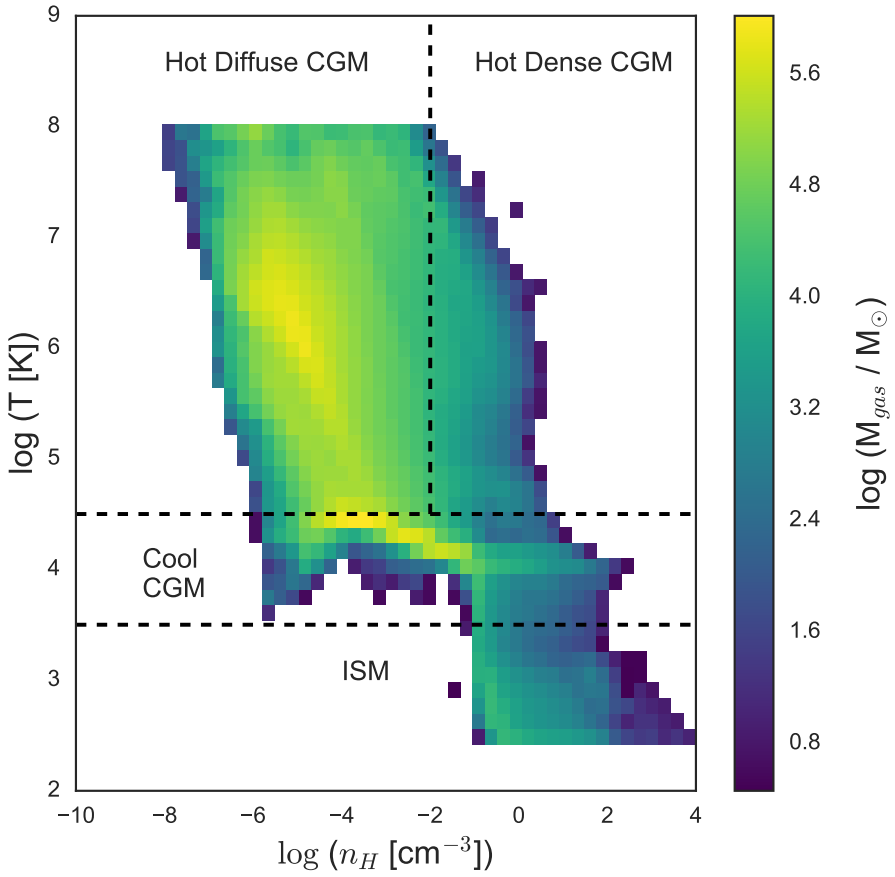

Fig. 4.11.— The phase diagram for all gas cells in `VELA2b-25` at z=2. The color of each bin corresponds to the total gas mass with the given phase. The diagram was split into four regions for clarity in discussions. The simulations impose a temperature ceiling of 10^8 K and floor of 300 K. The simulations do not impose a density limit beyond the activation of star formation in dense regions.

only region of the full phase diagram missing in the H I absorber phase diagrams was the very hot, diffuse gas ($T > 10^7$ K, $n_H < 10^{-5}$ cm^{-3}).

The majority of the mass of gas generate H I absorption lies in the Cool CGM. In all simulations and across all snapshots a large concentration of H I absorbing gas was found here.

There were two notable transient features in the composite halo. The first

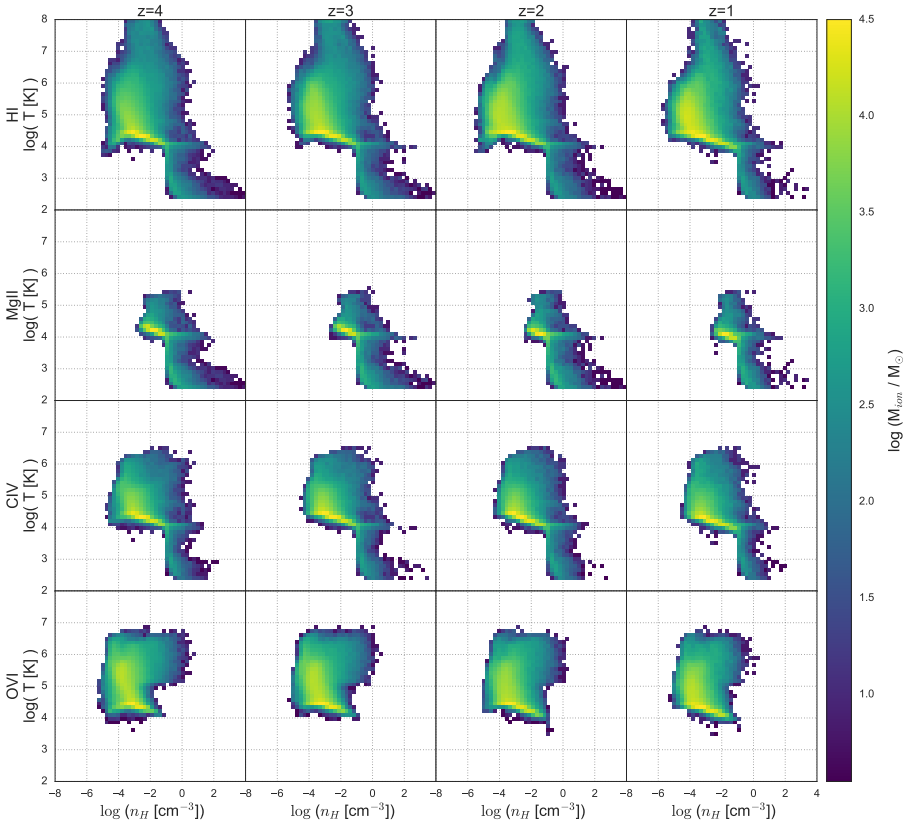

Fig. 4.12.— The evolution of the phase of gas cells contributing to detected absorption for the composite halo. Each row is a different ion with redshift evolution shown left to right. The color corresponds to the mass of the ions in each phase bin.

occurred in the low density end of the Cool CGM. At high-z there was a small extension with at less than 10^4 K and less than 10^{-4} cm^{-3}. The extension was most prominent in the z=4 and z=2 snapshots. A small version of the extension existed at z=3 but it was completely absent at z=1. The cool, diffuse part of the phase diagram is indicative of cool inflows (see Chapter 5 for details), which are stronger at higher redshift as seen here

The second phase evolution in the HI absorbing cells was the increase in the gas mass in the Hot Diffuse phase (T$> 10^{4.5}$ K, $n_H < 10^{-2}$ cm^{-3}) with time. The

Hot Diffuse phase of the CGM is the preferred phase of outflowing gas generated by stellar feedback as seen in the O VI phase below.

The phase diagrams for gas cells that were responsible for the detected Mg II absorption are shown in the second row of Figure 4.12. There is a notable difference between the Mg II phase diagrams and the H I phase diagrams as the gas responsible for the detected Mg II absorption was restricted to a smaller region of the available phase space. Across all halos and time the majority of gas cells generating Mg II absorption resided in the dense Cool CGM and ISM. No gas cells with $n_H < 10^{-3}$ cm^{-3} generate detectable Mg II absorption.

There was little trend in the Mg II absorbing phase space with redshift, suggesting Mg II absorption always probes the same type of gas regardless of where or when the observing material lies.

The phase diagrams for gas cells that were responsible for the detected C IV absorption are shown in the third row of Figure 4.12. The peak in the phase distribution for all halos peak in the Cool CGM with densities between 10^{-4} - 10^{-2} cm^{-3}. However, gas in the ISM and both Hot phase regions were also able to generate C IV absorption. There was a maximum temperature to all snapshots of 10^6 K as no gas hotter than this contributed to detectable C IV absorption.

The phase diagrams for gas cells that were responsible for the detected O VI absorption are shown in the bottom row of Figure 4.12. The strongest difference between the O VI phase diagrams and the lower ions was the lack of any contribution from the ISM phase. The coldest gas to contribute to O VI was $T = 10^4$ K.

The phase distribution of O VI absorbing gas was distributed between the Cool

CGM and the Hot Diffuse CGM. The nature of the two peaks in the distribution of gas phases for O VI absorbing cells gives insight into the underlying physics, namely the dominate ionization mechanism for O VI. Collisionally ionizing oxygen atoms into the O VI state requires temperatures of $10^{5.5}$ K and densities of 10^{-4} cm^{-3}. Hotter gas will be pushed into higher ionization states such as O VII while cooler gas will reach equilibrium in lower ionization states such as O V. The phase of the hot peak matches the requirements for collisionally ionized O VI. To generate O VI in the cool peak requires the dominate ionization mechanism to be photoionization. The dominate ionization mechanism for O VI is a debated topic in literature (Oppenheimer & Davé 2009; van de Voort & Schaye 2012; Oppenheimer & Schaye 2013a; Heckman et al. 2002; Cen & Chisari 2011; Faerman et al. 2017) and is discussed more in §4.4.2.

4.4. Discussion

4.4.1. Evolution of the CGM

A strength of the `VELA` simulation suite is the ability to study the evolution of the CGM for halos with a different histories. The galaxies studied here evolved in a variety of environments and experienced different merger histories. All the galaxies were active star formers throughout the times studied with sSFR $> 10^{-11}$ yr^{-1} at all times.

Observations have established relations between the star formation rate of galaxies and the strength of various ion absorption features in the CGM of the galaxy. Tumlinson et al. (2011) established a strong correlation between the column density of O VI and the sSFR of the galaxy.

A recurring theme in the analysis of the simulated CGM was the lack of evolution in the spatial distribution of the metals detected in absorption. When the trends of EW and C_f were plotted against D the behavior across time changed depending on the scaling of D. A standard way of normalizing the size of the CGM for various galaxies with different masses is to divide D by the galaxy's R_{vir} (Nielsen et al. 2013a; Churchill et al. 2013). When the size of the simulated halos were normalized with their R_{vir} the EW and C_f profiles showed notable redshift evolution. When D was instead presented in units of kpc, showing the true physical extent of the CGM, most redshift trends disappeared, suggesting the dominate source of the detected trends in EW and covering fraction with the modulated impact parameter were due to the evolution in R_{vir}.

The slight evolution in covering fraction shown in Figure 4.10 suggests the CGM became more patchy with time. At a fixed impact parameter, a drop in covering fraction over redshift means detections are less likely, but the constant EW means the detections found would have the same strength. Taken together suggests the CGM starts to break apart at low redshift, with gaps in absorbing material forming.

The lack of significant redshift evolution is apparent in Figures 4.13 - 4.16 which show the location around the composite galaxy of all detections. The color of each point denoted the strength of the absorption. The composition galaxy was aligned to lie along the x-axis. The dotted black circle denotes the average R_{vir} of the halos at the time point.

The method by which the LOS are generated lead to a few artifacts in the plots. When the LOS were generated by `MOCKSPEC` the impact parameter was

pulled from a uniform distribution ranging from 0-1.5 R_{vir}. Since each galaxy had a different R_{vir} the same LOS impact lead to slightly different impact parameters when measured in kpc. Since the azimuthal angle α was generated using a constant seed, the result was a radial pattern in the maps.

Additionally, since each galaxy had a different R_{vir}, the true extent each halo was probed with LOS was different. At z=2, two halos (`VELA2b-21` and `VELA2b-22`) were notably more massive than the rest resulting in their halos being probed to a larger physical distance. The sphere like structure in the z=3 plot was a result of two of the halos being probed to a larger distance than the rest.

The map of the distribution of HI around the composite galaxy is shown in Figure 4.13. From the covering fraction plots of HI (Figure 4.9 and 4.10) HI absorption was detected at all probed impact parameters, in agreement with the EW map. As the halo evolves HI was still detected at all distances with little change to the distribution of equivalent widths.

The map of the distribution of MgII around the composite galaxy is shown in Figure 4.14. The distribution of EW(MgII) with D showed that MgII was not detected beyond 40 kpc. At z=4, the mean maximum impact parameter used was 45 kpc resulting in the detected near uniform covering fraction. As the DM halo grew larger impact parameters were probed, but the size of the CGM traced by MgII absorption did not increase in size. Comparing the map of MgII at z=1 and z=4, the size is nearly the same. The distribution does evolve from a spherical shape at high redshift to a flattened distribution aligned with the disk of the galaxy. However the flattening was not statistically significant.

The map of the distribution of CIV around the composite galaxy is shown in

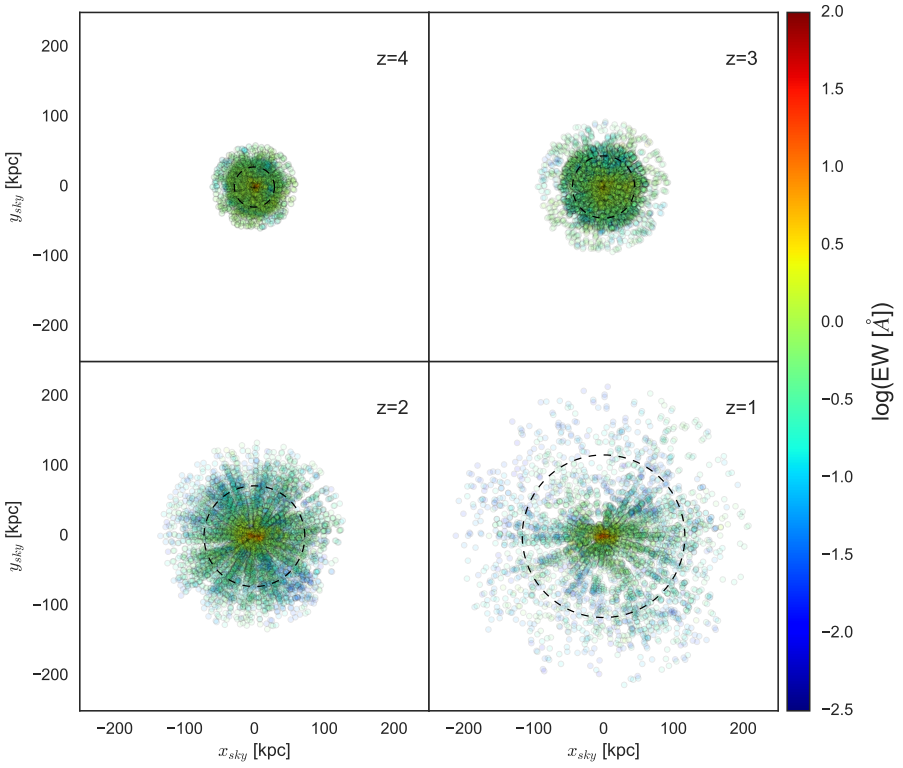

Fig. 4.13.— The location and EW(H I) of all detections around all the composite halo. The galaxy is aligned along the x-axis. The dotted circle denotes the average R_{vir} of the halos at that time step. The color of each point denotes the EW(H I) of the detections. The ray-like patterns evident in z=2 and z=1 panels was a result of how the LOS were generated.

Figure 4.15. The spatial extent of C IV was larger than that of Mg II, consistently extending beyond the virial radius of the galaxy. It is likely C IV could be detected beyond the probed distance at z=4.

Examining the evolution of the detection of C IV it appeared the density of detections decreased with time. This is an artifact of how the LOS were generated. With the impact parameter pulled from a uniform distribution between 0 - 1.5 R_{vir}, the density of LOS in a square kpc of the projected CGM would decrease as R_{vir} grows. The paucity of detected in the z=1 halo as compared to the z=4

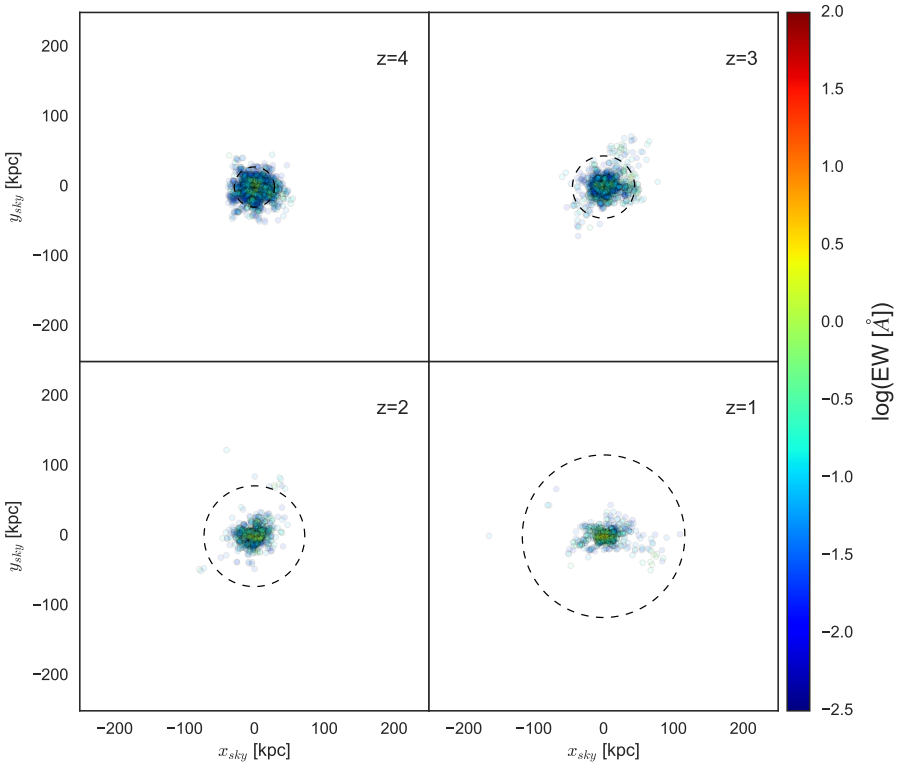

Fig. 4.14.— The location and EW(Mg II) of all detections around all the composite halo. The galaxy is aligned along the x-axis. The dotted circle denotes the average R_{vir} of the halos at that time step. The color of each point denotes the EW(Mg II) of the detections

halo is due to a decreased sampling rate as the halo grew.

The map of the distribution of O VI around the composite galaxy is shown in Figure 4.16. O VI shared many of the same qualities as the C IV map such as the extension beyond R_{vir} and the decrease density of detections as the halo grows. O VI was detected at all impact parameters probed, suggesting the O VI CGM extends farther out.

The lack of evolution in the simulated CGM was a consequence of the growth history of the galaxy. At the simplest levels, the presence of metals in the CGM is a consequence of star formation and the resulting distribution of metal enriched

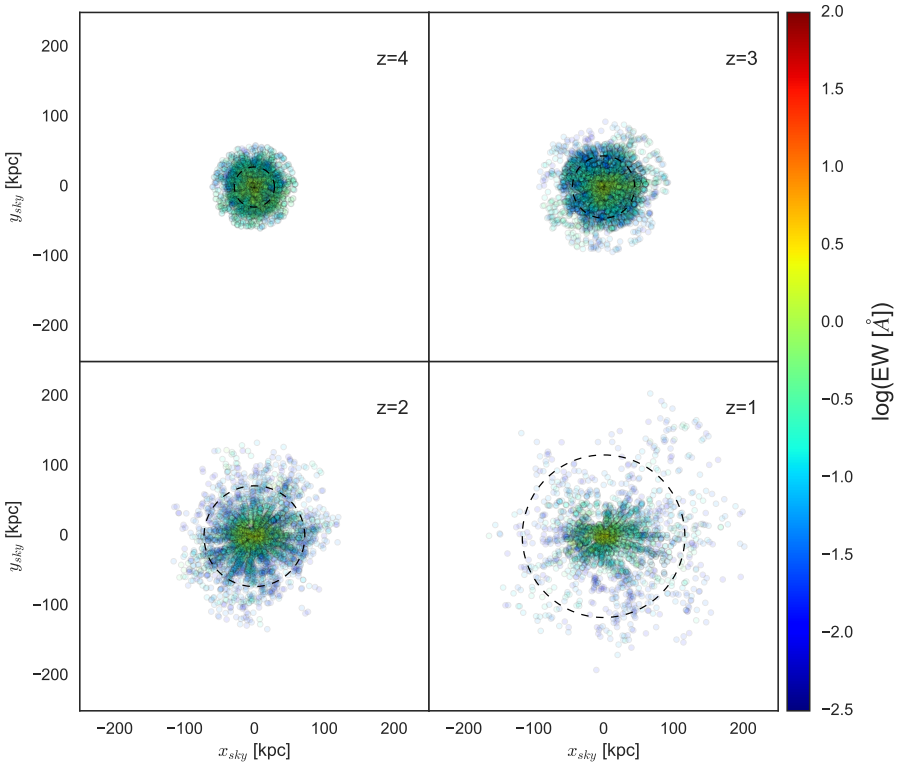

Fig. 4.15.— The location and EW(C IV) of all detections around all the composite halo. The galaxy is aligned along the x-axis. The dotted circle denotes the average R_{vir} of the halos at that time step. The color of each point denotes the EW(C IV) of the detections

gas via stellar feedback out into the halo. The galaxies in the VELA2b suite formed 90% of their stars before z=4 on average and had accreted 95% of their z=1 virial mass by z=4. The halos were fully established before the cosmic epoch over which they were studied. As the galaxies only formed 10% of their final stellar mass during the cosmic time range studied here, it was not surprising the CGM of the galaxies did not change significantly in spatial extent or phase.

The size of the observable CGM was calculated by measuring the impact parameter that encompasses 90% of all detections for each ion, named D_{90}. This limiting impact parameter was calculated twice with differing EW cuts. Initially

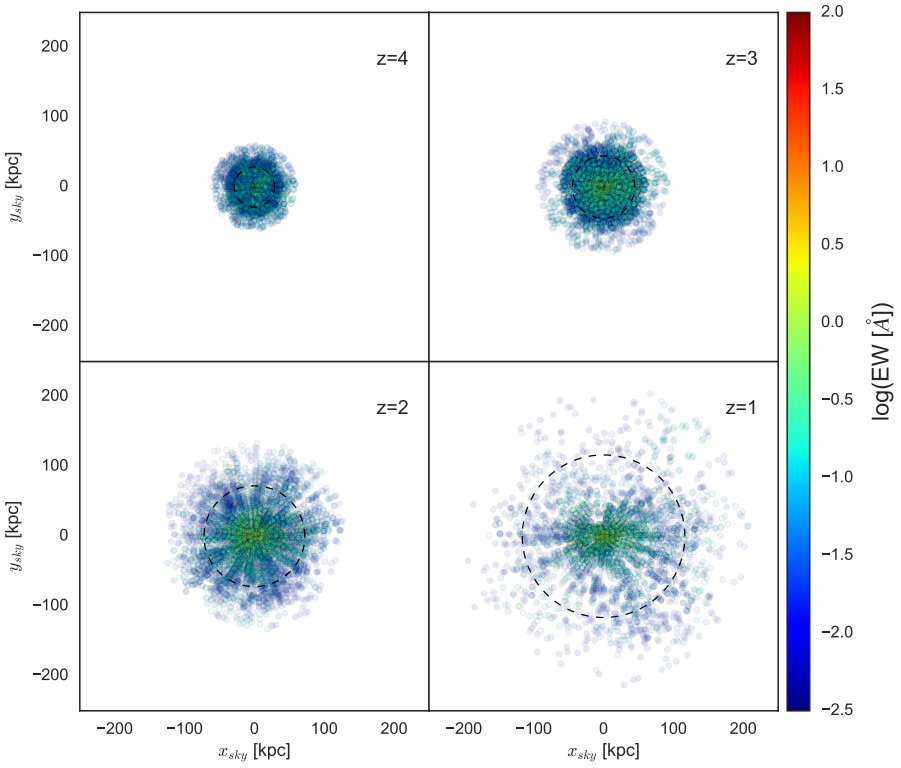

Fig. 4.16.— The location and EW(O VI) of all detections around all the composite halo. The galaxy is aligned along the x-axis. The dotted circle denotes the average R_{vir} of the halos at that time step. The color of each point denotes the EW(O VI) of the detections

the only EW cut was the effective EW cut imposed by the noise in the spectrum (D_{90}^{0}). Then a typical observational EW cut of 0.1 Å was applied to emulate what an observer would detect ($D_{90}^{0.1}$). A common EW delimiter to separate "weak" absorbers from "strong" absorbers is 0.3 Å (e.g. Nielsen et al. 2013b), was also calculated ($D_{90}^{0.3}$). The last cut applied was 1.0 Å which only selected the strongest absorbers. The evolution of these properties for the composite halo for all snapshots is shown in Figure 4.17.

The size of the H I halo expanded as the halo grew, a result of the increased maximum impact parameter used in `MOCKSPEC`. When only the strongest H I ab-

sorbers were used ($D_{90}^{1.0}$) the size of the HI CGM did not evolve staying at ∼30 kpc.

Conversely, the MgII halo never increased past $D_{90}^{0.1}$ ∼20 kpc or D_{90}^{0} ∼ 30 kpc. The strongest MgII absorbers were found only within ∼5 kpc, well within the range of ISM.

The CIV CGM extended roughly as far as the HI CGM, but the outer regions were too weak to be detectable in most observations. With the observational limit applied the CIV CGM grew with time but at a decelerating rate. It appeared to be plateau at $D_{90}^{0.1}$ ∼ 75 kpc at z=2.5. The stronger the EW cut applied the less evolution was found for the size of the CGM traced by CIV.

The OVI halo grew constantly and did not appear to plateau but the observable OVI size did begin to plateau by z=1 at ∼80 kpc. It is important to note the increase in D_{90} for HI, CIV, and OVI was tied to the increase in the space probed by LOS due to the increase in the simulation size with time.

The apparent size evolution of the CGM as traced by HI, CIV, and OVI cannot be directly interpreted as an increase in the size of the actual CGM. The spatial extent of the CGM as determined by observations from `MOCKSPEC` is limited to the size of the simulation box used, which is dependent on the halo's virial radius which increases with time. Suppose the true spatial extent of the CIV CGM including the weakest observable detections ($D_{90}^{0.1}$) is beyond the edges of the simulation box and is constant with time. As the galaxy halo grows and the size of the space probed by `MOCKSPEC` increases, the size of the CIV would increase as well. Eventually the box size would overtake the boundaries of the observable CIV halo and `MOCKSPEC` would detect the edge. The resulting evolution of D_{90}

would be an increase with time until a turnover point, beyond which the size of the halo would not increase. This trend is similar to the trend found for the size of the weak HI, CIV, and OVI halos. When only the strongest absorbers were used ($D_{90}^{1.0}$) the size of the halos for all ions did not evolve with time.

The size of the OVI halo traced by strong absorbers ($D_{90}^{0.3}$) did show small evolution, increasing from ∼10 kpc to ∼40 kpc over the duration of the simulations. The increased OVI halo was a result of the constant star formation.

In Pallottini et al. (2014) the CGM of high-z galaxies were examined to determine the evolution of the EW of HI. The EW was calculated from the column density of HI pulled directly from projections of the simulations. They found the EW vs D profile of HI does not evolve between z=4 and z=2, in agreement with the results presented here.

The lack of evolution of the CGM has been noted in a few observational studies. Most notably, Chen (2012) compared the $z \approx 2.2$ CGM to the $z \sim 0$ CGM by examining how the EW profile of Lyα, MgII, and CIV changed and found the spatial extent and the mean EW did not significantly change over this time. The observational results agree with the work done here despite the differing redshift regime. Taken together, the results suggest the CGM of large galaxies are built up before z=4 and do not evolve significantly thereafter. Studies of the evolution of the strength of MgII observations over large redshift ranges support a constant CGM. Matejek & Simcoe (2012), for example, studied the strength of MgII absorbers with $1.9 < z < 6.3$ and found no significant evolution. They concluded the MgII in halos of galaxies must be generated before z=6, in agreement with the results here.

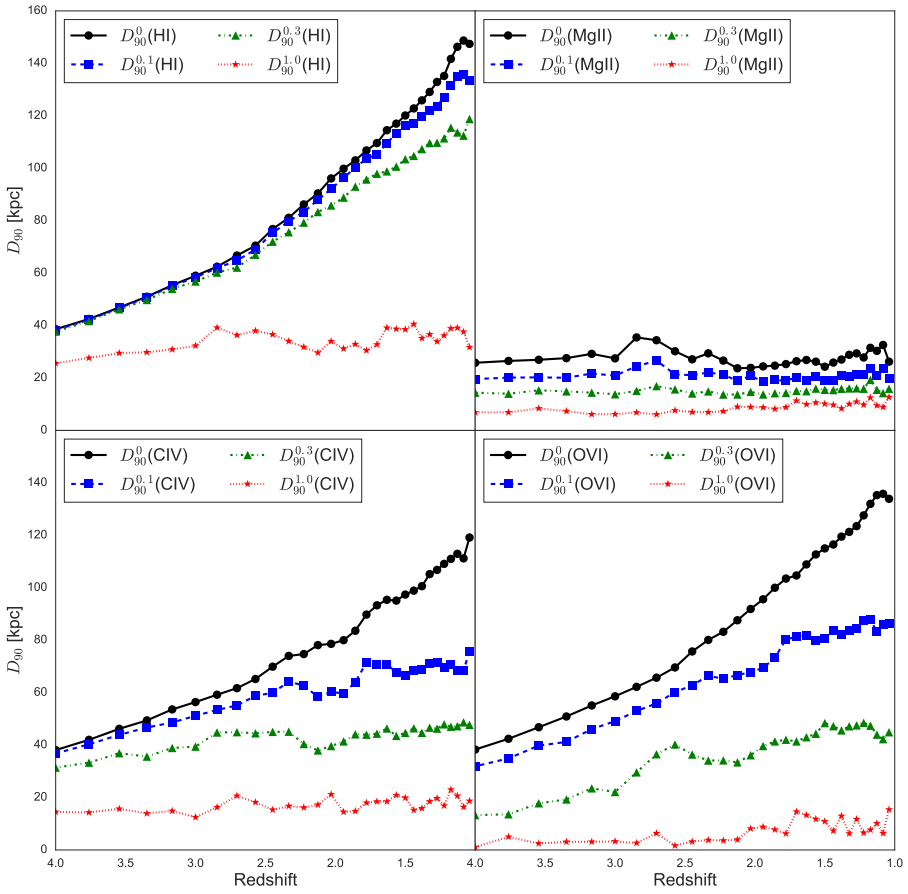

Fig. 4.17.— The evolution of the physical size of the CGM in the composite VELA as is measured with D_{90}^{cut}, the impact parameter that encompasses 90% of detections with an EW> *cut*. For each ion four cuts are shown. The black lines are D_{90} with no additional EW cut applied, the blue lines show a typical observational limit of 0.1 Å, the green lines applied a cut of 0.3 Å, a typical delineation between "weak" and "strong" absorbers and the red lines only the strongest absorbers with a cut of 1.0 Å. When all detected absorbers are included, the CGM traced by HI, CIV, and OVI seem to increase in size with time but this is a consequence of the size of the probed CGM increasing with time as the galaxy grows. As weaker absorption features were cut from the sample by increasing the EW cut, the size of the detected halo decreases at all redshifts. With the strictest cuts, the size of the halo for all ions does not increase with time. The MgII halo size did not grow independent of the EW cut.

4.4.2. OVI *Ionization Mechanism*

Several studies of the OVI absorption in the CGM of galaxies have revealed a great deal about the nature of the absorbing materials. The COS-Halos study

initial results described how the amount of O VI detected in absorption at $z \sim 0.25$ as measured by it column density ($N_{\rm O\,VI}$) is strongly correlated with the specific star formation rate of the galaxy (Tumlinson et al. 2011). Passive galaxies (sSFR $< 10^{-11}$ yr^{-1}) tended to have low column density absorbers or column densities below the detection limit. Ionization modeling of the absorbers put lower limits on the mass of O VI in the galaxy revealing the CGM hosts as much mass in metals as in the ISM (Peeples et al. 2014).

While the amount of O VI in halos is well-studied, the nature of the absorbers is relatively unknown. If O VI is collisionally ionized the absorbers would be large, hot, and diffuse structures, such as a hot ambient halo component (Cen & Chisari 2011; Smith et al. 2011; Faerman et al. 2017). If instead the O VI absorbing gas was photoionized then it could reside in a colder and denser structure (Oppenheimer & Davé 2009). The cold structures could be tracing cold accretion (Kereš et al. 2005; van de Voort & Schaye 2012) or the enhanced local radiation field produced by recent star formation. Understanding the ionization mechanism of O VI is vital to correctly constraining the mass and physical sizes of the gas responsible for the absorption.

The two dominant ionization mechanisms for O VI, collisional ionization and photoionization, have two distinct distributions on the phase diagram. Collisionally ionized O VI peaks at $10^{5.5}$ K and 10^{-4} cm^{-3}(Sutherland & Dopita 1993). Photoionization dominates in colder gas and is most commonly found at 10^4 K (Bergeron et al. 1994; Oppenheimer & Davé 2009). By taking advantage of the distinct phase differences of the two ionization mechanisms the ionization method of the detected O VI in the `VELA` simulations were studied. In the phase diagrams presented in §4.3.3 the O VI absorbing gas were often concentrated in two regions,

namely the Cool CGM and the Hot Diffuse CGM. The temperatures and densities of these phase regions suggests the gas in the Cool CGM was photoionized while the gas in the Hot Diffuse CGM was collisionally ionized. The Cool CGM peak was present in every snapshot while the hot peak was more transient.

To explore the cause of the presence of the hot peak the fraction of gas mass contributing to detected O VI in the Hot Diffuse CGM phase and the Cool CGM phase relative to the total gas mass (f_{Hot} and f_{Cool} respectively) was compared to multiple galaxy properties such as M_{vir}, M_*, SFR, sSFR, and the number of high mass satellites ($M_{sat}/M_{host} \geq 0.1$). The majority of O VI absorbing cells resided in these two phases ($f_{Hot} + f_{Cool} \simeq 1$) so the comparisons between f_{Cool} would be redundant.

The strongest correlation was between the fraction of O VI mass in the Hot Diffuse CGM phase and the galaxy's sSFR, with a Kendall's τ of 0.46 (8.4σ). The correlation is shown in Figure 4.18. The correlation between f_{Hot} and the SFR of the galaxy was only r = 0.29, suggesting the dominant ionization mechanism for observed O VI depends on both the galaxy's SFR and stellar mass. The `VELA2`b simulations had relatively constant SFR. Since the stellar mass continuously grew the sSFR decreased with time, causing the observed decrease in the size of the hot peak in the O VI phase diagrams.

The correlation between the presence of the Hot Diffuse CGM and the current sSFR suggests collisionally ionized O VI is causally connected to winds from stellar feedback. The constant presence of the Cool CGM suggests the photoionized gas arises from a persistent feature in the simulations. Previous works have suggested photoionized O VI may arise from cold flows (Kereš et al. 2005; Dekel et al. 2009;

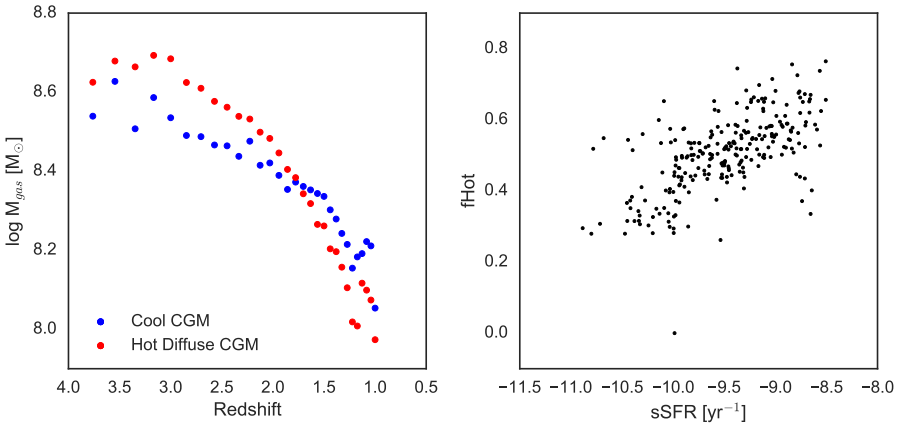

Fig. 4.18.— Behavior of the size of the Hot Diffuse phase of gas generating detectable O VI. *Left:* The mass of absorbing cells in the Cold CGM phase and the Hot Diffuse CGM phase over redshift. The total mass in both phases decrease with time. As the halos evolve the relative importance of the Hot Diffuse CGM phase decreased as the mass of the Cool CGM overtook it. The values were averaged over all halos at each redshift. *Right:* The relation between the fraction of the mass in the Hot Diffuse CGM phase to the sSFR of the galaxy. Each snapshot of each halo was plotted as an independent point. The properties were correlated with $\tau = 0.46$ at the 8.4σ level.

van de Voort & Schaye 2012) or from gas near the galaxy being ionized from young stars (Oppenheimer & Schaye 2013b; Suresh et al. 2017). The `MOCKSPEC` ionization correct does not take into account the local radiation field from stars leaving the possibility of photoionized O VI tracing cold flows. Cold flows are predicted to be a prominent feature in the halos of high redshift galaxies, supporting this interpretation (Dekel et al. 2009).

For observations of the O VI CGM the mix of ionization methods could cause complications with modeling. The likelihood of a complication depends on how likely a given LOS with O VI absorption is a result of both photoionized gas and collisionally ionized gas. To determine this likelihood each LOS that detected O VI in any `VELA` snapshot was classified as either a collisional LOS or a photo LOS based on the median temperature of the gas cells that generated the absorption

($T < 10^{4.5}$ K is photo).

In Figure 4.19 the evolution of the ionization classification of LOS is presented. For each snapshot the fraction of LOS with detectable O VI absorption that were classified as being dominated by collisional ionization was calculated. At high redshift, roughly 90% of the LOS were dominated by collisional ionization. The fraction remained relatively constant until $\sim z = 3$ when it started to decrease. By z=1 the fraction had dropped to ~65%.

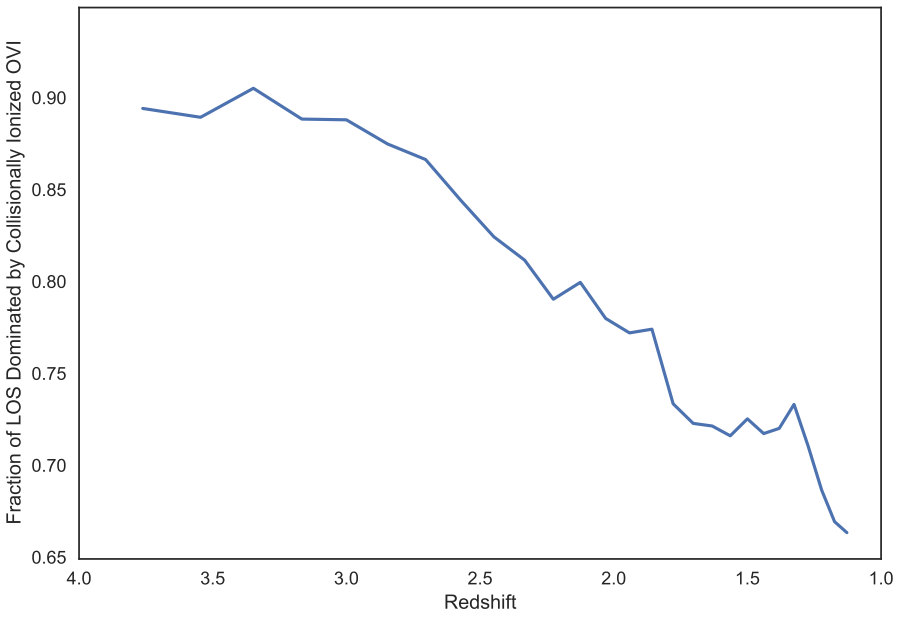

Fig. 4.19.— The evolution of the fraction of LOS through all `VELA` with detectable O VI absorption that are dominated by collisionally ionization. The fraction decreases with time, but remains above 65%.

Figure 4.19 only examined the dominate ionization mechanism of each LOS. In Figure 4.20 the fraction of cells along the LOS that have the same class as the LOS are shown as a function of redshift. This plot demonstrates the "purity" of

the cells responsible for the detected O VI for a LOS. The solid line denotes the mean value across all LOS with detectable O VI absorption and the shaded regions denote the 1σ variations. The fraction of cells along a collisionally ionized LOS that contributed to the O VI absorption that are collisionally ionized remained constant with time at ∼80%. For photoionized LOS, the fraction of cells that were photoionized was lower at ∼60% at high-z and ∼70% at low-z. While it is likely to detect absorption due to purely collisionally ionized O VI, it is unlikely to detect absorption due to purely photoionized O VI in this redshift regime.

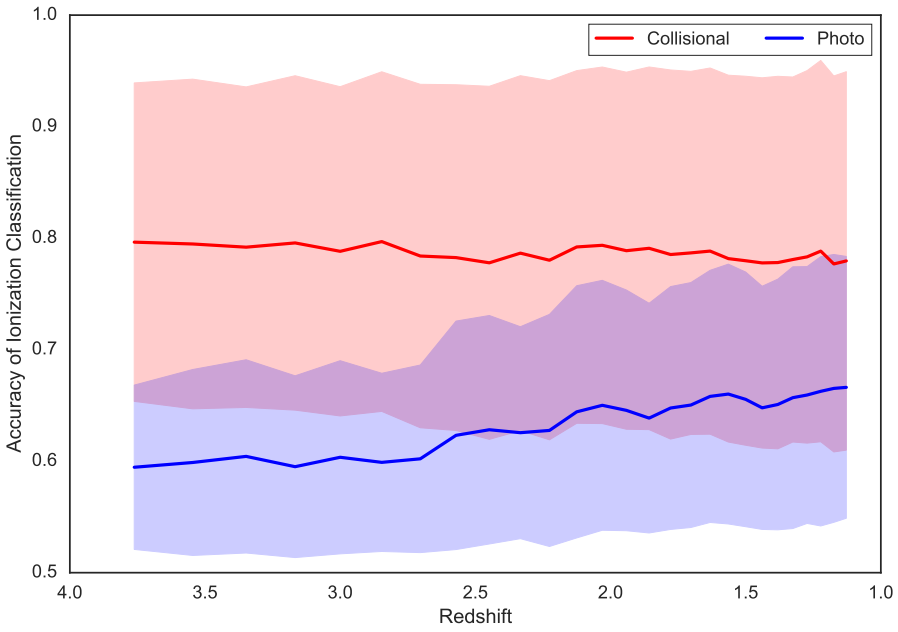

Fig. 4.20.— The fraction of cells whose ionization mechanism classification agrees with the classification of the LOS. The solid line denotes the mean value across all LOS with detectable O VI absorption and the shaded regions denote the 1σ variations. As the halo evolves the accuracy of the classification of collisionally ionized LOS remains constant at ∼80% while the accuracy of the classification of photoionized LOS increases. For a given LOS with O VI absorption, if the median temperature of the gas cells responsible for the absorption is $> 10^{4.5}$ K it is likely nearly all the cells are dominated by collisional ionization. If the median temperature is < 104.5 K, then it is likely a significant number of the cells contributing to the absorption feature are not dominated by photoionization until lower redshifts.

The domination of collisionally ionized O VI in absorption studies contrasts with recent work by Rahmati et al. (2016) studying the dominate ionization methods of highly ionized metals in the Evolution and Assembly of Galaxies and their Environments (EAGLE) simulations. They found the majority of O VI absorbers were photoionized at z=3, with only 20% at most being collisionally ionized. They also found the reverse trend with redshift, finding the importance of collisional ionization increasing with time. The discrepancy could be the result of any of the differences between the two studies. It was shown in Figure 4.18 that the importance of collisionally ionized O VI depends on the galaxy's sSFR. Since the entire VELA sample has high sSFRs, collisional ionization would be important in all detected absorbers. The EAGLE simulations included both passive and active star forming galaxies which would increase the typical role photoionization has on O VI absorbing gas. The second major difference is the method used. Rahmati et al. (2016) generated projection maps of their galaxy halos to determine column densities while this study generated mock observations of the halos in absorption. To determine the relative importance of each ionization mechanism they compared the temperature of all gas O VI gas cells along the projection axis without testing if the gas would actually contribute to detected absorption resulting in conclusions that would not necessarily be useful to explaining observations. By only examining the properties of gas that are responsible for detectable absorption features the work presented here is directly applicable to interpreting observations.

4.4.3. Comparison with Observations

Studying the simulated CGM is a useful method to learn how the spatial and kinematic distributions of gas manifest themselves in the observational data.

However, the interpretations reach their maximum usefulness when the mock observations match real observations. Unfortunately the number of observations of the high-z CGM is small. The majority of studies focus on galaxies with $z < 1$ which the VELA simulations did not reach.

Steidel et al. (2010) studied the CGM around galaxies between z=2-3 providing one of the few data sets of a comparable samples for the work presented here. The data set consisted of 89 galaxies at $< z >$=2.2 and presented measurements of HI and CIV as a function of D for comparison. The results from the composite VELA halo between z=2-3 are shown in Figure 4.21 which shows the detected absorption in the simulations both as the full set of data points and the binned in the same bins as Steidel et al. (2010). The simulated HI absorption features were weaker than the observed features by $\sim$0.5 dex outside of $D \approx$10 kpc. In the inner regions the simulations detected much larger HI absorption features which is likely due to the orientation of the galaxies. Within $D = 10$ kpc the LOS were directly probing the ISM of the galaxy, which was oriented edge-on, the orientation with the largest possible column density of gas in the ISM. The galaxies in Steidel et al. (2010) did not have a selected orientation and thus likely did not pass through as thick of an ISM as the VELA sample. The simulations failed to generate strong enough CIV absorption to match observations, with the mock absorption features having a weaker equivalent width by $\sim$1 dex in the outer CGM. The simulations matched observations in the ISM, but the strength of the mock CIV should have been stronger than the observed for the same reason the mock HI was stronger than the observations. Overall the VELA simulations did not generate a realistic CGM at $< z >= 2.2$.

As discussed in §4.4.1 the structure of the simulated CGM did not evolve

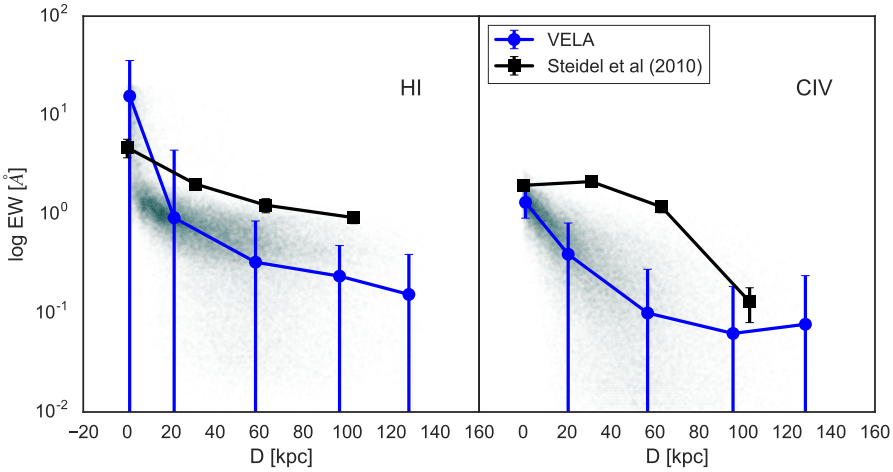

Fig. 4.21.— A comparison between the VELA composite halo between z=2-3 and the observations from Steidel et al. (2010) for HI (*left*) and CIV (*right*). The cyan points are the full mock observations of the VELA halo. The black points are the observational results. The blue points are the geometric mean of the VELA results with the same impact parameter binning as the observational results. Outside of the inner regions the VELA underpredict the strength of HI and CIV absorption.

significantly from z=4 to z=1. With the assumption that the lack of evolution continues to z=0, the VELA CGM can be compared to observations at lower redshifts.

One of the largest low-z surveys of the CGM was the COS-Halos survey (Tumlinson et al. 2013) which used the Cosmic Origins Spectrograph on *HST* to observed the metal absorption of the CGM around 44 galaxies with $0.15< z <0.35$. Despite the difference in redshift the COS-Halos galaxies match the VELA galaxies in stellar mass and SFR making the comparison reasonable. To compare the mock CGM to the observed CGM the covering fractions of HI, MgII, and OVI were compared. Since the simulations did not reach the redshift regime of the observed galaxies, only snapshots with $z < 1.2$ were used. A uniform equivalent width cut of 0.1 Å was applied to match the sensitivity cut of the COS-Halos survey. The resulting covering fractions are shown in Table 4.2.

The COS-Halos covering fractions were divided into two regions: the inner CGM ($D < 75$ kpc) and outer CGM ($D > 75$ kpc). For all ions presented in both spatial regions, the VELA simulations did not produce covering fractions as high as measured by the COS-Halos survey. A significant reason for the low covering fraction in the simulation was the application of an equivalent width cut. The VELA simulations produced metal-line absorption in the extended CGM but with small equivalent widths (EW < 0.1 Å).

In order to match the observations, the VELA simulations would need to increase the metal content of the CGM in the ~ 5.4 Gyr between the end of the VELA simulation and the epoch of the COS-Halos observations. The possibility of enriching the CGM to match observations is not likely as the typical star formation rate of massive galaxies declines after z=1, leading to fewer metals being pushed into the CGM. Additionally, the ionizing radiation of the UVB decreases by roughly an order of magnitude in this time frame, making high ionization species such as CIV less favorable as well.

Alternatively the size of the absorbing structure could increase at lower redshift, creating a longer path length of the LOS. The longer path length would increase the strength of the absorption and has the potential to increase the detection rate of weak absorbing systems. However, the spatial extent of absorbing

Table 4.2. Comparison of C_f between VELA and COS-Halos samples

Ion	$C_{f,V}$ ($D < 75$ kpc)	$C_{f,CH}$ ($D < 75$ kpc)	$C_{f,V}$ ($D > 75$ kpc)	$C_{f,CH}$ ($D > 75$ kpc)
HI	0.749±0.002	0.960±0.040	0.384±0.003	0.970±0.030
MgII	0.166±0.002	0.810±0.110	0.002±0.000	0.430±0.130
OVI	0.592±0.002	0.960±0.040	0.094±0.002	0.820±0.100

systems as parameterized by D_{90} in Figure 4.17 began to plateau for all ions at low redshift, suggesting a future path length increase is unlikely.

The last low-z observational data set the VELA results were compared to was the MAGIICAT sample (Nielsen et al. 2013b) which compiled observations of MgII absorption around galaxies with $0.3< z <1$. Within the VELA simulations the distribution of MgII showed the least amount of evolution suggesting the MAGIICAT results should agree with the simulations. The comparison of the strength of MgII absorption as a function of impact parameter between MAGIICAT and VELA galaxies is shown in Figure 4.22.

Of the observational datasets used in this study, the MAGIICAT sample best matched the VELA sample. The most notable discrepancy between the samples was the lack of strong (EW>1 Å) absorbers in the VELA sample. The lack of strong MgII absorbers in the simulations could be a result of the ionization correction performed in the MOCKSPEC code. While calculating the ionization correction of each gas cell it was assumed that all gas is optically thin. Strong MgII absorbers are likely to arise in gas that is optically thick to ionizing radiation, implying the optically thin assumption would lead to weaker MgII absorbers, as seen here. Overall the MgII absorption in the VELA simulations was in agreement with the MAGIICAT sample.

4.5. Conclusions

In this chapter the CGM of massive galaxies were studied using the MOCKSPEC code as the galaxies evolved from z=4 to z=1. The galaxies were all active star forming galaxies (sSFR> 10^{-11}) and generated strong, metal-rich halos. The

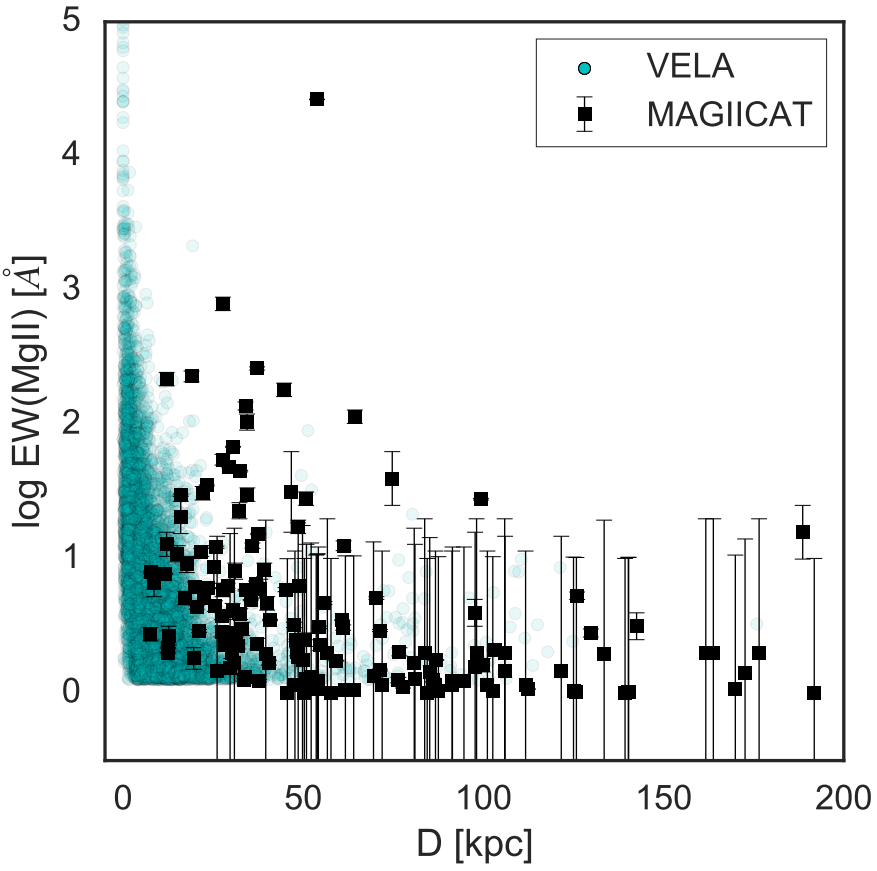

Fig. 4.22.— The unbinned MgII absorption in the VELA simulations plotted with the MAGIICAT simulations. While there was notable overlap between the two samples. The largest discrepancy was the lack of strong (EW>1 Å) absorption in the D=25-100 kpc range in the VELA sample.

behavior of observed absorption properties such as EW and C_f with D were explored as well as the phase of the gas cells responsible for the detected. The conclusions were as follows:

- The strength of absorption as a function of impact parameter does not significantly evolve with time. The covering fraction of HI, CIV, and OVI decrease slightly over time, suggesting a fragmenting CGM.

- Absorption from H I could be detected to large impact parameters, beyond the boundaries of the CGM taken as the virial radius. Mg II was restricted to LOS with $D < 30$ kpc. C IV could be found out to 60 kpc and O VI out to 80 kpc with observational limits. Weak C IV and O VI absorption features below most survey detection limits could be found at all impact parameters.

- The most temporal feature of the CGM was the dominant ionization mechanism for O VI. The fraction of O VI that is collisionally ionized was correlated with the galaxy's sSFR.

- The dominant ionization mechanism for gas cells responsible for O VI absorbing was collisional ionization, responsible for 90% of detected O VI absorption at z=4. The dominance of collisional ionization drops with time as the sSFR of the galaxy drops, reaching a low of 65% at z=1.

- The EW profile with impact parameter of H I and C IV in the `VELA` simulations did not match observations at $< z >$=2.2. A projection of the H I, Mg II, and O VI covering fraction to z=0.2 assuming no evolution did not match the results of the COS-Halos survey. The projection of the EW of Mg II profile to low-z did agree with the results of MAGIICAT.

The conclusions presented here were limited by the sample size of the `VELA` simulation suite. There are few observations of the CGM of high-z surveys, limiting the ability to test the accuracy of the simulations. In the coming years, surveys utilizing integral field spectrometers (IFUs) such as the Multi Unit Spectroscopic Explorer (MUSE) will be able to fill the gap in the observations at high-z.

Additional limitations were generated when the VELA simulation suite failed to create passive galaxies. Many properties of the CGM are correlated with the SFR and sSFR of the galaxy and the lack of diversity in the sSFR of the VELA galaxies limits the diversity of gaseous halos to study. To further verify the results of this study would require a larger sample of more diverse galaxies that have reached low redshift.

When the VELA CGM was compared to the observed CGM from multiple studies at various redshifts, the simulations generally failed to create absorption features strong enough to be consistent with the observations. A likely cause of the weak features was a lack of metals in the simulations relative to observations. To bring the simulations into agreement with observations, the ability of stellar feedback to transport metals into the CGM should be increased through strengthening the energy output of the feedback.

5. EVOLUTION OF COSMOLOGICAL FILAMENTS

5.1. Introduction

As galaxies grow and form stars they consume their supply of gas. Gas consumption timescales are relatively short (∼15% Hubble time scale Daddi et al. (2010); Genzel et al. (2010)). In order for galaxies to maintain their observed star formation rate, galaxies require a sustained supply of gas. The gas can come from IGM accretion, mergers or recycled outflows. Above $z > 1$, galaxies received most of their gas from merging satellites and accretion from the IGM. Both sources tend to bring material along the dark matter (DM) filaments composing the cosmic web (Katz & White 1993; Katz et al. 1993; Bertschinger & Jain 1994; Katz et al. 1994; Bond et al. 1996; Shen et al. 2006; Harford et al. 2008), however the amount of gas contributed by filamentary inflows exceed that from mergers by an order of magnitude (L'Huillier et al. 2012).

As filamentary material merges into a galaxy it encounters the pre-existing halo gas, where it gets shock heated to the virial temperature (T_{vir}) of the halo. For massive galaxies ($M_{vir} > 10^{12}$ $M_\odot$), T_{vir} is high enough to set the gas cooling timescale to several Gyr (Birnboim & Dekel 2003; Kereš et al. 2005, 2009; Dekel & Birnboim 2006; Ocvirk et al. 2008; Brooks et al. 2009; Stewart et al. 2011). The gas must cool before it can condense onto the galaxy and fuel star formation. The long cooling time for the shock-heated gas (∼ several Gyr) means the gas disperses into the halo, eventually reaching the galaxy through relatively smooth deposition. This form of accretion is known as "hot-mode" accretion and is relatively inefficient.

However for smaller galaxies, T_{vir} is low enough that the cooling time is

smaller than the dynamical time. The gas will cool quickly, allowing it to efficiently accrete onto the galaxy "cold-mode" accretion. Since galaxies grow with time, cold-mode dominates in the early universe ($z > 1$) with hot-mode becoming more common in the more recent universe. Galaxies that reside in halos with $M_{vir} < 10^{12}$ $M_{\odot}$ are dominated by cold-mode accretion at all times.

Understanding gaseous filaments and their properties are key to understanding the role of cold mode accretion in galaxy evolution, especially in the high-z universe. However, they are very difficult to study observationally due to their diffuse nature (Faucher-Giguère & Kereš 2011), but there has been some recent success. For example, Crighton et al. (2013) found a metal-poor absorber around a star-forming galaxy at $z = 2.44$ in the spectrum of a background quasar whose kinematic and phase properties matched what would be expected from cold-mode accretion. Systems like these are rare to observe, suggesting simulations are thus key to understanding the nature of cosmological filaments. There have been several studies to meet this challenge.

In Powell et al. (2011), they examined the physical structures that feed galaxies at very high redshift. Using high-resolution simulations, they determined the physical properties of filaments at $z = 9$. Their goal was to determine the extent to which supernova feedback affects the filaments. Incoming gas leads to star formation, which leads to stellar feedback in the form of supernovae. This feedback is very efficient at regulating star formation, but they found has little effect on the filament. They defined the filaments as all gas with $T < 2 \times 10^4$ K and $0.1 \leq n_H \leq 10$ cm^{-3}, showing that at high-z the filaments can be uniquely identified purely by their phase.

Ceverino et al. (2016) examined the relation between material merging into a galaxy from galaxy filaments in simulations to star forming clumps in the disc. They determined that low metallicity Hα-bright clumps are due to pristine accretion from cosmological inflows.

van de Voort & Schaye (2012) examined the connection between star formation rates in galaxies to the modes of gas accretion. They found the cosmological star formation decline at $z = 2$ is due to a decline of cold-mode accretion as the dominant source of material for galaxies. AGN feedback is a vital part of the shift from cold-mode accretion to hot-mode accretion.

Filamentary inflows bring in gas directly from the IGM and thus tend to be very metal poor. Typical mean metallicities are on the order of 10^{-2} and 10^{-3} $Z_{\odot}$, which arise from a large spread of very metal poor gas (pristine material) and metal pollution from small galaxies embedded in the filament (Fumagalli et al. 2011; Shen et al. 2012; Brook et al. 2012).

In this chapter the evolution of the gas contained in a cosmological filament was studied. Using a massive galaxy from the `VELA` cosmological simulation suite, the structure and kinematics of gas selected purely by phase and its response to the hot winds generated by a star formation burst after a merger event were examined. The importance of filament-fed growth of a galaxy as its halo outgrew the filament was addressed.

5.2. Simulations

The study presented here used a zoom-in simulation from the `VELA` simulation suite (Ceverino et al. 2014; Zolotov et al. 2015). The parameters of the `VELA` suite

were addressed in §2.2.3. The galaxy studied here was designated as VELA2b-27. A brief overview of the simulation is given here.

The simulations were perform with the AMR code ART (Kravtsov et al. 1997; Kravtsov 2003). The code included many relevant physical processes for star formation and galaxy evolution, such as gas cooling by atomic hydrogen and helium, metal and molecular hydrogen cooling, photoionization heating by a cosmological UV background.

In addition to the basic physics included in ARTsimulations, this model also used a prescription to describe radiation pressure from stars which added pressure to the cells containing young stars (under 5 Myr) and high gas content ($N_H > 10^{21}$ cm^{-2}).

The VELA simulations used minimum dark matter particle mass of 8.3×10^4 M$_\odot$ and minimum stellar particle mass of 10^3 M$_\odot$. The spatial resolution was 17-35 pc.

The galaxy had a relatively quiet merger history with the exception of a major merger at $z = 2.13$ with a mass ratio (M_{star}/M_{host}) of ∼0.5. The merger created a spike in star formation, raising the nominal SFR from 2–3 M$_\odot$ yr^{-1} to a peak of 25 M$_\odot$ yr^{-1} as shown in Figure 5.1. The star formation was maintained by an

Table 5.1. Initial and final properties of the galaxy

Propriety	Initial Value	Final Value
Redshift	4.00	1.04
Rvir [kpc]	26.8	119.4
Mvir [M$_\odot$]	7.80×10^{10}	$4.01, \times 10^{11}$
Mstar [M$_\odot$]	1.73×10^9	2.02×10^{10}
SFR [M$_\odot$ yr^{-1}]	3.8	2.2 M$_\odot$ yr^{-1}

influx of pristine material from the filament and a constant rate of minor mergers. The increasing M_* means the sSFR of the galaxy is constantly decreasing, but remains above 10^{-10} yr^{-1} throughout the simulation. The quiet history of the galaxy removed the influence mergers might have in the establishment of the gaseous filament. The major merger and resulting starburst allowed for the study of the fragility of the filament.

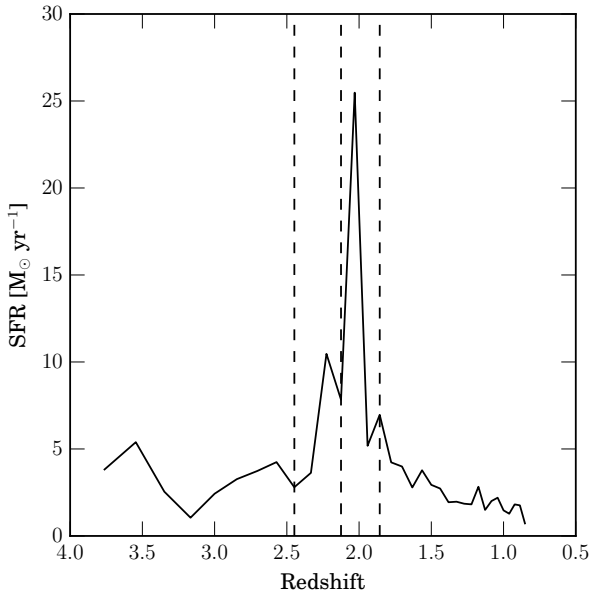

Fig. 5.1.— Star formation rate of the galaxy averaged over roughly 100 Myr bins. The galaxy had a consistent SFR of $\sim 3-4$ M$_\odot$ yr^{-1} outside of the starburst event, when the SFR reaches a peak of 25 M$_\odot$ yr^{-1}. The dashed vertical lines denote the different epochs. The merger occurred during $2.1 < z < 2.5$ and the starburst epoch was defined as $2.1 < z < 1.9$.

Utilizing the merger and starburst four epochs were defined in the history of `VELA2b-27`, summarized in Table 5.2. The formation epoch lasted from the start of the simulation at z=4 until the satellite responsible for the major merger entered the simulation box at z=2.57. The merger epoch was defined as the time

from when the major satellite entered the simulation volume until it merged with the galaxy at z=2.13. The starburst epoch followed, defined by the increase in the galaxy's star formation rate until it returned to pre-merger rates at z=1.86. The final epoch, the relaxation epoch, was started when the starburst ended and lasted until the end of the simulation at z=1.

5.3. Inflow Selection

The primary issue with this work is selecting out the filament material. Since our aim is to characterize the filament, the selection criteria cannot include physical parameters such as the spatial location of possible underlying DM filaments. We restrict the selection of the material to the gas's temperature and density. To guide this section, we used the phase diagram of gas in the simulation showed in Figure 5.2. The most prominent feature is the scarcity of metals in the lower left of diagram. This material exists in a region with $10^{3.5} < T < 10^{4.5}$ K and $10^{-5.5} < n_H < 10^{-2.5}$ cm^{-3}.

When gas only within this phase is selected, we see a clear filamentary structure flowing into the galaxy. The median temperature was constant at $10^{4.4}$ K throughout the duration of the simulation. The median density of the gas in the filamentary selection did evolve and is shown in Figure 5.3. To describe

Table 5.2. Epochs in the Galaxy's Evolution

Epoch	Starting Redshift	Ending Redshift	Description
Formation	4.00	2.57	Filament forms
Merger	2.57	2.13	Major merger occurs
Starburst	2.13	1.86	Peak in star formation rate
Relaxation	1.86	1.00	Return to quiescent state

the evolution the phase selection was split into three regions. Dense gas had $n_H = 10^{-2.5} - 10^{-3.5}$ cm^{-3}, mid gas had $n_H = 10^{-3.5} - 10^{-4.5}$ cm^{-3}, and diffuse gas had $n_H = 10^{-4.5} - 10^{-5.5}$ cm^{-3},

Previous studies of filaments from simulations typically use the dark matter distribution to select out the material. Using the gas properties is beneficial since it is an actual observable, and is the material responsible for the star formation that describes galaxy evolution. Selecting a particular gas phase can be achieved with using quasar absorption lines of select ions.

5.4. General Filament Properties

This section details the general properties of the filamentary gas including passive evolution and time-averaged properties.

5.4.1. Structure

Filaments are a diffuse structure with no clear boundaries. The radius of the filament was defined as the distance from the center of the filament that enclosed 90% of the filament's mass. The size of the filament depended on the density cut used, as shown in Figure 5.4.

Measuring the size of the filament in proper kiloparsecs (pkpc) revealed the structure of the filament with time. Higher density gas resided only in the core of the filament, with a r_{90} of approximately 50 kpc for all snapshots. The inner core of the filament did not change in size with time. The outer regions of the filament were traced by the lower density gas and had larger r_{90} at all times. The difference between r_{90} for the high density gas and the low density gas grew with

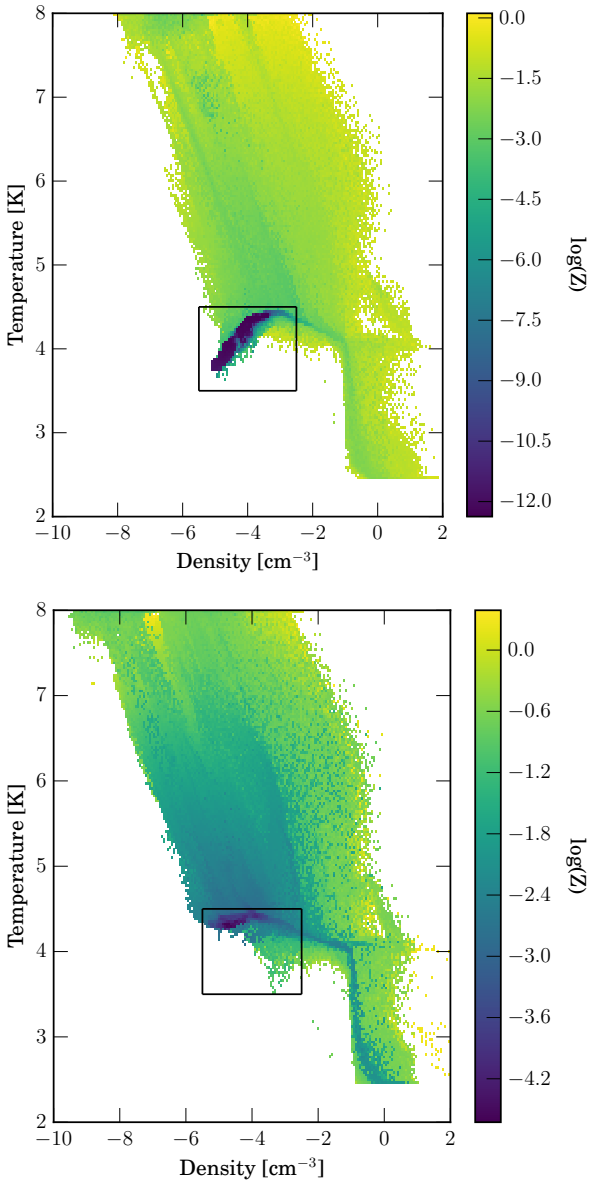

Fig. 5.2.— Phase of gas around the simulation at $z = 4$ (top) and $z = 1$ (bottom), with each bin colored by the minimum metallicity of the gas with that phase. The lowest metallicity gas, presumably associated with "pristine" inflowing material, was predominately located in the lower left corner of the phase diagram, indicated by a box. From these diagrams, it is clear there was notable evolution in this region.

time, reaching a peak difference of ∼150 pkpc at $z = 1.5$. At this point, the low density gas extended 240 kpc from the center of the filament.

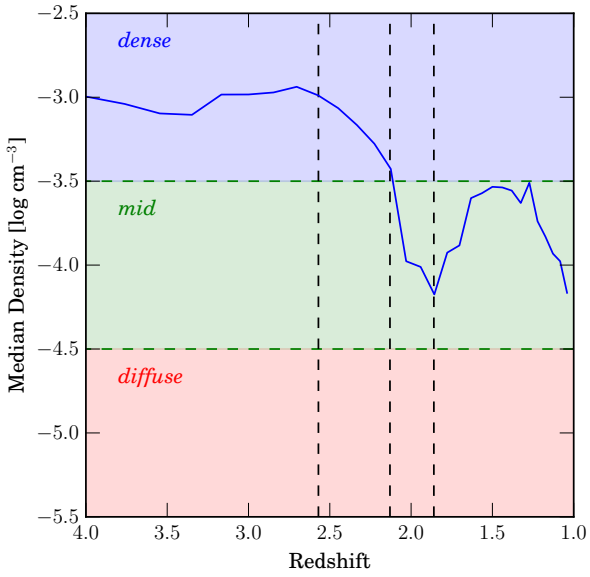

Fig. 5.3.— The median density of the filamentary gas as a function of time. The median density started in the dense selection, but transitioned to the mid density after the merger begins (first vertical line). After the end of the starburst epoch (last vertical line), the median density started to rise again, before dropping after the system recovered from the starburst.

If r_{90} was instead measured in units of R_{vir}, the evolution took a different shape. High density gas still had a smaller r_{90} than lower density gas. For high density gas, r_{90} decreased at a roughly constant rate until $z = 2.0$, when it leveled off at 0.5 R_{vir}. Since the size of this gas in pkpc is constant, the decrease was due to the galaxy's growing virial radius. The low density gas remained at constant distance of 2.75-3.00 R_{vir} until $z = 1.5$. At this point r_{90} dropped quickly.

In Figure 5.4 the size of the filament was averaged over the entire length of the filament. When discussing the physical coherency of the filament, it was useful to look at the evolution of the radius of filament as a function of distance from the galaxy. If the filament's structure was independent of the galaxy and its behavior, then its size would be consistent along its length. The size of the filament along

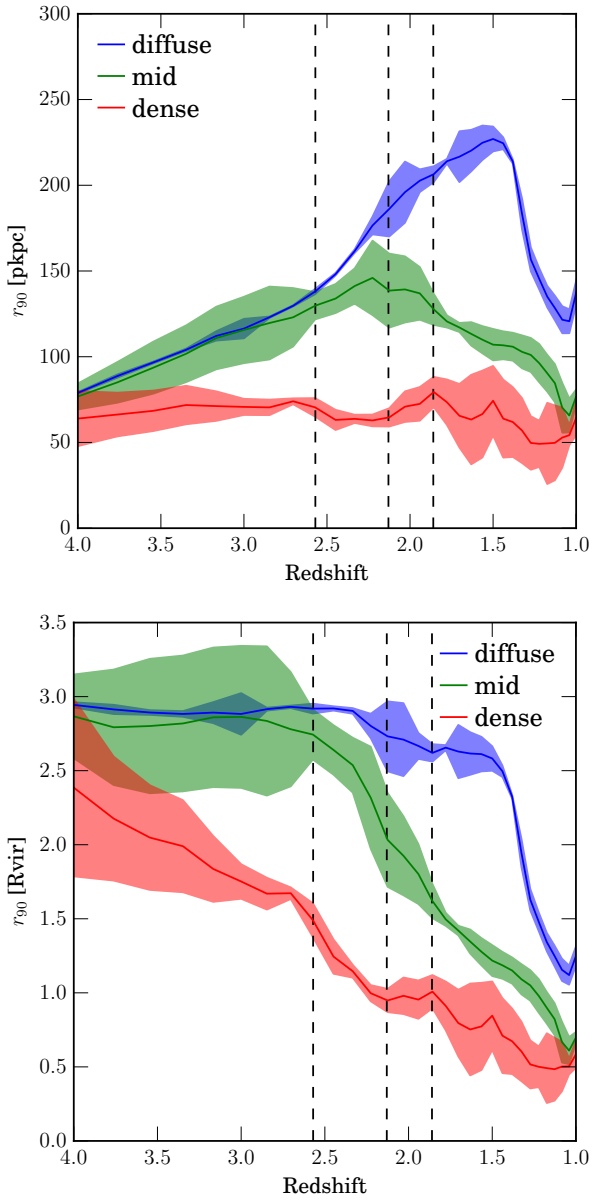

Fig. 5.4.— The physical size of the filament as a function of density cut used and time in (a) pkpc and (b) virial radius.

its length as measured by r_{90} is shown by the shaded are in Figure 5.4.

It was immediately apparent that diffuse gas extended farther out than high density gas across all time, confirming that the general trend shown in Figure 5.4

held throughout the entire length of the filament. The dense gas did not show any significant trend along the length of the filament. The only changes in r_{90} for the dense gas was a small evolution. This evolution occurred simultaneously along all parts of the filament, suggesting it is a passive evolution as there are not any astrophysical events that could force a uniform change across the entire length of the filament.

Diffuse gas showed similar behavior. There were only slight changes along the length of the filament and the changes were dominated by a temporal evolution.

The mid density gas did show significant trends along the filament. Initially, the mid density gas structure was thicker when close to the galaxy. The disparity in thickness as a function of proximity to the galaxy disappeared as the structure evolved. By $z \approx 2$ the mid-density filament achieved a uniform size along its length, a trait it kept until z=1 when the simulation ended.

On average the filament contained $10^{9.5}\,\mathrm{M}_{\odot}$ of gas. The amount of gas fluctuated over time but never by more than a factor of 2.5. Since the length of the filament was restricted to the length of the box and thus tied to R_{vir}, as time progress the filament included more material. Between the start and end of the simulation, R_{vir} increased by a factor of 4.5, leading to a naive estimation of a $\sim$4.5 increase in mass in the filament assuming no density evolution. The actual variation of 2.5 implied the density of the filament must have decreased over time, as seen in Figure 5.3.

The phase shift of the filament was also reflected in the mass distribution between the different phase selections, shown in Figure 5.5, Early in the history of the filament the majority of the mass was contained in the dense gas. By $z \approx 2.5$

the majority of the mass resided in the mid density gas. The diffuse gas was an insignificant portion of the filament by mass until $z \approx 1.25$.

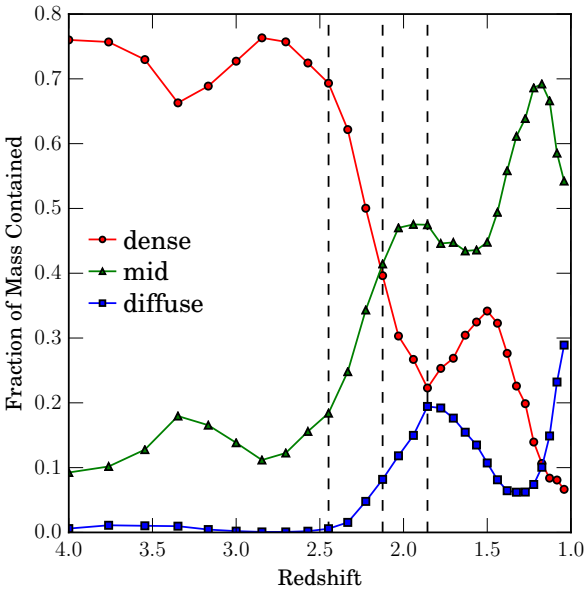

Fig. 5.5.— The total mass of gas contained within the filament across all density cuts. While the mass of the filament fluctuates with time with response to various environmental effects, the overall change is small (less than a factor of two)

5.4.2. Kinematics

In §5.4.1 the spatial distribution of the gas was shown to not be strongly dependent on the density cut used. This was not the case for the kinematics of the gas which depended more on the temperature selection used. Similarly to the density selections used in the previous sections, the temperature range was divided into three sections. Gas with temperatures between $10^{3.5}$ K and $10^{4.5}$ K was labeled as "cool", "warm" gas resided between $10^{4.5}$ K and $10^{5.5}$ K, and "hot" gas resided between $10^{5.5}$ K and $10^{6.5}$ K.

Combined with the density regimes used previously, the temperature regimes form nine phase cuts. Table 5.3 shows the fraction of gas cells in each phase cut averaged over all snapshots that are infalling as defined as having a negative radial velocity with respect to the galaxy's center of mass ($v_r < 0$). The standard deviation of the fraction over all snapshots is included. The cool gas forms the filament, so it is not surprising that this phase is mostly infalling, with 66% of all cool gas cells having $v_r < 0$. The fraction of infalling cool gas cells did not change appreciably across the density cuts, ranging from 61% for dense gas to 72% for diffuse gas. A smaller fraction of hotter gas cells were infalling, with only 49% and 21% of warm and hot gas cells respectively having a negative radial velocity.

To effectively measure the degree to which the radial component of the overall velocity velocity dominates the kinematics of the various phases of the filament the mean values of $v_r/|v|$ along with the standard deviation for each phase cut across all snapshots are shown in Table 5.4. Negative values correspond to infalling material while positive values correspond to outflowing material. As before, the temperature selection had a larger effect on the magnitude of the radial velocity component than the density selection.

The cool gas was the phase whose kinematics were most aligned towards the galaxy with 18% of its velocity vector aligned radially inward on average. The was no significant difference between the three density cuts. The relatively low value of 18% combined with the large standard deviation of values for each density cut suggests the cool gas is only mildly radially aligned and still had significant transverse velocity.

The warm gas was neither inflowing now outflowing on average, suggesting

this phase is predominately ambient gas. The diffuse warm gas had the most radially aligned kinematics, with ∼14% of the velocity vector aligned away from the galaxy on average. Similar to the cool gas, the larger values standard deviation of the fraction of the velocity vector aligned in the radial direction relative to the mean values makes any strong conclusions difficult.

The hot gas was the most phase whose kinematics were the most dominated by radial motions. The hot diffuse gas had 68% of its velocity vector aligned away from the galaxy, suggesting this phase is sensitive to outflows generated by stellar feedback. The denser hot gas was less strongly aligned with the radial vector than the diffuse phase, but was still the more radially aligned than the warm or cool gas.

In summary, infalling material was most likely to occur in cool gas phase while outflowing material was most likely to occur in hot gas phase. Warm gas was predominately neither infalling nor outflowing.

The kinematic trends were found for all gas in the phase cuts. Additionally insight was gained when considering the distance from the galaxy as well as the phase cut.

The evolution of the radial velocity of the cool gas The cold gas was generally

Table 5.3. Fraction of cells in each phase that are infalling

	Diffuse	Mid	Dense	Mean
Cool	0.72 ± 0.19	0.65 ± 0.15	0.61 ± 0.15	0.66 ± 0.28
Warm	0.45 ± 0.10	0.53 ± 0.11	0.50 ± 0.12	0.49 ± 0.19
Hot	0.21 ± 0.07	0.28 ± 0.08	0.38 ± 0.07	0.29 ± 0.13
Mean	0.46 ± 0.22	0.49 ± 0.21	0.49 ± 0.20	

inflowing at all distances along the filament. As the gas moves closer to the galaxy it speeds up. At large distances the infall velocity is low, less than 10 km/s. At smaller distances, the inflow rate increases, reaching a peak of 100 km/s at ∼1 R_{vir}. Within the CGM the cool gas is predominately outflowing.

The warm gas is neither inflowing nor outflowing, with $v_r \sim 0$. The mean v_r is constrained to be within ±100 km/s. In contrast with the cool gas, there is no trend with distance from the galaxy. Warm gas is neither inflowing nor outflowing regardless of its location.

The hot gas is almost exclusively outflowing. The radial velocity profile is more chaotic than the profile for cool or warm gas, with no consistent trend across time. The randomness of the profile is partially a result of the low number of hot gas cells at large distances, as hot gas is predominately located within 2 $R_{vir}$of the galaxy.

5.5. Non-Passive Evolution

While the galaxy has a relatively quiet history, it did experience a major merger at $z = 2.1$, with a mass ratio (M_{sat}/M_{host}) of 0.58. The merging satellited passed directly along the filament, providing a test of the stability of the structure

Table 5.4. Mean values of $v_r/|\vec{v}|$ for cells in each phase cut

	Diffuse	Mid	Dense	Mean
Cool	-0.17 ± 0.18	-0.18 ± 0.17	-0.19 ± 0.26	-0.18 ± 0.36
Warm	0.14 ± 0.24	-0.02 ± 0.24	0.07 ± 0.22	0.07 ± 0.40
Hot	0.68 ± 0.17	0.51 ± 0.16	0.32 ± 0.15	0.50 ± 0.28
Mean	0.22 ± 0.35	0.10 ± 0.33	0.07 ± 0.37	

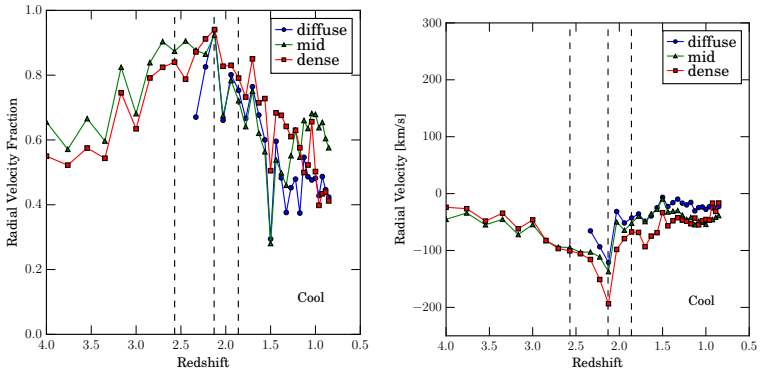

Fig. 5.6.— The evolution of the fraction of the gas cell's velocity in the radial direction (*left*) and the mean radial velocity (*right*) for cool filament gas. The dotted vertical lines denote the epochs defined in Table 5.2. The cool gas was predominately infalling with the majority of cool gas cells moving towards the galaxy with speeds of ∼50 km/s. The merger increased both the fraction of cool gas cells infalling and the rate at which they approached the galaxy. After the merger the cool gas cells return to their original kinematics. There was not a strong density dependence on the radial kinematics.

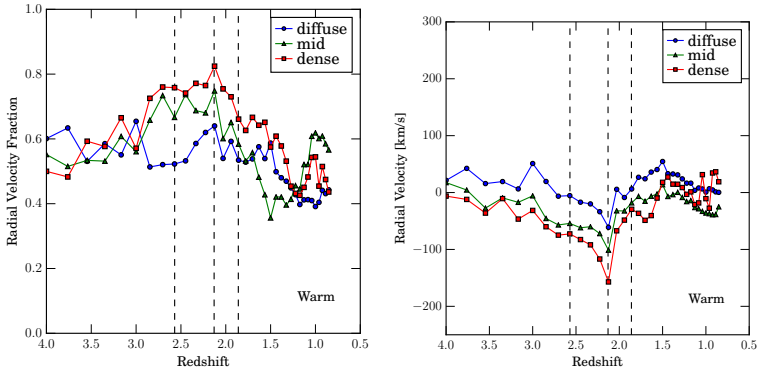

Fig. 5.7.— The evolution of the fraction of the gas cell's velocity in the radial direction (*left*) and the mean radial velocity (*right*) for warm filament gas. The dotted vertical lines denote the epochs defined in Table 5.2. Warm filament gas tended to be neither infalling now outflowing, with the mean radial velocity ∼0 km/s. The response of the warm gas to the merger and starburst mimicked that of the cool gas shown in Figure 5.6. The warm gas was more sensitive to density selection than the cool gas but all densities followed the same trends with redshift.

and kinematics of the filament when perturbed by a large satellite. The satellite is within the filament from $z = 2.4$ to $z = 2.1$, taking approximately 420 Myr to merge. The merging events provoked a period of increased star formation in the

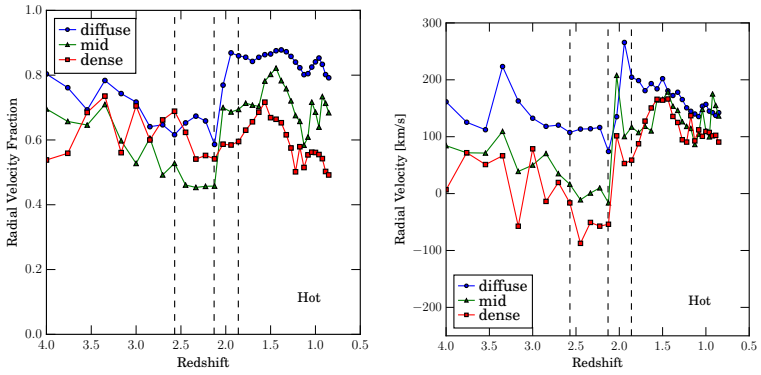

Fig. 5.8.— The evolution of the fraction of the gas cell's velocity in the radial direction (*left*) and the mean radial velocity (*right*) for hot filament gas. The dotted vertical lines denote the epochs defined in Table 5.2. The hot gas was primarily outflowing with significant density dependence. The diffuse hot gas had radial velocities ∼4x that of the dense hot gas. The merger did not significantly alter the kinematics of the hot gas while the starburst increased the radial velocity of all densities of the hot gas.

galaxy that generated strong outflows. In this section, the reaction of the filament to both the merger and outflows were studied.

5.5.1. Spatial

The physical size of the filament as measured by r_{90} did not exhibit any significant deviation from the passive evolution established in the formation epoch due to the merger, as seen in Figure 5.4. The cool dense core of the filament did not change size at any point in the simulation.

The size of the cool mid-density material did deviate from the passive evolution near the end of the merger epoch. The constant growth experienced from z=4 reached a maximum at the end of the merger epoch and the cool mid-density started to constrict.

The cool diffuse filament did react slightly to the merger. The grew similarly

to the mid-density gas until the merger starts. When the mid-density gas started to contract, the rare gas continued to expand growing until $z \sim 1.5$, when it started to rapidly contract, long after the starburst ends.

5.5.2. Kinematics

While the spatial distribution of filamentary gas, especially the dense core, was affected by the merger, the kinematics of the gas were significantly altered by the merger. The velocity vector of the cool, warm, and hot gas phases become more inwardly aligned during the merger event. Additionally, the cool gas reached higher speeds during the merger, reaching 250 km/s at the end of the merger epoch. The warm gas phase was typically stagnant with $v_r/\left|v\right| \sim 0$ km/s became more infalling during the merger epoch. The hot gad remained predominately outflowing with little change during the merger epoch.

During the starburst epoch all phase cuts became less infalling. The cool gas returned to its more positive mean radial velocity across all density cuts once the merger epoch ended, with little evolution afterwards. The warm gas likewise return to its previous stagnant state after the end of the merger. The hot phase, however, reached its fastest outflowing velocities during the starburst epoch.

The radial kinematics of the cool gas were not significantly different during the starburst epoch than in the formation epoch. The largest difference occurred immediately after the starburst. The outflowing cool gas was normally restricted to within 0.5 $R_{vir}$was instead pushed out to 0.75 R_{vir}during the starburst. During the starburst epoch, the CGM expanded and interacted with the filament, mixing the cool gas.

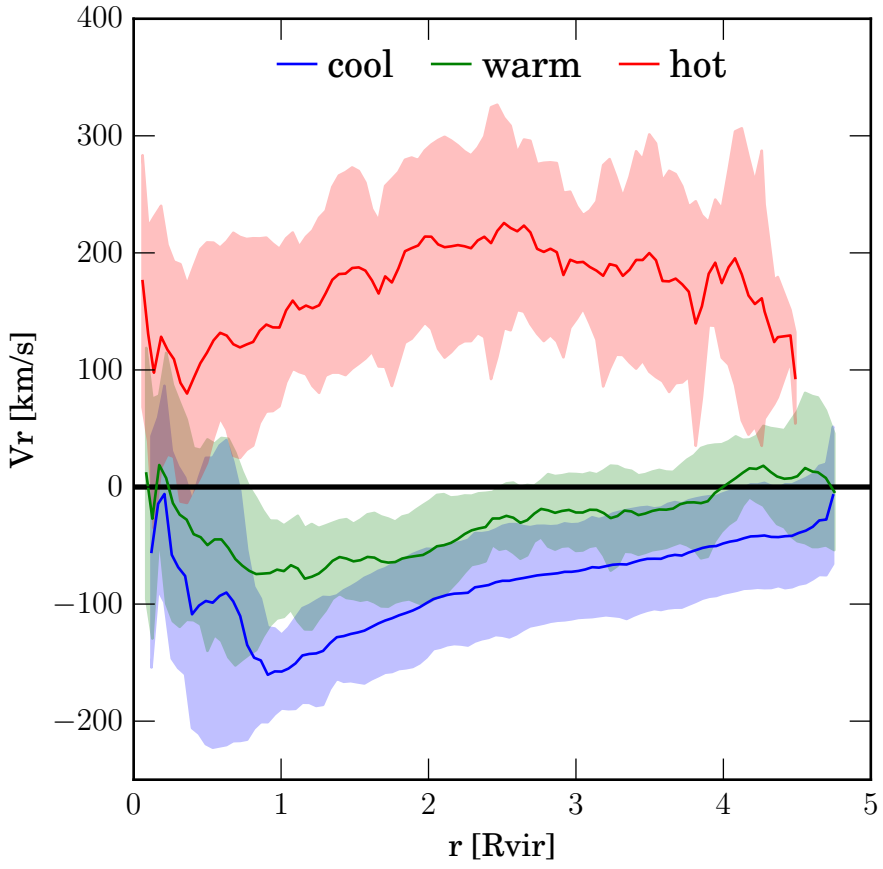

Fig. 5.9.— The reaction of the radial velocity of the filament's gas to the starburst. The solid lines are the mean value during the starburst. The shaded regions show the standard deviation of the means during the starburst. Hot gas is affected more by the burst than the cool or warm gas.

The reaction of the warm gas to the merger and starburst events did not depend on the density selection used. The dense, mid-density, and diffuse gas all followed the same pattern. During the merger the mean radial velocity of the warm gas became more negative indicating the bulk motion of the warm gas was towards the galaxy. Immediately after the end of the merger epoch the mean radial velocity of the warm gas returned to its state at the beginning of the merger event and did not evolve significantly afterwards. Any density selection applied

did not affect the described trends, merely the magnitudes of the mean radial velocities. In all snapshots the mean radial velocity of the diffuse warm gas was ∼25-50 km/s more positive than the mid-density gas. The dense warm gas had the most mean negative radial velocities for all snapshots with $z > 1.5$, typically ∼20 km/s more negative than the mid-density gas. After z=1.5 the mean radial velocity of the dense warm gas become comparable to mean radial velocities of the other warm gas phases at ∼0 km/s.

The hot gas kinematics were the most affected by the filament, perhaps not surprisingly, as outflows are expected to be hot (van de Voort & Schaye 2012), The infalling portion of the hot gas from the merger was quickly pushed out by the outflows.

The mean radial velocity of the dense hot gas changed from ∼-75 km/s at the end of the merger epoch to ∼100 km/s in the next snapshot. The dense hot gas remained predominately outflowing with speeds of 100-150 km/s for the rest of the simulation. Similar to the dense hot gas, the mean radial speed of the mid-density hot gas changed from ∼0 km/s at the end of the starburst epoch to a maximum of ∼200 km/s in the next snapshot. After this peak in radially outward motion motion the mean radial speed of the mid-density hot gas followed the same trends as the dense hot gas. The diffuse hot gas followed the same trends with time as the other hot gas phases, except it reached a higher maximum radial speed of ∼250 km/s away from the galaxy.

5.5.3. Metallicity

An expected byproduct of a starburst and its associated outflows is an increase in the number of metals in CGM. For each phase cut, the evolution of the mass-weighted mean metallicity in the filament is shown in Figure 5.10. In all phase cuts, metallicity increases with time.

The density cut applied to the cool gas had a significant affect on the metallicity evolution for the filament, while the warm and hot gas demonstrated the same metallicity evolution regardless of the density cut used in the formation epoch. Neither the warm nor the hot gas showed notable metallicity evolution until the merger epoch. At the beginning of the merger epoch the dense warm gas started to increase in mean metallicity while the mean metallicity of the diffuse and mid-density warm gas dropped slightly. During the starburst epoch the mid-density and dense warm gas reversed the decline and started to increase in mean metallicity. The hot gas similarly showed no metallicity evolution until the end of the merger epoch, at which point the metallicity of all density cutes rose until z=1. For all temperature cuts, the diffuse gas had lower mean metallicity than the mid-density gas, and the dense gas had the highest mean metallicity.

The effect of the starburst on each phase cut is a consequence of the typical phase of winds generated by stellar feedback which carry metal-enriched gas into the CGM from the ISM. The winds are hot, low-density gas centered at $\log(T) \sim 6$, $\log(n_H) \sim -5$. It follows that the diffuse gas should experience a larger increase in mean metallicity after the starburst than the mid-density or the dense gas, and the hot gas should likewise be affected more than the cool or warm gas. The trends discussed above and shown in Figure 5.10 agree with the predictions.

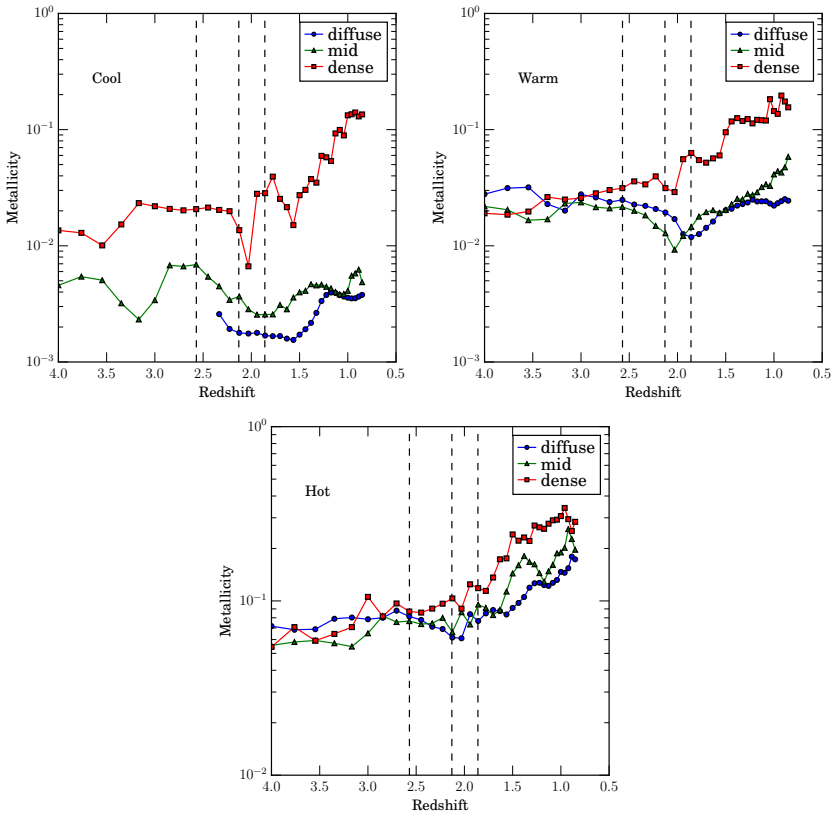

Fig. 5.10.— Evolution of the mass-weighted mean metallicity in each phase cut. The vertical dashed lines are the boundaries of the different epochs.

The addition of hot gas into the CGM had consequences for the preferred temperature of the ambient gas. The winds shift the dominant phase by mass they pass through. Gas that would be part of the warm/cool phase are pushed into the hot phase. Since the winds originate in the galaxy, warm/cool gas close to the galaxy was preferentially heated. Additionally, metallicity decreases with increased distance from the galaxy. By removing the relatively metal-rich warm/-cool gas close to the galaxy, the mean metallicity decreases until the winds pass by. The winds were estimated to travel at roughly 200 km/s.

5.6. Discussion

In this work the structure and kinematics of a gaseous filament feeding a galaxy from z=4 to z=1 was studied, by dividing the phase space of gas around the galaxy into cool, warm, and hot gas as well as diffuse, mid-density, and diffuse gas as detailed in §5.3. The evolution of each phase selection was studied in four epochs detailed in Table 5.2 which included a major merger and the subsequent starburst. The merging satellite had approximately half the mass of the host galaxy and had a large effect on the host. The influx of new material increased the SFR of the host by an order of magnitude for 575 Myr.

The filament was selected solely by phase criteria, the gas's density and temperature. The simple phase selection identified significantly metal-poor gas, characteristic of a filament bringing in pristine material along the cosmic web. This gas is indeed infalling into the galaxy at a consistent 100–200 km/s, depending on the distance along the filament.

A reoccurring trend in the filament properties was a general indifference to the galaxy. The galaxy experienced a major merger and a significant burst of star formation and the cool gas of the filament was not significantly affected. The size of the dense cool gas structure, which formed the filament core, as defined by r_{90} and shown in Figure 5.4 did not evolved through the entire run of the simulation. The core remained at a consistent 100 pkpc diameter with little variation.

The kinematics of the core did respond to the major events in the galaxy. The major merger increased the inflowing velocity of the cool gas. After the merger epoch the radial velocity of the cool gas returned to formation epoch rates. The return to prior infall rates is likely due to galactic winds generated by the star-

burst pushing back on infalling material. The increase in infall velocity was slow, starting just before the merger epoch. The slow-down at the beginning of the starburst epoch, however, was very quick, with the mean radial velocity of the dense cool core changing from 200 km/s to 100 km/s between two snapshots. Similar changes in the inflow velocity were seen in the warm and hot gas phases. The galactic winds themselves were found in the diffuse hot phase, but they affected the kinematics of all phases. The impact of the winds on the radial kinematics were most strongly seen in the warm and hot phases which were not part of the filament.

The galactic winds delivered metals produced in the starburst into the CGM and IGM. The core of the filament did see an increase in metallicity after the starburst.

The trends discussed above have implications for observations of the role of filaments galaxy evolution. Any observation that could only establish the physical size of the filament would not be able to determine anything about the history of the galaxy as the filament's size does not respond to events in the galaxy's history. However, if metallicity could be measured, then it would be possible study the galaxy's history. The metallicity of the filament did not evolve prior to the starburst, so observations of elevated metallicity in the core of a filament would suggest starburst event occurred in the galaxy's past.

The constant size of the filament's core has consequences for its role in governing galaxy evolution. Initially the core was over twice the diameter of the galaxy's virial radius. The galaxy was a small structure inside the filament and its baryon cycle would be dominated by accretion from the filament. As the galaxy gained

mass, its virial radius grew and eventually the galaxy outgrew the filament. By z=2.25 the virial radius was equal in size to the filament's core. The galaxy's halo had become the largest gaseous structure in the local volume of the simulation box. With the edge of the galaxy's halo, taken as the virial radius, breaching the filament's core the impact of the filament on galaxy's evolution must decline. The transition between filament dominated evolution and non-filament dominated evolution did not occur because the filament evolved but due to the galaxy's halo evolving.

5.7. Conclusions

In this chapter the evolution of a filament as it feeds a galaxy during a major merger and subsequent starburst was studied by selecting the gas purely by phase. The filament was identified as gas with temperature between $T = 10^{3.5}$ – $10^{4.5}$ K and hydrogen density to $n_H = 10^{-2.5}$ – $10^{-6.5}$ cm^{-3}. The filaments structure and kinematics were examined with attention to how the properties changed through the major events of the galaxy. Our main conclusions are listed below:

1. Phase selection was an effective method for identifying the gas composing the filament. The filament is structured with the densest gas in the center, and progressively less dense gas in the outer regions.

2. The filament's core was constant in size both in time and along the length of the filament at $\sim$ 50 pkpc, while the diffuse outer regions grow with time.

3. The structure of the filament core was unaffected by a large satellite passing through it along the path to the host galaxy. The kinematics of the core

were affected as the radial velocity of the cool gas increased as the satellite approached the host.

4. The subsequent starburst after the merger created large outflows that could be seen in the hot diffuse gas ($T = 10^{5.5}$ - $10^{6.5}$ K, $n_H = 10^{-5.5}$ - $10^{-6.5}$ cm^{-3}). The core of the filament endured the encounter with the outbursts. The increased radial velocity of the core caused by the merger was reduced to pre-merger levels by the winds.

5. As the galaxy grew the filament became less important both in size and mass. The virial radius of the galaxy began to outstrip the constant size of the filament core and the mass contained in the outflows began to exceed the mass contained within the filament itself. The ability of the filament to influence the galaxy's evolution began to subside.

This work is a simple case study of one filament in a single simulation. Caution should be taken in applying the conclusions here to all filaments. Simulations of galaxies with other environments, merging histories, or star formation histories should be studied to test if the conclusions of this work are globally accurate.

6. CONCLUSIONS

The focus of this dissertation was to explore the interplay between galaxy evolution and the baryon cycle by studying the circumgalactic medium of simulated galaxies with synthetic quasar absorption line observations. The method of mock observations enables a direct comparison between the simulations and observations. To create the mock observations the code `MOCKSPEC` was developed and applied to galaxies simulated with *hydroART*. The code generates synthetic absorption spectra for any transitions observed such as C IV $\lambda\lambda 1548, 1550$ taking into account instrumental effects such as pixelization and convolution with the ISF. `MOCKSPEC` then analyzes the spectra to calculate the equivalent width and AOD column density, and identifies which gas cells are responsible for the detected absorption.

`MOCKSPEC` was applied to cosmological hydrodynamic simulations of dwarf galaxies to determine the effect of various stellar feedback processes have on the CGM as traced by QAL measurements and to determine the ability of simulations to create an accurate CGM around dwarf galaxies. The conclusions were as follows:

- All feedback prescriptions were able to create an extended, multiphase, metal-rich CGM.
- Changing the details of the feedback prescription had no significant effect on the observed CGM as traced by H I and Mg II. The C IV absorbing CGM has slight variations.
- The CGM is not sensitive to the inclusion of radiation pressure but the O VI

absorbing CGM is sensitive to the strength of photoheating. The strength of the detected OVI absorption is below the detection limits of available instruments today.

- Observations of the CGM of dwarf galaxies are not a useful metric to differentiate between feedback mechanisms.

- While there are no observational data sets that perfectly match the galaxies simulated, the COS-Dwarfs sample is the closest. The simulated galaxies were unable to produces a strong enough CIV absorbing halo to agree with the COS-Dwarfs results. The discrepancy could be a consequence of the disparity with mass of the galaxies in each sample. The simulated spatial distribution of CIV absorbers does agree with the observations.

The dwarf galaxies were also used to study the veracity of the assumptions implicit in Voigt profile decomposition, specifically the assumption that the material responsible for the absorption is a spatially and kinematically coherent with a single density, temperature, and metallicity. The gas properties of the cells identified as being the source of the detected absorption by `MOCKSPEC` were compared to the gas properties derived from Voigt Profile (VP) fitting to arrive at the following conclusions:

- Absorption from low-ionization species such as HI and MgII arose from small, coherent structures with roughly uniform density, temperature, and metallicity. The assumptions implicit in VP decomposition are valid for low-ionization species.

- Absorption from high-ionization species such as C IV and O VI arose in large, volume-filling structures with large variations in density, temperature, and metallicity. The single structure appearance of the absorption profile was due to chance line-of-sight velocity alignments in the C IV and O VI absorbing medium. The assumptions implicit in VP decomposition are not valid for high-ionization species.

The `MOCKSPEC` code was applied to the `VELA` suite of simulations, a collection of Milky Way mass galaxies, to determine how the CGM varies across a range of stellar mass, environments, and time. As there are currently few observations of the CGM at high redshift that identify the host galaxy responsible for the detected absorption, the conclusions presented here serve as predictions for upcoming surveys. The conclusions are as follows:

- The strength of absorption features as a function of projected distance from the galaxy does not significantly evolve with time.

- Absorption from H I could be detected to large impact parameters, beyond the boundaries of the CGM. Mg II was restricted to LOS with $D < 30$ kpc. C IV could be found out to 60 kpc and O VI out to 80 kpc with observational limits. Weak C IV and O VI absorption features below most survey detection limits could be found at all impact parameters.

- The most temporal feature of the CGM was the dominant ionization mechanism for O VI. The fraction of O VI that is collisionally ionized was correlated with the galaxy's sSFR.

- The dominant ionization mechanism for gas cells responsible for O VI absorbing was collisional ionization, responsible for 90% of detected O VI absorption at z=4. The dominance of collisional ionization drops with time as the sSFR of the galaxy drops, reaching a low of 65% at z=1.

- The EW profile with impact parameter of H I and C IV in the `VELA` simulations did not match observations at $< z >$=2.2. A projection of the H I, Mg II, and O VI covering fraction to z=0.2 assuming no evolution did not match the results of the COS-Halos survey. The projection of the EW of Mg II profile to low-z did agree with the results of MAGIICAT.

The last section of this dissertation was the characterization of an inflow in one of the `VELA` simulations. The gas filament was selected by its density and temperature and characterized as the galaxy it fed experienced a major merger and a subsequent starburst. The conclusions of this study were as follows:

- The filament, as defined by the gas contained within it, is still settling by $z = 4$.

- The filament is structured with the densest gas in the center, and progressively less dense gas in the outer regions.

- The filament's core is constant in size both in time and along the length of the filament at $\sim$ 50 pkpc, while the diffuse outer regions grow with time.

- The filament's core is unaffected by a large satellite passing through it along the path to the host galaxy. The only effect is in the kinematics by increasing the radial velocity of the gas moving in.

- The subsequent starburst after the merger creates large outflows that can be seen in the hot diffuse gas ($T = 10^{5.5}$ – $10^{6.5}$ K, $n_H = 10^{-5.5}$ – $10^{-6.5}$ cm^{-3}). The core of the filament endures the encounter with the outbursts.

- As the galaxy grows the filament becomes less important both in size and mass. The virial radius of the galaxy begins to outstrip the constant size of the filament core and the mass contained in the outflows begins to exceed the mass contained within the filament itself. The ability of the filament to influence the galaxy's evolution begins to subside.

The work presented in this dissertation explored the interaction with the baryon cycle and galaxies in cosmological hydrodynamic simulations. The details of the model used to describe the main driver of the baryon cycle, stellar feedback, had a large effect on the properties of the galaxy by regulating star formation. The CGM as measured using mock QAL observations is insensitive to the details of the stellar feedback model.

The simple models used in most QAL analysis are unable to accurate determine the nature of the absorbing materials.

APPENDICES

REFERENCES

Abazajian, K., et al. 2003, AJ, 126, 2081

Agertz, O., Kravtsov, A. V., Leitner, S. N., & Gnedin, N. Y. 2013, ApJ, 770, 25

Agertz, O., et al. 2007, MNRAS, 380, 963

Aguirre, A., Hernquist, L., Schaye, J., Katz, N., Weinberg, D. H., & Gardner, J. 2001, ApJ, 561, 521

Arraki, K. S. 2016, PhD thesis, New Mexico State University

Baldry, I. K., Balogh, M. L., Bower, R. G., Glazebrook, K., Nichol, R. C., Bamford, S. P., & Budavari, T. 2006, MNRAS, 373, 469

Baldry, I. K., Glazebrook, K., Brinkmann, J., Ivezić, Ž., Lupton, R. H., Nichol, R. C., & Szalay, A. S. 2004, ApJ, 600, 681

Barro, G., et al. 2013, ApJ, 765, 104

—. 2014, ApJ, 791, 52

Behroozi, P. S., Wechsler, R. H., & Conroy, C. 2013a, ApJ, 770, 57

Behroozi, P. S., Wechsler, R. H., & Wu, H.-Y. 2013b, ApJ, 762, 109

Bell, E. F., McIntosh, D. H., Katz, N., & Weinberg, M. D. 2003, ApJ, 585, L117

Berger, M. J., & Colella, P. 1989, Journal of Computational Physics, 82, 64

Bergeron, J., et al. 1994, ApJ, 436, 33

Bertone, S., De Lucia, G., & Thomas, P. A. 2007, MNRAS, 379, 1143

Bertschinger, E., & Jain, B. 1994, ApJ, 431, 486

Bird, S., Vogelsberger, M., Sijacki, D., Zaldarriaga, M., Springel, V., & Hernquist, L. 2013, MNRAS, 429, 3341

Birnboim, Y., & Dekel, A. 2003, MNRAS, 345, 349

Boksenberg, A., Carswell, R. F., & Sargent, W. L. W. 1979, ApJ, 227, 370

Bond, J. R., Kofman, L., & Pogosyan, D. 1996, Nature, 380, 603

Bordoloi, R., et al. 2014, ApJ, 796, 136

Bregman, J. N. 1980, ApJ, 236, 577

Brook, C. B., et al. 2012, MNRAS, 426, 690

Brooks, A. M., Governato, F., Quinn, T., Brook, C. B., & Wadsley, J. 2009, ApJ, 694, 396

Bryan, G. L., et al. 2014, ApJS, 211, 19

Cen, R., & Chisari, N. E. 2011, ApJ, 731, 11

Ceverino, D., Arribas, S., Colina, L., Rodríguez Del Pino, B., Dekel, A., & Primack, J. 2016, MNRAS, 460, 2731

Ceverino, D., Dekel, A., & Bournaud, F. 2010, MNRAS, 404, 2151

Ceverino, D., & Klypin, A. 2009, ApJ, 695, 292

Ceverino, D., Klypin, A., Klimek, E. S., Trujillo-Gomez, S., Churchill, C. W., Primack, J., & Dekel, A. 2014, MNRAS, 442, 1545

Chen, H.-W. 2012, MNRAS, 427, 1238

Chen, H.-W., Gauthier, J.-R., Sharon, K., Johnson, S. D., Nair, P., & Liang, C. J. 2014, MNRAS, 438, 1435

Chieffi, A., & Limongi, M. 2013, ApJ, 764, 21

Churchill, C. W. 1997, PhD thesis, UNIVERSITY OF CALIFORNIA, SANTA CRUZ

Churchill, C. W., & Charlton, J. C. 1999, AJ, 118, 59

Churchill, C. W., Klimek, E., Medina, A., & Vander Vliet, J. R. 2014, ArXiv e-prints

Churchill, C. W., Mellon, R. R., Charlton, J. C., Jannuzi, B. T., Kirhakos, S., Steidel, C. C., & Schneider, D. P. 2000, ApJS, 130, 91

Churchill, C. W., Mellon, R. R., Charlton, J. C., & Vogt, S. S. 2003, ApJ, 593, 203

Churchill, C. W., Trujillo-Gomez, S., Nielsen, N. M., & Kacprzak, G. G. 2013, ApJ, 779, 87

Churchill, C. W., Vander Vliet, J. R., Trujillo-Gomez, S., Kacprzak, G. G., & Klypin, A. 2015, ApJ, 802, 10

Churchill, C. W., & Vogt, S. S. 2001, AJ, 122, 679

Crighton, N. H. M., Hennawi, J. F., & Prochaska, J. X. 2013, ApJ, 776, L18

Daddi, E., et al. 2010, ApJ, 713, 686

Davé, R., Hernquist, L., Weinberg, D. H., & Katz, N. 1997, ApJ, 477, 21

Davé, R., Oppenheimer, B. D., & Finlator, K. 2011, MNRAS, 415, 11

Davé, R., Oppenheimer, B. D., Katz, N., Kollmeier, J. A., & Weinberg, D. H. 2010, MNRAS, 408, 2051

Dehnen, W., & Read, J. I. 2011, European Physical Journal Plus, 126, 55

Dekel, A., & Birnboim, Y. 2006, MNRAS, 368, 2

Dekel, A., et al. 2009, Nature, 457, 451

Draine, B. T. 2011, Physics of the Interstellar and Intergalactic Medium

Eggen, O. J., Lynden-Bell, D., & Sandage, A. R. 1962, ApJ, 136, 748

Erb, D. K., Shapley, A. E., Pettini, M., Steidel, C. C., Reddy, N. A., & Adelberger, K. L. 2006, ApJ, 644, 813

Evans, J. L. 2011, PhD thesis, New Mexico State University

Evans, II, N. J., et al. 2009, ApJS, 181, 321

Faber, S. M., et al. 2007, ApJ, 665, 265

Faerman, Y., Sternberg, A., & McKee, C. F. 2017, ApJ, 835, 52

Faucher-Giguère, C.-A., & Kereš, D. 2011, MNRAS, 412, L118

Ferland, G. J., Korista, K. T., Verner, D. A., Ferguson, J. W., Kingdon, J. B., & Verner, E. M. 1998, PASP, 110, 761

Ferland, G. J., et al. 2013, Rev. Mexicana Astron. Astrofis., 49, 137

Ford, A. B., Davé, R., Oppenheimer, B. D., Katz, N., Kollmeier, J. A., Thompson, R., & Weinberg, D. H. 2014, MNRAS, 444, 1260

Ford, A. B., Oppenheimer, B. D., Davé, R., Katz, N., Kollmeier, J. A., & Weinberg, D. H. 2013, MNRAS, 432, 89

Ford, A. B., et al. 2016, MNRAS, 459, 1745

Frenk, C. S., & White, S. D. M. 2012, Annalen der Physik, 524, 507

Fumagalli, M., Prochaska, J. X., Kasen, D., Dekel, A., Ceverino, D., & Primack, J. R. 2011, MNRAS, 418, 1796

Genzel, R., et al. 2010, MNRAS, 407, 2091

Gingold, R. A., & Monaghan, J. J. 1977, MNRAS, 181, 375

Green, J. C., et al. 2012, ApJ, 744, 60

Gutcke, T. A., Stinson, G. S., Macciò, A. V., Wang, L., & Dutton, A. A. 2017, MNRAS, 464, 2796

Haardt, F., & Madau, P. 2001, in Clusters of Galaxies and the High Redshift Universe Observed in X-rays, ed. D. M. Neumann & J. T. V. Tran

Haardt, F., & Madau, P. 2011, ArXiv e-prints

—. 2012, ApJ, 746, 125

Harford, A. G., Hamilton, A. J. S., & Gnedin, N. Y. 2008, MNRAS, 389, 880

Heckman, T. M., Norman, C. A., Strickland, D. K., & Sembach, K. R. 2002, ApJ, 577, 691

Heitmann, K., Ricker, P. M., Warren, M. S., & Habib, S. 2005, ApJS, 160, 28

Hopkins, P. F. 2014, GIZMO: Multi-method magneto-hydrodynamics+gravity code, Astrophysics Source Code Library

Hopkins, P. F., Quataert, E., & Murray, N. 2011, MNRAS, 417, 950

Humlek, J. 1979, Journal of Quantitative Spectroscopy and Radiative Transfer, 21, 309

Hummels, C., Smith, B., & Silvia, D. 2016, ArXiv e-prints

Hummels, C. B., Bryan, G. L., Smith, B. D., & Turk, M. J. 2013, MNRAS, 430, 1548

Iwamoto, K., Brachwitz, F., Nomoto, K., Kishimoto, N., Umeda, H., Hix, W. R., & Thielemann, F.-K. 1999, ApJS, 125, 439

Jenkins, E. B. 1996, ApJ, 471, 292

Katz, N., Quinn, T., Bertschinger, E., & Gelb, J. M. 1994, MNRAS, 270, L71

Katz, N., Quinn, T., & Gelb, J. M. 1993, MNRAS, 265, 689

Katz, N., & White, S. D. M. 1993, ApJ, 412, 455

Kennicutt, Jr., R. C., Tamblyn, P., & Congdon, C. E. 1994, ApJ, 435, 22

Kereš, D., Katz, N., Fardal, M., Davé, R., & Weinberg, D. H. 2009, MNRAS, 395, 160

Kereš, D., Katz, N., Weinberg, D. H., & Davé, R. 2005, MNRAS, 363, 2

Klypin, A. A., Trujillo-Gomez, S., & Primack, J. 2011, ApJ, 740, 102

Komatsu, E., et al. 2009, ApJS, 180, 330

Kravtsov, A. V. 1999, PhD thesis, NEW MEXICO STATE UNIVERSITY

—. 2003, ApJ, 590, L1

Kravtsov, A. V., Klypin, A. A., & Khokhlov, A. M. 1997, ApJS, 111, 73

Krumholz, M. R., & Tan, J. C. 2007, ApJ, 654, 304

Lehner, N., et al. 2013, ApJ, 770, 138

L'Huillier, B., Combes, F., & Semelin, B. 2012, A&A, 544, A68

Liang, C. J., Kravtsov, A. V., & Agertz, O. 2016, MNRAS, 458, 1164

Madau, P., & Dickinson, M. 2014, ARA&A, 52, 415

Marasco, A., Debattista, V. P., Fraternali, F., van der Hulst, T., Wadsley, J., Quinn, T., & Roškar, R. 2015, MNRAS, 451, 4223

Martin, D. C., Chang, D., Matuszewski, M., Morrissey, P., Rahman, S., Moore, A., & Steidel, C. C. 2014, ApJ, 786, 106

Martin, D. C., et al. 2007, ApJS, 173, 342

Matejek, M. S., & Simcoe, R. A. 2012, ApJ, 761, 112

Mathes, N. L., Churchill, C. W., Kacprzak, G. G., Nielsen, N. M., Trujillo-Gomez, S., Charlton, J., & Muzahid, S. 2014, ApJ, 792, 128

McGaugh, S. S. 2008, in IAU Symposium, Vol. 244, Dark Galaxies and Lost Baryons, ed. J. I. Davies & M. J. Disney, 136–145

McGaugh, S. S., Schombert, J. M., de Blok, W. J. G., & Zagursky, M. J. 2010, ApJ, 708, L14

McKee, C. F., & Ostriker, E. C. 2007, ARA&A, 45, 565

Murray, N., Ménard, B., & Thompson, T. A. 2011, ApJ, 735, 66

Muzahid, S. 2014, ApJ, 784, 5

Neistein, E., van den Bosch, F. C., & Dekel, A. 2006, MNRAS, 372, 933

Nielsen, N. M., Churchill, C. W., & Kacprzak, G. G. 2013a, ApJ, 776, 115

Nielsen, N. M., Churchill, C. W., Kacprzak, G. G., & Murphy, M. T. 2013b, ApJ, 776, 114

Ocvirk, P., Pichon, C., & Teyssier, R. 2008, MNRAS, 390, 1326

Oppenheimer, B. D., & Davé, R. 2006, MNRAS, 373, 1265

—. 2008, MNRAS, 387, 577

—. 2009, MNRAS, 395, 1875

Oppenheimer, B. D., Davé, R., Kereš, D., Fardal, M., Katz, N., Kollmeier, J. A., & Weinberg, D. H. 2010, MNRAS, 406, 2325

Oppenheimer, B. D., & Schaye, J. 2013a, MNRAS, 434, 1063

—. 2013b, MNRAS, 434, 1043

Owen, J. M., Villumsen, J. V., Shapiro, P. R., & Martel, H. 1998, ApJS, 116, 155

Pallottini, A., Gallerani, S., & Ferrara, A. 2014, MNRAS, 444, L105

Peeples, M. S., Werk, J. K., Tumlinson, J., Oppenheimer, B. D., Prochaska, J. X., Katz, N., & Weinberg, D. H. 2014, ApJ, 786, 54

Peng, Y., Maiolino, R., & Cochrane, R. 2015, Nature, 521, 192

Persic, M., & Salucci, P. 1992, MNRAS, 258, 14P

Pettini, M., Madau, P., Bolte, M., Prochaska, J. X., Ellison, S. L., & Fan, X. 2003, ApJ, 594, 695

Pflamm-Altenburg, J., & Kroupa, P. 2009, ApJ, 706, 516

Pieri, M. M., & Haehnelt, M. G. 2004, MNRAS, 347, 985

Planck Collaboration et al. 2016, A&A, 594, A13

Powell, L. C., Slyz, A., & Devriendt, J. 2011, MNRAS, 414, 3671

Prochaska, J. X., O'Meara, J. M., & Worseck, G. 2010, ApJ, 718, 392

Rahman, N., et al. 2012, ApJ, 745, 183

Rahmati, A., Pawlik, A. H., Raicevic, M., & Schaye, J. 2013, MNRAS, 430, 2427

Rahmati, A., Schaye, J., Crain, R. A., Oppenheimer, B. D., Schaller, M., & Theuns, T. 2016, MNRAS, 459, 310

Rasmussen, J., Ponman, T. J., Verdes-Montenegro, L., Yun, M. S., & Borthakur, S. 2008, MNRAS, 388, 1245

Rudie, G. C., et al. 2012, ApJ, 750, 67

Sarkar, P., Pandey, B., & Bharadwaj, S. 2012, MNRAS, 423, 955

Savage, B. D., & Sembach, K. R. 1991, ApJ, 379, 245

Schawinski, K., et al. 2014, MNRAS, 440, 889

Schaye, J., Aguirre, A., Kim, T.-S., Theuns, T., Rauch, M., & Sargent, W. L. W. 2003, ApJ, 596, 768

Schneider, D. P., et al. 1993, ApJS, 87, 45

Searle, L., & Zinn, R. 1978, ApJ, 225, 357

Sembach, K. R., & Savage, B. D. 1992, ApJS, 83, 147

Sharma, M., Nath, B. B., Chattopadhyay, I., & Shchekinov, Y. 2014, MNRAS, 441, 431

Shen, J., Abel, T., Mo, H. J., & Sheth, R. K. 2006, ApJ, 645, 783

Shen, S., Madau, P., Aguirre, A., Guedes, J., Mayer, L., & Wadsley, J. 2012, ApJ, 760, 50

Shen, S., Madau, P., Guedes, J., Mayer, L., Prochaska, J. X., & Wadsley, J. 2013, ApJ, 765, 89

Simcoe, R. A., Sargent, W. L. W., & Rauch, M. 2004, ApJ, 606, 92

Simcoe, R. A., Sargent, W. L. W., Rauch, M., & Becker, G. 2006, ApJ, 637, 648

Smith, B. D., Hallman, E. J., Shull, J. M., & O'Shea, B. W. 2011, ApJ, 731, 6

Springel, V. 2005, MNRAS, 364, 1105

—. 2010, MNRAS, 401, 791

Springel, V., Frenk, C. S., & White, S. D. M. 2006, Nature, 440, 1137

Steidel, C. C., Erb, D. K., Shapley, A. E., Pettini, M., Reddy, N., Bogosavljević, M., Rudie, G. C., & Rakic, O. 2010, ApJ, 717, 289

Stewart, K. R., Kaufmann, T., Bullock, J. S., Barton, E. J., Maller, A. H., Diemand, J., & Wadsley, J. 2011, ApJ, 735, L1

Stinson, G. S., et al. 2012, MNRAS, 425, 1270

Strateva, I., et al. 2001, AJ, 122, 1861

Suresh, J., Rubin, K. H. R., Kannan, R., Werk, J. K., Hernquist, L., & Vogelsberger, M. 2017, MNRAS, 465, 2966

Sutherland, R. S., & Dopita, M. A. 1993, ApJS, 88, 253

The HDF Group. 1997-2017, Hierarchical Data Format, version 5, http://www.hdfgroup.org/HDF5/

Theuns, T., Leonard, A., Efstathiou, G., Pearce, F. R., & Thomas, P. A. 1998, MNRAS, 301, 478

Thom, C., et al. 2012, ApJ, 758, L41

Trujillo-Gomez, S., Klypin, A., Colín, P., Ceverino, D., Arraki, K. S., & Primack, J. 2015, MNRAS, 446, 1140

Trujillo-Gomez, S., Klypin, A., Primack, J., & Romanowsky, A. J. 2011, ApJ, 742, 16

Tumlinson, J., et al. 2011, Science, 334, 948

—. 2013, ApJ, 777, 59

Turk, M. J., Smith, B. D., Oishi, J. S., Skory, S., Skillman, S. W., Abel, T., & Norman, M. L. 2011, ApJS, 192, 9

van de Voort, F., Bahé, Y. M., Bower, R. G., Correa, C. A., Crain, R. A., Schaye, J., & Theuns, T. 2017, MNRAS, 466, 3460

van de Voort, F., & Schaye, J. 2012, MNRAS, 423, 2991

Werk, J. K., et al. 2014, ApJ, 792, 8

Wiersma, R. P. C., Schaye, J., & Smith, B. D. 2009, MNRAS, 393, 99

Wiersma, R. P. C., Schaye, J., & Theuns, T. 2011, MNRAS, 415, 353

Zolotov, A., et al. 2015, MNRAS, 450, 2327

Zuckerman, B., & Evans, II, N. J. 1974, ApJ, 192, L149